Transactional Array Reconciliation Tomography for Precision Indoor Location

by

Vincent T. Amendolare

A Dissertation
Submitted to the Faculty
of the
WORCESTER POLYTECHNIC INSTITUTE
in partial fulfillment of the requirements for the
Degree of Doctor of Philosophy
in
Electrical and Computer Engineering
by

_____

May 2010

APPROVED:

_____

Professor David Cyganski, Major Advisor

_____

Professor R. James Duckworth

_____

Professor Arthur C. Heinricher

Abstract

This dissertation was conducted as part of the efforts related to WPI's Precision Personnel Location (PPL) project, the purpose of which is to locate emergency personnel in hazardous indoor environments using radio location techniques. The current PPL system prototype uses a radio transmitter worn by the personnel, indoors, and receivers on reference units, outdoors. This dissertation proposes a new system architecture with bidirectional radio transmissions to replace the current unidirectional system architecture. This allows the development of a synchronization scheme that can extract additional Time of Arrival (TOA) information for estimating the location of personnel. This dissertation also describes an extension of the multi-signal fusion technique previously used that incorporates this TOA information. At the cost of a more complicated mobile unit design, resultant benefits of this approach include rejection of signal reflectors as solutions, improved accuracy with limited reference unit geometries, improved noise rejection and significant computation reduction. In this dissertation the mathematical underpinnings of this approach are presented, a performance analysis is developed and the results are evaluated in the context of experimental data.

Acknowledgements

To my family: I am eternally grateful of my family: Dad, Mum, and Nick for the support in my academic efforts and everything else I do; my wonderful fiancé Rhiannon for her love, support and patience.

To my sponsor: I would like to thank the Department of Homeland Security and Federal Emergency Management Agency for funding this research, both for giving me this research opportunity and also striving to protect the lives of personnel in hazardous situations.

To my fellow team members: I would never have achieved this goal without the wisdom and knowledge of my past lab mates, David Holl and Benjamin Woodacre. Also thanks to the students on this project (past and present) who have struggled with me through many days of system testing: Jack Coyne, Hauke Dämpfling, Hemish Parikh, Vivek Varshney, Matt Campbell, Jorge Alejandro, Vasil Savov, Andrew Cavanaugh, Matt Lowe and Jamie Mitchell. Also thanks to Bob Boisse for his hard work and keeping us organized.

To my committee: I also extend my appreciation to my thesis committee members, Professor Duckworth and Professor Heinricher, for taking the time out of their busy schedules to review this dissertation.

To my advisor: Lastly I would like to thank my advisor, Professor Cyganski. His immense knowledge, guidance, patience, and sense of humor have made the last several years working for him a great pleasure and very rewarding.

Contents

List of Figures

List of Tables

Chapter 1

Introduction

This dissertation was written in support of the Precision Personnel Location (PPL) project which is being conducted by the Electrical and Computer Engineering Department of Worcester Polytechnic Institute (WPI). This project has received funding from the Department of Justice, Department of Homeland Security, Federal Emergency Management Agency and Honeywell. The goal of the project is to design a precision location system capable of locating first responders in indoor environments. This dissertation deals specifically with improving the accuracy of this system with additional timing information obtained via two-way signal exchanges between mobile devices worn by the first responders and reference units at fixed positions outdoors.

Throughout this document several acronyms are used. Each are defined in the text, but are also provided in Table 1.1 as a quick reference. Similarly mathematical conventions are provided in Table 1.2 and variable names used in Table 1.3.

1.1 Precision Personnel Location Problem

On December 3, 1999 a veritable tragedy occurred in Worcester, Massachusetts. An aging brick warehouse, the former Worcester Cold Storage and Warehouse Co. building, became host to a fierce inferno. What at first seemed like a routine response by the Worcester Fire Department turned out to be deadly. Two firefighters entered the building initially, concerned that people might be inside. The two men soon found themselves in trouble and called for help using their radios. Four more firefighters were sent in to search for them, but soon became missing themselves. Several other

ADC	Analog to Digital Converter
DAC	Digital to Analog Converter
DFT	Discrete Fourier Transform
DSS	Direct State Space
FFT	Fast Fourier Transform
GAC	Geometric Autoconfiguration
GPS	Global Positioning System
PPL	Precision Personnel Location
RF	Radio Frequency
RMS	Root Mean Square
RX	Receiver
σART	Singular Value Array Reconciliation Tomography
SNR	Signal to Noise Ratio
TART	Transactional Value Array Reconciliation Tomography
TCVR	Transceiver
TDOA	Time Difference Of Arrival
TOA	Time Of Arrival
TX	Transmitter
WPI	Worcester Polytechnic Institute
1D	One-Dimensional
2D	Two-Dimensional
3D	Three-Dimensional

Table 1.1: Acronyms

Time and frequency	$x(t) \overset{\mathcal{F}}{\Leftrightarrow} X(\omega) = X(2\pi f)$
Imaginary unit	$j = \sqrt{-1}$
Set of all real numbers	$\mathbb{R}$
Set of all complex numbers	$\mathbb{C}$
Real part of complex number	$\mathrm{Re}(z)$
Imaginary part of complex number	$\mathrm{Im}(z)$
Element in set	$\in$
Natural logarithm	$\ln x$
Base of natural logarithm	e
Angle of complex number	$z = xe^{j\theta}$, $\angle z = \theta + 2\pi a$, for integer a
Unit impulse function [23]	$\delta(t) = \begin{cases} +\infty, & t = 0 \\ 0, & t \neq 0 \end{cases}$, $\int_{-\infty}^{\infty} \delta(t)dt = 1$
Convolution [23]	$z(t) = x(t) * y(t)$, $z(t) = \int_{-\infty}^{\infty} y(t)x(t-\tau)d\tau$
Vector	$\mathbf{x}$
Matrix	$\mathbf{X}$
Element in matrix	$(\mathbf{X})_{a,b}$
Absolute value or complex magnitude	$\lvert \cdot \rvert$
Euclidean norm	$\lVert \cdot \rVert$
Random variable	$\tilde{x}$
Test value	$\overset{\#}{x}$
Conjugate transpose (Hermitian)	$\mathbf{X}^H$
Entrywise, Hadamard or Schur product	$\mathbf{Z} = \mathbf{X} \circ \mathbf{Y}$, $(\mathbf{Z})_{a,b} = (\mathbf{X})_{a,b}(\mathbf{Y})_{a,b}$
Entrywise complex magnitude	$\mathbf{Z} = \mathrm{elm}(\mathbf{X})$,$(\mathbf{Z})_{a,b} = \lvert(\mathbf{X})_{a,b}\rvert$
Argument of the maximum	argmax
Expectation operator	$E\{\cdot\}$
Is distributed as	$\sim$
Determinant of matrix	$\det\mathbf{X}$
Variance of random variable	$\mathrm{var}\tilde{x}$
Covariance of random variable	$\mathrm{cov}\tilde{x}$
Standard deviation of random variable	$\mathrm{std}\tilde{x}$
Root Mean Square of random variable	$\mathrm{rms}\tilde{x}$
Normal distribution	$N(\mu, \sigma^2)$
Multivariate normal distribution	$N(\boldsymbol{\mu}, \boldsymbol{\Sigma})$
Multivariate complex normal distribution	$C(\boldsymbol{\mu}, \boldsymbol{\Gamma})$
Rice distribution	$R(\nu, \sigma^2)$
Del operator	∇

Table 1.2: Mathematical Conventions

Speed of light [meters/second]	c
Range [meters]	[meters]
Time [seconds]	t
Discrete time [samples]	k
Number of time samples	K
Frequency [Hz]	f
Angular frequency [radians/second]	ω
Signal period [seconds]	T
Frequency spacing between carriers	Δf, $\Delta\omega$
Signal index	n
Number of signals	N
Carrier index	m
Number of carriers	M
Reference unit index	p
Number of reference units	P
Mobile unit index	q
Number of mobile units	Q
Time delay for signal n	t_n
Time delay for signal n and Reference Antenna p	$t_{n,p}$
Attenuation for signal n	γ_n
Attenuation for signal n and Reference Antenna p	$\gamma_{n,p}$
Vector of carrier frequencies	$\mathbf{f}$ or $\boldsymbol{\omega}$
Centered vector of carrier frequencies	$\boldsymbol{\omega}_c$
Transmitted signal	$x(t)$,$X(\omega)$, $x(k)$, $\mathbf{x}$
Received signal	$r(t)$,$R(\omega)$,$\mathbf{r}$
Channel response	$h(t)$,$H(\omega)$,$\mathbf{h}$
Sample clock frequency	f_s
RF mixer frequency	f_c
Random time-offset	$\tilde{\tau}$
Random phase offset	$\tilde{\theta}$
Position vector	$\mathbf{v}$
Mobile unit position	$\mathbf{v}_l$
Mobile unit position test value	$\overset{\#}{\mathbf{v}}_l$
Mobile unit position estimate	$\overset{\star}{\mathbf{v}}_l$
Reference unit position	$\mathbf{v}_p$
Received signals matrix	$\mathbf{R}$
Rephased received signals matrix	$\mathbf{R}'$
Ideal synchronization rephased received signals matrix	$\mathbf{R}'_{ideal}$
Received signals matrix rephased to correct location	$\overset{\star}{\mathbf{R}}'$
Time delay test value for Reference Antenna p	$\overset{\#}{t}_{0,p}$
Rectified received signal	$\mathbf{s}$
Ideal TART metric function	$f(\mathbf{v})$

Table 1.3: Variable Names

firefighters searched for their comrades for some time, but to no avail. The fire was too fierce, and they were forced to evacuate. None of the six men made it out of the building alive. [11, 27]

This depressing event left many questions in people's minds. How could this happen? What could have been done to prevent such a tragedy? If only the firefighters had better knowledge of where to look for their fallen companions, they may have been able to all get out safely. Could this have been possible? Does the technology exist to keep track of individuals in such an environment? Sadly, it does not. It is for this reason that the Electrical and Computer Engineering Department of Worcester Polytechnic Institute assembled a team of researchers, currently funded by the United States government's Department of Homeland Security and Federal Emergency Management Agency, to create such a technology.

The goal that our team is trying to achieve is the creation of a location system for personnel such as firefighters that requires no preexisting infrastructure and can perform accurately in hazardous indoor environments. This project has been titled the Precision Personnel Location project. In our proposed system, an incident commander would be constantly updated with the knowledge of the location of his/her personnel. The system needs to be able to be put into operation quickly, without any preexisting knowledge of the site, since it is never known when or where a fire response (or similar event) is needed. [29]

The desired level of accuracy is such that our position estimates are within 1 foot of the true position. This is so that there is as little ambiguity as possible as to where the personnel are located, whether on one side of a wall or another for example. The system should also record position estimates over time so that the paths taken by personnel are available in case they are needed to direct personnel back the way they came or send someone after them. Other features of the system include a wireless data channel for sending information such as environmental and physiological conditions. [29]

1.2 RF-based Indoor Position Estimation

There are many avenues that may lead to a solution to the indoor location problem. The existing Global Positioning System (GPS) uses radio frequency electromagnetic waves to perform position estimation, but suffers from poor accuracy indoors in its standard operation.[22] Other methods

include inertial navigation and even ultrasound based systems.[21]

Our team decided to use radio frequency electromagnetic waves (RF) as our means for position estimation. In the proposed scheme, inside a building each person to be located would wear a transmitter device with an antenna to generate a signal. Outside the building this signal would be received by units with antennas on them.

Let c be the speed of light in our environment. If the time the signal took to propagate through the air from the transmit antenna to the receive antennas could be determined, then the distance between the antennas, called the range, can be deduced.

$$r = ct, \tag{1.1}$$

where r is the range in meters, c is the speed of light in meters per second, and t is the time of propagation in seconds from the transmit antenna to the receive antenna.

It is known that in air electromagnetic waves at radio frequencies travel at very close to the speed of light in a vacuum, 299,792,458 meters per second. In some cases however, it is useful to compute a more precise value of the speed of light in air based upon atmospheric conditions.[26]

If the range from the transmit antenna to several receive antennas outside the building can be measured, then the position of the transmitter may be determined geometrically. This assumes that the locations of the receive antennas are known. Thus some sort of procedure must be executed when the system is deployed to determine these receive antenna positions. This may performed manually by surveying with measuring devices, although in an emergency situation this would not be practical. Thus the locations of the receive antennas should be measured automatically by the system using a radio ranging approach similar to how the personnel-attached transmitter is located. This is known as Geometric Autoconfiguration (GAC), and has been an active research area for the PPL team.[32, 33] In the firefighter application the receive antennas would most likely be fixed to firetrucks extended upon ladders outside the building. The system concept is illustrated in Figures 1.1.

The greatest challenge with performing indoor location with radio frequency electromagnetic waves is the complexity of the radio propagation environments involved. Radio waves are reflected by metal objects, which are plentiful in indoor environments. This results in the signals received being a combination of the so called direct path signal, and reflected signals, called multipath. This

Figure 1.1: Precision Personnel Location System [30]

behavior is illustrated in Figure 1.2. The direct path is always the shortest path, since it travels

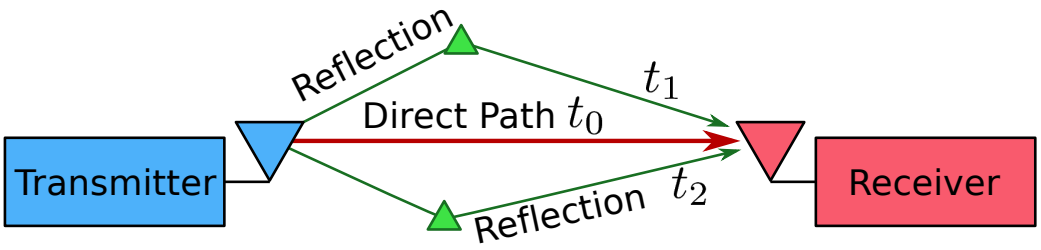

Figure 1.2: Multipath

directly from the transmit antenna to the receive antenna. But before one could hope to make such a distinction the direct path signal and multipath signals must be disentangled somehow. This problem contributes strongly to why current GPS systems do not function accurately indoors. A successful RF indoor location system development must find a way to take the multipath problem into account and mitigate its effects.

There are different possible RF signal structures that may be used to solve the indoor location problem. One notable approach is known an Impulse Ultra-Wideband (UWB) which uses a series of pulses that are very narrow in time, and thus very broad in frequency. This causes the signal to occupy frequencies in use by other services so such sources are regulated to use low power levels so as to not interfere with these other services. The low power levels make it difficult to perform location at larger distances or through building materials. [28]

The Impulse Ultra-Wideband approach attempts to perform one-dimensional ranging between the transmit antenna and each receive antenna. Then from these one-dimensional ranges a position estimate is deduced. In practice it is generally not possible to determine the absolute distance from a transmitter to a receiver. Instead the relative differences of the ranges is determined, adding an extra degree of freedom that is resolvable with an additional receive antenna position. This is known as the Time Difference Of Arrival (TDOA) approach, as opposed to absolute Time Of Arrival (TOA). From these range estimates (or relative range estimates) the position can be deduced using a solution method called multilateration. One algorithm that can achieve this is the Bard algorithm.[7]

Because of the issues inherent with the Impulse Ultra-Wideband approach, the early efforts in the WPI Precision Personnel Location project considered alternate location systems and associated ranging signals. The next chapter will introduce the method that was chosen, which uses a so

called multicarrier signal. In addition to using a unique ranging signal, the WPI PPL team developed a unique algorithm called Singular Value Array Reconciliation Tomography (σART). This algorithm estimates the position of a mobile transmitter based upon received multicarrier signals. Unlike existing RF location systems which estimate one-dimensional ranges before multilateration, σART performs a multi-signal fusion operation to solve for a position estimate directly.[12]

This dissertation contributes an extension to both the PPL system architecture as well as the multi-signal fusion algorithm in order to obtain benefits from TOA information. This dissertation will show that TOA information has significant advantages over TDOA information in many cases of for our application. As discussed, TOA information is generally unattainable with a unidirectional signal from a transmitter to a receiver. With an transactions of bidirectional signals between transceivers however, it is possible to attain this TOA information. Existing location systems use bidirectional signals to obtain TOA information, but only for the classical approach of one-dimensional ranging and multilateration.[13, 19]

The following chapter will discuss the theory governing the existing PPL prototype system. Subsequently, in Chapter 3 the novel extension to the PPL system, Transactional Array Reconciliation Tomography (TART), will be introduced and compared to the existing σART method using simulated signal data. Also in Chapter 3, the synchronization scheme necessary to support TART will be described. Various technical challenges that arise in the implementation of the TART approach with real system hardware will be discussed in Chapter 4. Chapter 5 will explore the behavior of TART when using received signals that are corrupted with noise, by deriving an analytic perturbation approximation of the position error for various levels of signal to noise ratio and system geometries. Finally, Chapter 6 will present the performance of TART using real data in various system tests, showing superior performance to the existing system using σART.

Chapter 2

A Multicarrier Approach to Precision Indoor Location

This chapter presents the mathematical model of an indoor RF environment and how the particular signal that our system uses extracts information from that environment, to be used to estimate the position of a unit indoors.

2.1 Channel Response

Consider an RF transmitter broadcasting a signal $x(t)$ which is received by a receiver. If the transmitter and the receiver are some distance apart r_0, then in an ideal RF environment (free space) the signal at the receiver would be a time delayed version of the original $\gamma_0 x(t - t_0)$, where $t_0 = \frac{r_0}{c}$ and γ_0 is an attenuation factor. Assuming a passive channel $\gamma_0 < 1$. If we interpret our signals in the frequency domain

$$x(t) \overset{\mathcal{F}}{\Leftrightarrow} X(\omega), \tag{2.1}$$

$$\gamma_0 x(t - t_0) \overset{\mathcal{F}}{\Leftrightarrow} \gamma_0 X(\omega) e^{-j\omega t_0}, \tag{2.2}$$

based on the properties of the Fourier transform.[23]

In an indoor RF environment however, we must use a model that takes multipath into account. Recall Figure 1.2 on page 8. We will use the convention depicted, which is that the direct path signal will be labeled signal 0 with corresponding delay t_0 and attenuation γ_0. We may have any number

of reflected signals, so we will say generally that we have N signals, and will index a particular signal with n. The received signal is a sum of these individual contributions. Therefore our discrete multipath channel model in the time domain is

$$h(t) = \sum_{n=0}^{N-1} \gamma_n \, \delta(t - t_n). \tag{2.3}$$

This function $h(t)$ is the impulse response of the channel, and $\delta(t)$ is the unit impulse function. Taking the Fourier transform we obtain the frequency response of the channel,

$$H(\omega) = \sum_{n=0}^{N-1} \gamma_n \, e^{-j\omega t_n}. \tag{2.4}$$

These functions are different representations of the same information, which will be referred to as the channel response.

This channel model is a linear system, therefore its input-output relationship can be expressed

$$r(t) = x(t) * h(t), \tag{2.5}$$

$$R(\omega) = X(\omega)H(\omega), \tag{2.6}$$

where the operator $*$ represents the convolution integral and $r(t)$, $R(\omega)$ represent the output, or received signal. [23]

2.2 Multicarrier Signal

The WPI PPL project group decided to use an RF-based location system with a signal structure quite different from GPS and Impulse Ultra-Wideband, a multicarrier approach.[14] Using this method we interpret received signals to obtain position estimates by frequency domain analysis, where these methods have been determined to be very effective in their ability to accept direct path signals and reject multipath signals. The chosen multicarrier signal consists of several unmodulated sinusoids evenly spaced in frequency.

Consider our signal, which is a sum of several sinusoids. They are evenly spaced in frequency and each sinusoid has a respective initial phase angle of θ_m.

$$x(t) = \sum_{m=0}^{M-1} e^{-j(t(\omega_0 + m\Delta\omega) + \theta_m)} \tag{2.7}$$

where we have M sinusoids spaced $\Delta\omega$ apart in frequency, and the lowest frequency sinusoid has a frequency ω_0. Taking the Fourier transform of $x(t)$ we get

$$X(\omega) = \sum_{m=0}^{M-1} \delta((\omega - (\omega_0 + m\Delta\omega))e^{j\theta_m}, \tag{2.8}$$

which is a series of impulses in the frequency domain. Figure 2.1 shows an example of what the magnitude spectrum of a Multicarrier signal with 10 carriers looks like in the frequency domain.

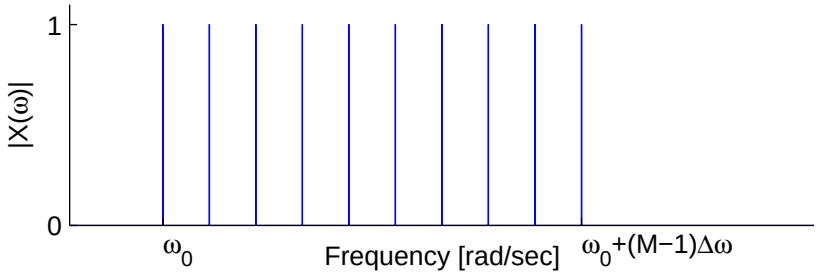

Figure 2.1: Example Multicarrer Magnitude Spectrum

Since we are able to choose the signal that is transmitted, we choose the phase angles θ_m of each carrier. Theoretically they can be arbitrary, however in practice we choose these phase angles in order to minimize the signals crest factor [8], the ratio of the signal's peak value to its average power. This is important in order to optimize the power handling capacity of the transmitter RF power amplifier.

Recall our received signal $R(\omega) = X(\omega)H(\omega)$. If $X(\omega)$ is a train of impulses, then multiplication by $H(\omega)$ is a sampling process. Thus we can consider our multicarrier signal as sampling the channel response. This reduces our carrier representation effectively to an ordered list. Our analog received signal is discretized and becomes the entry-wise product (see Table 1.2)

$$\mathbf{r} = \mathbf{x} \circ \mathbf{h}, \tag{2.9}$$

where $\mathbf{r}$, $\mathbf{x}$ and $\mathbf{h}$ are defined as

$$\mathbf{r} = \begin{bmatrix} R(\omega_0) & \dots & R(\omega_0 + \Delta\omega\, m) & \dots & R(\omega_0 + \Delta\omega\, M) \end{bmatrix}^T, \tag{2.10}$$

$$\mathbf{x} = \begin{bmatrix} X(\omega_0) & \dots & X(\omega_0 + \Delta\omega\, m) & \dots & X(\omega_0 + \Delta\omega\, M) \end{bmatrix}^T, \tag{2.11}$$

$$\mathbf{h} = \begin{bmatrix} H(\omega_0) & \dots & H(\omega_0 + \Delta\omega\, m) & \dots & H(\omega_0 + \Delta\omega\, M) \end{bmatrix}^T. \tag{2.12}$$

Similarly we will define $\boldsymbol{\omega}$ as the vector set of our carrier angular frequencies,

$$\boldsymbol{\omega} = \begin{bmatrix} \omega_0 & \dots & \omega_0 + \Delta\omega\, m & \dots & \omega_0 + \Delta\omega\, M \end{bmatrix}^T. \tag{2.13}$$

Received signals can be subsequently analyzed in this vector form.

2.2.1 Aliasing Issues

Any signal consisting of a sum of harmonically related sinusoids must be periodic. Let us consider first the simplest case, a single real sinusoid with period T

$$f_1(t) = \cos\left(\frac{2\pi t}{T}\right). \tag{2.14}$$

Since the signal repeats itself every time one period elapses, we have ambiguity on trying to assign its time delay. We can only determine the time delay modulo T. This problem is not just true of sinusoids, but any periodic function. Any Multicarrier signal with rational carrier spacing will be periodic. For example, with a two-carrier signal, if one of our sinusoids repeats itself every two seconds and the other every three seconds, then their sum will repeat itself every six seconds, see Figure 2.2. The period or aliasing window of a Multicarrier signal is determined by the least

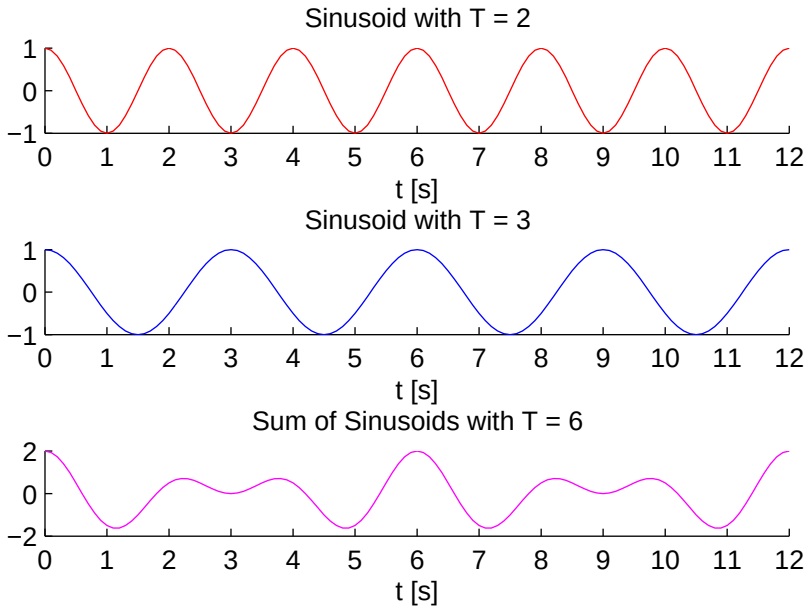

Figure 2.2: Sinusoid Periodicity

common multiple of the periods of the individual frequencies.

Alternatively we can interpret this aliasing issue in the same way one interprets aliasing with sampling signals in the time domain. The Nyquist-Shannon sampling theorem states that from samples of a continuous-time signal, the signal can be exactly reconstructed if the signal is band-limited and the sampling frequency is greater than twice the signal highest frequency in the signal. If this condition is not met, then frequency content above twice the sampling frequency is aliased back into the lower part of the band.[23]

Our situation is exactly the same, except instead of sampling signals in the time domain we are sampling signals in the frequency domain at each of our carrier frequencies. Suppose we are sampling a simple time delay channel, $H(\omega) = e^{-j\omega t_0}$. If t_0 is large relative to our carrier spacing then we will have aliasing. Thus our carrier spacing is what determines the aliasing window (or period) of our Multicarrier signal, via this equation:

$$T = 1/(2\pi\Delta\omega) = 1/\Delta f. \tag{2.15}$$

We need to ensure that this aliasing window is large enough to avoid any ambiguity. For radio waves, time delays translate into ranges via Equation 1.1. If we assume that the range from the receive antenna to the transmit antenna is less than a certain amount (several hundred meters in our problem of interest) then we can determine how large our aliasing window needs to be.

2.2.2 Software Radio Approach

The hardware implementation of the PPL system uses a software radio approach to allow us to flexibly change the parameters of our multicarrier signal. In the current version of the prototype system, the transmitted multicarrier signal consists of about 100 carriers spread over 550-700MHz. Figure 2.3 summarizes the various stages undergone by our ranging signal before it is finally analyzed at the receiving station.

Our signal originates in a discrete state in the memory of the transmitter worn by the personnel. This discrete version of our signal $x(k)$ is a digitized version of our multicarrier signal in the baseband. As discussed, the multicarrier signal is repetitive, hence we can repeatedly transmit a waveform that consists of an integer number of signal periods to produce a continuous multicarrier output. These blocks of samples, which are repeated, are called "symbols" which consist of K samples. In our current system $K = 2048$.

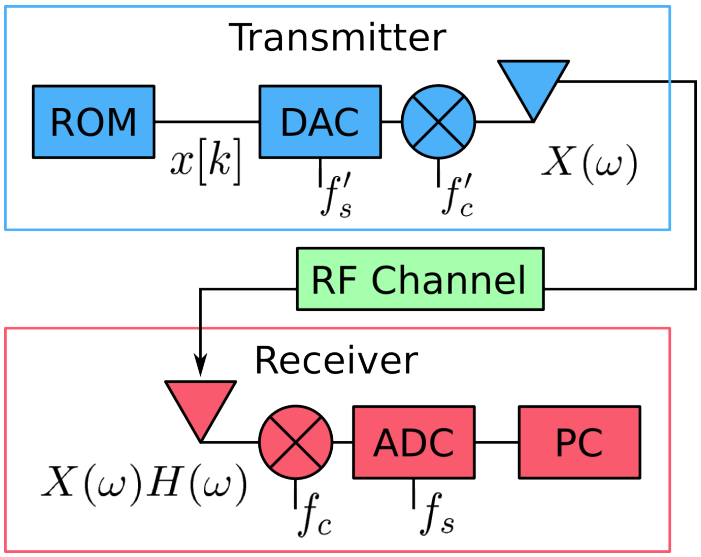

Figure 2.3: System Diagram of Software Radio Approach

Our chosen carrier frequencies are generally too high to be the direct output of an economic digital to analog converter (DAC). In the current prototype our DAC sample frequency f_s' is 400 MHz, which means that its output signal must have frequency content no higher than 200 MHz in keeping with the Nyquist sampling theorem.[23] Using our DAC generated signal and appropriate filters, we obtain a baseband (30-180 MHz) multicarrier signal which is then upconverted by an RF Mixer, a shift of f_c' = 520MHz, to the desired 550-700MHz band. After further filtering at these higher frequencies, the signal is transmitted.

After traveling through the indoor radio channel, our signal arrives at each of our receive antennas outside the building. The process on the receive side is very similar to that on the transmit side. After being captured by the antenna, the signal is filtered at RF and then downconverted using an RF mixer with nominally the same f_c = 520MHz. After baseband filtering the signal is then sampled by an analog to digital converter (ADC) at nominally the same sample rate as the DAC f_s = 400MHz. The signal in its digital state can now be sent to a computer for signal processing to make position estimates.

Figure 2.4 illustrates the system architecture of the PPL system. The mobile transmitter broadcasts the multicarrier ranging signal, which is received by multiple reference stations outside the building. This data is sent over a wireless data link to the base reference station, which analyzes

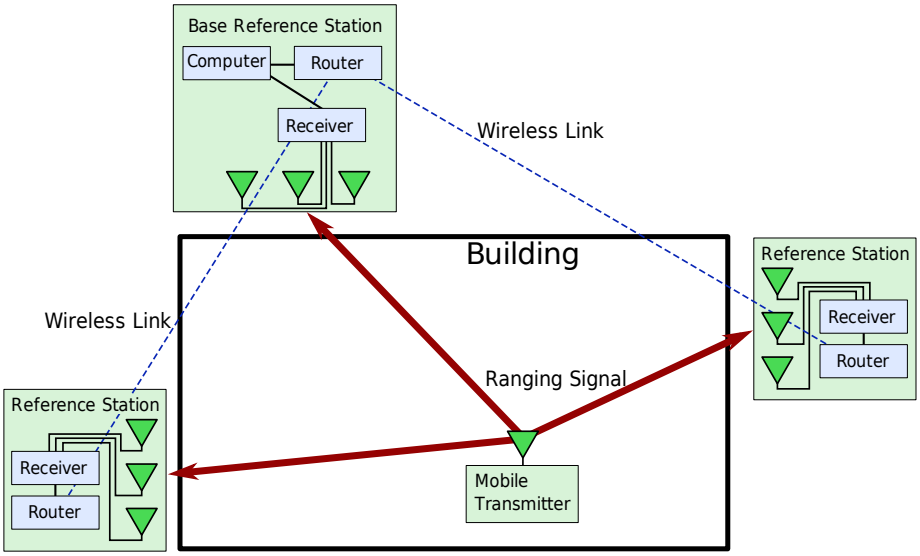

Figure 2.4: PPL System Architecture

digitized received signals in order to estimate the location of the mobile transmitter.

2.2.3 Received Signal Preprocessing

Signals received at the ADCs are also processed as symbols, blocks of K samples. All of our signal processing is done in the frequency domain, whereas our received symbols are in the time domain. For this reason our multicarrier signal was chosen with Discrete Fourier Transform (DFT) processing in mind. We use the Fast Fourier Transform algorithm (FFT) to compute the DFT, taking a discrete time signal of some K samples and convert it into a frequency domain representation. The spectral energy of the signal is distributed into K frequency bins.

Consider a sampled time domain signal of K samples at a sampling frequency f_s. If the DFT is performed on this signal then K frequency bins are created. These bins represent frequencies evenly spaced from $\frac{-f_s}{2}$ to $\frac{f_s}{2}$, with a spacing of $\frac{f_s}{k}$. The complex values in these bins represent the magnitude and phase of positive and negative frequencies up to half of the sampling frequency.[23]

If a sinusoid in the time signal has an exact frequency corresponding to one of the frequency bins, then all of its energy will be present in that bin. If the frequency is not precisely a bin frequency, then most of the energy will be present in the closest bin but some of the energy will reside in neighboring bins. This is known as leakage, and can reduce signal to noise ratio and also cause

sinusoids of different frequencies to interfere with each other, muddling the underlying information. Figure 2.5 shows this behavior, where we can see one case where the DFT was taken of a signal with the exact frequency of a DFT bin; this contrasts with another signal with the same amplitude wherein the frequency is in between two bins. We can see the energy has leaked into neighboring bins.

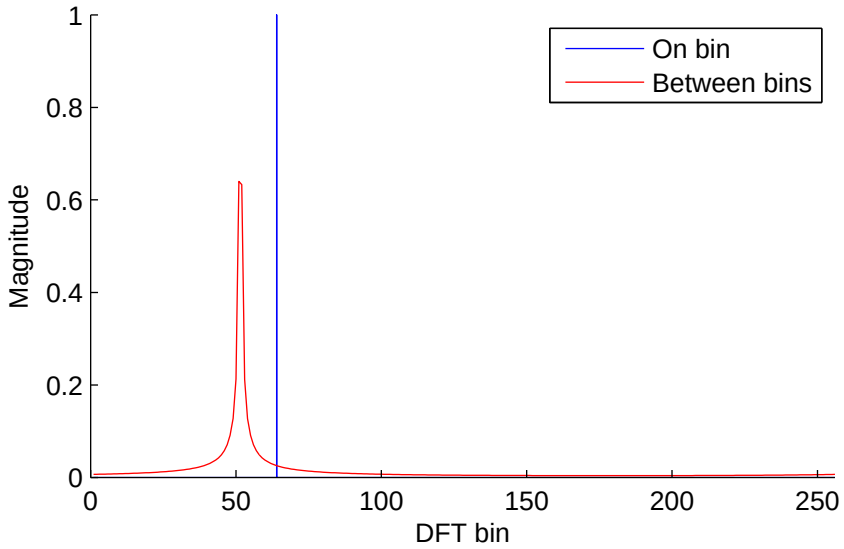

Figure 2.5: Magnitude of DFT Output for Frequencies on and off DFT bins

We chose our carrier spacing carefully such that it is an integer number of DFT bins, and the mixer frequency by which we downconvert, such that our multicarrier signal frequencies are centered on the DFT bins to minimize leakage. That means that after we take the DFT of our sampled signal the magnitude and phase of our received signal carriers are directly represented in the appropriate bins, which are indexed to form the received signal vector $\mathbf{r}$.

2.3 Effects of Non-Ideal Synchronization

Unfortunately in our real world system the sample and mixer frequencies do not perfectly match on the transmit and receive sides. This is due to the fact that our transmitter must be a wireless unit driven by its own oscillator, which itself can not be overly expensive. The result is that there is generally a mismatch and significant frequency drift between the mixer frequencies as well as sample clock frequencies. Furthermore the frequency of each oscillator is stochastically time-varying due

to thermal fluctuations.

$$f_s(t) \neq f_s'(t) \tag{2.16}$$

$$f_c(t) \neq f_c'(t) \tag{2.17}$$

There are ways to share a common frequency reference instead of having to depend upon independent oscillators; a master frequency beacon could be transmitted over the air for the transmitter to use. Multipath causes problems with this approach however, as it is possible for the transmitter to be at a location where the direct path and a reflected path happen to superimpose destructively resulting in signal loss. This is unacceptable for our application. While transmitting a single frequency over the air presents the problem just discussed, it may be possible to transmit a more complicated signal, such as a multicarrier signal, and assure that there will always be frequency content for the transmitter to lock onto, thanks to the frequency dependence of multipath channels. Such approaches require that our transmitter has the capability of receiving such a signal and processing it, which would add to the hardware requirements. Also a unit receiving a beacon signal may not be able to differentiate motion induced Doppler effects from a drifting frequency reference.

2.3.1 Sample Clock Drift

Let us first consider issues caused by sample clock drift. In the current hardware configuration that our system uses, we have our software radio transmitter using one sample clock with rate f_s' and our receiving ADCs running on another independent sample clock with rate f_s. The ideal sample clock frequency chosen for our system is 400 MHz. The transmitter's sample clock comes from a crystal oscillator (FOX924B-10) with 2.5 ppm of frequency drift.[16] The receive ADCs have a sample clock derived from a Rubidium atomic oscillator with less than 0.01 ppm of frequency drift. The relative drift between the two clocks is approximately 2.5 ppm in the worst case.

Consider what happens when we generate our waveform with a different sampling frequency than with which we receive it. If our transmitter's sample clock frequency f_s' is faster or slower than the desired frequency f_s, then the signal generated will be accordingly compressed or stretched in time. Similarly on the receiving end, if the ADCs' sample clock is faster or slower than desired then the recorded signal will appear stretched or compressed accordingly. What ultimately determines the stretch/compression of the received signal is the difference in frequency between the transmit

sample clock and the receive sample clock.

Since our concern is with the relative frequency drift between the two clocks, we will treat the receive sample clock as the reference frequency about which the transmit sample clock drifts. Our worst case difference in frequency leads to a ratio of

$$\frac{f_s'}{f_s} = 1 \pm 2.5 \cdot 10^{-6}. \tag{2.18}$$

This means that the duration of the symbols transmitted and recorded by the ADCs will be slightly different. The reference symbol duration of the receive ADCs

$$T = \frac{a}{f_s}, \tag{2.19}$$

where a is a proportionality constant. The period of the symbols from the transmitter DAC is

$$T' = \frac{a}{f_s'}. \tag{2.20}$$

Hence in the worst case we have

$$\frac{f_s'}{f} = \frac{T'}{T} = 1 \pm 2.5 \cdot 10^{-6}. \tag{2.21}$$

For each symbol of data we use $K = 2048$ samples at 400 MHz so $T = 5.12\mu s$. The transmitted symbol duration is then at most

$$T' = T(1 + 2.5 \cdot 10^{-6}) = 5.12001280\mu s, \tag{2.22}$$

and at least

$$T' = T(1 - 2.5 \cdot 10^{-6}) = 5.11998720\mu s. \tag{2.23}$$

The difference in symbol duration is at most 25.6 ps. This difference is small enough not to affect the output of our FFT and thus can be ignored. This was proven in a previous thesis conducted and written in support of this project.[9]

Assuming a transmit symbol and receive symbol start at the same time, the drift between the two sample clocks does not cause a problem since they end at the same time within 25.6 ps which we have accepted as negligible. The next pair of symbols however will not start at exactly the same time, as these errors build up after several symbol periods. Figure 2.6 illustrates this behavior, though in a more extreme case for illustrative reasons, where $\frac{T}{T'} = 1.2$, so the symbols become

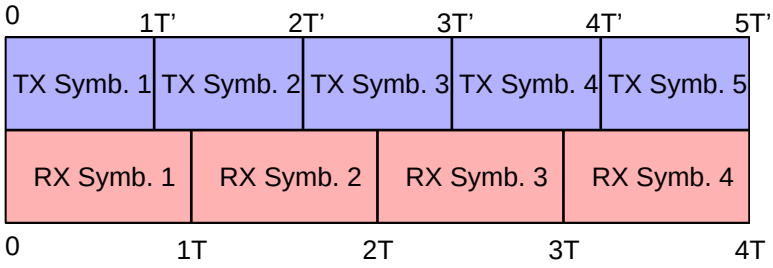

Figure 2.6: Temporal Symbol Alignment

misaligned after just a few symbol periods. In our case the symbols can become misaligned by at most 25.6 ps every symbol period, so that our symbols can be completely misaligned (offset by $\frac{T}{2}$) after as few as 100,000 symbol periods, which is 0.512 seconds. Thus in a short amount of time (relative to our real-time operation) the transmitted symbols can become completely misaligned from the receive symbol window. Since the ratio $\frac{f_s'}{f_s}$ depends on random wandering of the clock frequencies, we must accept that there will be a random time-varying time-offset $\tilde{\tau}(t)$ between the transmit and receive window. We may approximate $\frac{f_s'}{f_s}$ to be constant over small enough periods of time (on the order of tens of symbols), but over large periods of time it must be recognized that it changes randomly. When working with received signals captured close enough in time to make this approximation, we will use the shorthand $\tilde{\tau}$ and assumed the value to be a random constant. As result of this model reduction our received signals can be more fully modeled:

$$\mathbf{r} = R(\omega) = X(\omega)H(\omega)e^{-j\omega\tilde{\tau}}. \tag{2.24}$$

Since the drift is unknown, we record symbols at our receive ADCs with unknown time-offsets, while our means to determine position estimates is based upon the relative time of arrival of our signals. This may seem to undermine the hopes of using our received data to estimate position, but while the absolute distance information in each received symbol has been destroyed by $\frac{f_s'}{f_s} \neq 1$, there remains relative distance information between the received signals from several receivers that can be used to estimate position. For this reason our current system is described as a Time Difference of Arrival (TDOA) system, as opposed to a Time of Arrival (TOA) system.

2.3.2 Mixer Frequency Drift

The purpose of an RF mixer is to shift the frequency content of a signal by some constant value. The dual of the time delay property of the Fourier transform, the frequency shift property is

$$x(t)e^{-jt\omega_c} \overset{\mathcal{F}}{\Leftrightarrow} X(\omega - \omega_c). \tag{2.25}$$

Based upon this, RF mixers operate by multiplying an input signal by an sinusoid with the desired shift frequency. As discussed, our system uses RF mixers in our transmitter units as well as our receiver units.

Our mixer frequencies f_c and f_c' are derived from the same source oscillator as our sample clocks so their accuracies with respect to one another are the same, about 2.5 ppm worst case. The shift frequency used by our current system is 730 MHz. Our two mixer frequencies therefore have a worst case difference of 1.8 kHz. In comparison, the frequency spacing of our DFT bins is 195.1 kHz. This results in our carriers remaining very close to the center of their respective DFT bins with minimal leakage.

The magnitude of our received signal is not affected significantly by mixer frequency offset and drift; this is not true however of the phase. The issue arises from the fact that the mixer oscillators on the transmit and receive sides are not synchronized, and thus go in and out of phase unpredictably with one another in the same way that our symbols do, as depicted in Figure 2.6.

Ideally a signal that is upconverted with one mixer, and subsequently downconverted with another mixer would reproduce the original signal.

$$r_{bb}(t) = x_{bb}(t)e^{-jt\omega_c}e^{jt\omega_c} \tag{2.26}$$

$$r_{bb}(t) = x_{bb}(t)e^{-jt(\omega_c-\omega_c)} \tag{2.27}$$

$$r_{bb}(t) = x_{bb}(t)e^{-jt0} \tag{2.28}$$

$$r_{bb}(t) = x_{bb}(t) \tag{2.29}$$

If however the two mixers are out of phase, with phases $\tilde{\theta}_t(t)$ on the transmit side and $\tilde{\theta}_r(t)$ on the receive side, we observe the following:

$$r_{bb}(t) = x_{bb}(t)e^{-j(t\omega_c+\tilde{\theta}_t(t))}e^{j(t\omega_c+\tilde{\theta}_r(t))} \tag{2.30}$$

$$r_{bb}(t) = x_{bb}(t)e^{-jt\omega_c}e^{jt\omega_c}e^{j\overbrace{\left(\tilde{\theta}_r(t)-\tilde{\theta}_t(t)\right)}^{\tilde{\theta}(t)}} \tag{2.31}$$

$$r_{bb}(t) = x_{bb}(t)e^{j\tilde{\theta}(t)} \tag{2.32}$$

Thus the effect of unsynchronized mixers on our received signal is a phase offset $\tilde{\theta}$, which is time-varying but constant across frequency. For simplicity of notation, we substituted $\tilde{\theta}$ for $\tilde{\theta}_r(t) - \tilde{\theta}_t(t)$. Just like our sample clock drift term $\tilde{\tau}(t)$, $\tilde{\theta}(t)$ is time-varying, yet for short enough time periods can be assumed to be constant. Again, the unpredictable relationship between transmit and receive oscillators means that $\tilde{\theta}$ is considered to be random.

Combining the effects of sample clock drift and mixer drift, we can present a more complete model of our received signal,

$$r(t) = x(t-\tilde{\tau}) * h(t-\tilde{\tau})e^{j\tilde{\theta}}, \tag{2.33}$$

$$\mathbf{r} = R(\boldsymbol{\omega}) = X(\boldsymbol{\omega})H(\boldsymbol{\omega})e^{-j(\boldsymbol{\omega}\tilde{\tau}-\tilde{\theta})}. \tag{2.34}$$

Thus we observe two non-ideal synchronization effects on our received signals, a random time-offset $\tilde{\tau}$ and a random frequency independent phase offset $\tilde{\theta}$.

2.4 Singular Value Array Reconciliation Tomography

We have now presented our model for received signals; the next issue to be addressed is how the PPL system processes these received signals in order to obtain an estimate of the transmitter location. The precision location algorithm developed within the WPI PPL project that is currently used in our system was named Singular Value Array Reconciliation Tomography (σART). This novel algorithm obtains a position estimate directly with received data from all of the receive antennas, rather than determining the ranges from the transmitter to each receive antenna independently followed by a multilateration solution of the indicated source position.

2.4.1 Rephasing

σART is an exhaustive algorithm. The entire space that the transmitter may reside in is discretized as a grid with some spatial resolution. This grid is scanned and a metric is evaluated at each scan location in the grid. Our metric is chosen such that in a zero noise, no multipath scenario it is

maximized at the transmitter location. The sampling density of the grid is chosen based upon the bandwidth of our multicarrier signal. The spatial resolution of the location of the maximum may also be increased using interpolation techniques after the completion of the σART scan.

To describe this process, we start with our frequency domain data $\mathbf{r}_p$, the received signal vectors from a total of P receive antennas. These vectors form the columns in our raw data matrix $\mathbf{R}$, with one column for each receive antenna.

$$\mathbf{R} = \left[\begin{array}{cccc} \mathbf{r}_1 & \dots & \mathbf{r}_p & \dots & \mathbf{r}_P \end{array} \right] \tag{2.35}$$

At each point in space which is scanned, the distance from that location to each of the receive antennas is determined from the known locations of the receive antennas. Figure 2.7 illustrates this procedure. The left side of Figure 2.7 shows the ideal behavior of our transmitted signal in which

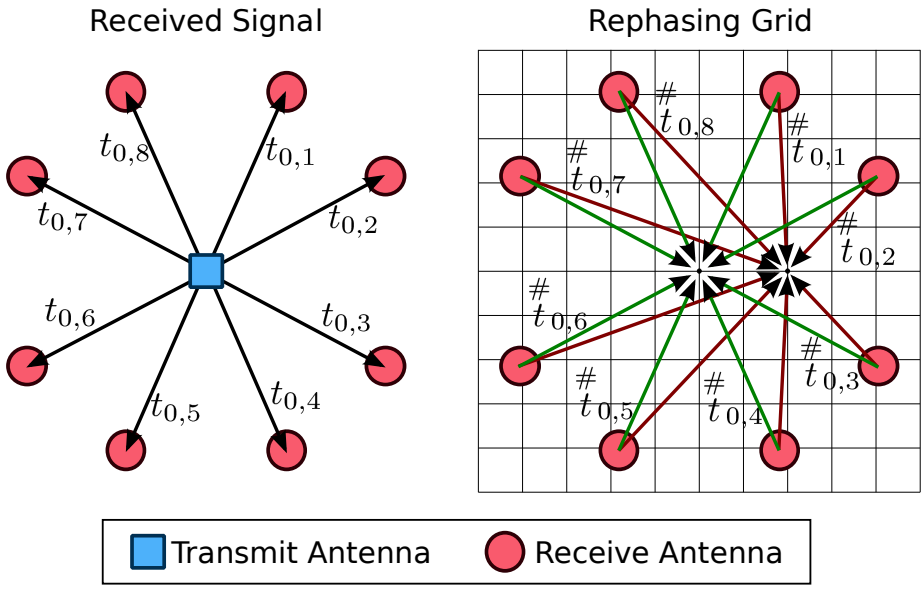

Figure 2.7: Rephasing Procedure

only a direct path signal is present. In this case the signal simply gets delayed as it propagates from the transmit antenna to the receive antennas, with a different delay $t_{0,1}, t_{0,2}, \dots t_{0,P}$ determined by the range from the transmitter to each receiver via Equation 1.1. The space that the transmitter may be located within is scanned in a grid pattern as depicted on the right side of Figure 2.7. At each scan location the ranges from the scan location to the receive antennas is computed, and then the corresponding values $\overset{\#}{t}_{0,1}, \overset{\#}{t}_{0,2}, \dots \overset{\#}{t}_{0,P}$ are the hypothetical time delays of the direct path signal

which will subsequently be tested. The hypothetical time delay

$$\overset{\#}{t}_{0,p} = \frac{\left\| \overset{\#}{\mathbf{v}}_l - \mathbf{v}_p \right\|}{c} \tag{2.36}$$

represents the time delay a direct path signal would undergo traveling from the mobile locator position $\mathbf{v}_l$ to the pth reference antenna location $\mathbf{v}_p$, where $\|\cdot\|$ represents the Euclidean norm.

Next the received data matrix $\mathbf{R}$ has the hypothetical time delays inversely applied to all its columns. This is performed by multiplying our frequency data by a complex exponential term. This is an entry-wise multiplication, which was described in Table 1.2. This operation undoes the time delay that would have been applied to the data by propagating through free space if the transmitter was at that location. So for every point in space we have a different "rephased" version of $\mathbf{R}$ we'll denote $\mathbf{R}'$, where

$$\mathbf{R}' = \left[\begin{array}{cccc} \mathbf{r}_1 \circ e^{j\omega \overset{\#}{t}_{0,1}} & \dots & \mathbf{r}_p \circ e^{j\omega \overset{\#}{t}_{0,p}} & \dots \quad \mathbf{r}_P \circ e^{j\omega \overset{\#}{t}_{0,P}} \end{array} \right]. \tag{2.37}$$

An important point to make is that this rephasing does not change the "energy" or Frobenius Norm of the matrix. The Frobenius norm of a matrix $\mathbf{A}$ with b elements, regardless of shape is defined as [31]

$$\|\mathbf{A}\|_F = \sqrt{\sum_{a=1}^{b} |(\mathbf{A})_a|^2}. \tag{2.38}$$

Since the rephasing only affects the phase, and not the magnitude of the elements of $\mathbf{R}$, we can conclude that the energy in the matrix remains constant as $\mathbf{R}$ is rephased to create $\mathbf{R}'$.

2.4.2 The First Singular Value

At each location an operation is performed on $\mathbf{R}'$ to obtain a metric indicating how strongly that location is judged as a potential position estimate, meaning the consistency of the rephased data with the ideal signal structure for that location. The metric is the first singular value of $\mathbf{R}'$.

Let us assume momentarily that our system has ideal synchronization, $\tilde{\theta} = \tilde{\tau} = 0$. Thus the received signal for antenna p is simply the channel response vector $\mathbf{h}_p$, which we know to consist of our multipath model.

$$\mathbf{r}_p = \mathbf{h}_p = \sum_{n=0}^{N_p-1} \gamma_{n,p}\, e^{-j\omega t_{n,p}} = \overbrace{\gamma_{0,p}\, e^{-j\omega t_{0,p}}}^{\text{direct path}} + \sum_{n=1}^{N_p-1} \gamma_{n,p}\, e^{-j\omega t_{n,p}} \tag{2.39}$$

Above the multipath model is rewritten such that the direct path term is separated from the paths due to reflections.

If our received signal is simply $\mathbf{h}_p$, then our rephased matrix

$$\mathbf{R}'_{ideal} = \left[\ldots \; \gamma_{0,p}\, e^{j\boldsymbol{\omega}(\overset{\#}{t}_{0,p} - t_{0,p})} + e^{j\boldsymbol{\omega}\overset{\#}{t}_{0,p}} \circ \sum_{n=1}^{N_p-1} \gamma_{n,p}\, e^{-j\boldsymbol{\omega}t_{n,p}} \; \ldots \right]. \tag{2.40}$$

The above equation is denoted $\mathbf{R}'_{ideal}$, representing the rephased matrix under ideal synchronization. We see that each column is a sum of complex sinusoids. We can say that generally the periodicities of these sinusoids are unrelated. The time delays associated with the multipath signals, as well as the time shift $\overset{\#}{t}_{0,p}$ at an arbitrary location have no particular relation to one another. Thus the columns of $\mathbf{R}'_{ideal}$ generally have low correlation.

At the correct test location however, we have the special case that $t_{0,p} = \overset{\#}{t}_{0,p}$ for all antennas. Thus the direct path term in each columns is multiplied by $e^{j\boldsymbol{\omega}\left(\overset{\#}{t}_{0,p} - t_{0,p}\right)} = e^{j\boldsymbol{\omega}0} = \mathbf{1}_{M\times 1}$. This simplifies to

$$\overset{\star}{\mathbf{R}}'_{ideal} = \left[\ldots \; \gamma_{0,p}\mathbf{1}_{M\times 1} + e^{j\boldsymbol{\omega}\overset{\#}{t}_{0,p}} \circ \sum_{n=1}^{N_p-1} \gamma_{n,p}\, e^{-j\boldsymbol{\omega}t_{n,p}} \; \ldots \right]. \tag{2.41}$$

We observe that each column has the term $\gamma_{0,p}$ that is constant across frequency, which can be referred to as a direct current (DC) component by virtue of its constancy, when scanned to the correct location. The presence of this DC component in each column causes the correlation of the columns to grow as well as the first singular value.[31] If one considers the reflection free case, each column is simply $\gamma_{0,p}\mathbf{1}_{M\times 1}$, which clearly results in a rank 1 matrix with all of the energy in the first singular value. The presence of reflected signals with unrelated periodicities in the rephased matrix cause the direct path to be the main contributor to the first singular value. In this fashion σART attempts to ignore reflected signals.

Next we will remove the simplifying assumption that we have perfect synchronization. Re-introducing our non-ideal synchronization term, our received signal at each antenna is

$$\mathbf{r}_p = \mathbf{h}_p \circ e^{-j(\boldsymbol{\omega}\tilde{\tau} + \tilde{\theta}_p)}. \tag{2.42}$$

The random time-offset $\tilde{\tau}$ affects the phase of the received signal as a trend across frequency (our columns), yet is constant for each receive antenna, so it can be expressed as the pre-multiplication

of a diagonal matrix. Similarly the random frequency independent phase offset $\tilde{\theta}_p$ is constant across frequency but varies for each receive antenna, so it can be represented as a post-multiplication term.

$$\mathbf{r}_p = \begin{bmatrix} e^{-j(\boldsymbol{\omega})_1\tilde{\tau}} & \dots & 0 \\ \vdots & \ddots & 0 \\ 0 & 0 & e^{-j(\boldsymbol{\omega})_M\tilde{\tau}} \end{bmatrix} \mathbf{h}_p \begin{bmatrix} e^{j\tilde{\theta}_1} & \dots & 0 \\ \vdots & \ddots & 0 \\ 0 & 0 & e^{j\tilde{\theta}_P} \end{bmatrix} \tag{2.43}$$

The reason $\tilde{\theta}_p$ differs by receive antenna is because in our system each receive antenna has its own mixer oscillator, each drifting relative to the transmitter oscillator. There may also be differing random time-offsets $\tilde{\tau}_p$ on different receive antennas, however σART assumes this is not the case. Received data with any differing time-offsets between receive antennas would need to be rectified before it could be used with σART. This problem has been a major research topic over the past several years for myself. This problem is detailed in my Master's Thesis[2] and a recent conference presentation[3].

Similarly to Equation 2.43 we can also express the non-ideal rephased matrix $\mathbf{R}'$ in terms of ideal $\mathbf{R}'_{ideal}$.

$$\mathbf{R}' = \begin{bmatrix} e^{-j(\boldsymbol{\omega})_1\tilde{\tau}} & \dots & 0 \\ \vdots & \ddots & 0 \\ 0 & 0 & e^{-j(\boldsymbol{\omega})_M\tilde{\tau}} \end{bmatrix} \mathbf{R}'_{ideal} \begin{bmatrix} e^{j\tilde{\theta}_1} & \dots & 0 \\ \vdots & \ddots & 0 \\ 0 & 0 & e^{j\tilde{\theta}_P} \end{bmatrix} \tag{2.44}$$

It can be shown that both of these diagonal matrices are unitary. Consider some diagonal matrix with unit magnitude elements and arbitrary phases:

$$\mathbf{A} = \begin{bmatrix} e^{j\phi_1} & \dots & 0 \\ \vdots & \ddots & 0 \\ 0 & 0 & e^{j\phi_B} \end{bmatrix} \tag{2.45}$$

The matrix $\mathbf{A}$ is unitary if $\mathbf{A}\mathbf{A}^H = \mathbf{I}$, where $\mathbf{A}^H$ is the Hermitian conjugate transpose operation.

$$\begin{aligned} \mathbf{A} &= \begin{bmatrix} e^{j\phi_1} & \dots & 0 \\ \vdots & \ddots & 0 \\ 0 & 0 & e^{j\phi_B} \end{bmatrix} \begin{bmatrix} e^{-j\phi_1} & \dots & 0 \\ \vdots & \ddots & 0 \\ 0 & 0 & e^{-j\phi_B} \end{bmatrix} \\ &= \begin{bmatrix} e^{j(\phi_1-\phi_1)} & \dots & 0 \\ \vdots & \ddots & 0 \\ 0 & 0 & e^{j(\phi_B-\phi_B)} \end{bmatrix} = \begin{bmatrix} 1 & \dots & 0 \\ \vdots & \ddots & 0 \\ 0 & 0 & 1 \end{bmatrix} = \mathbf{I} \end{aligned} \tag{2.46}$$

Thus the two diagonal matrices used in Equation 2.43 are also unitary.

Unitary matrices have the property that multiplication of a matrix by a unitary matrix retains the singular values of the original matrix.[17] Thus the singular values of $\mathbf{R}'$ must be the same as $\mathbf{R}'_{ideal}$. This means that σART is unaffected by these two synchronization effects, which is one of the reasons why the first singular value was chosen as our search metric.

Because of this property, σART ignores any constant time-offset on all receive antennas' data. This is a beneficial property in that we ignore the effects of sample clock drift. This also implies however that any absolute distance information from a particular receive antenna is ignored, and σART bases its position estimates on relative distance information from the different receive antennas. In this way σART is fundamentally a Time Difference of Arrival approach.

Figure 2.8 displays the outcome of the σART algorithm using ideal simulated data. The spatial scan for this two-dimensional simulation consisted of a horizontal plane at the height of the antenna. The circular markers represent 16 receive antenna locations, while the square marker represents the transmitter location. An "X" marker represent the location of the σART solution at the transmitter location. The background image represents the value of the σART metric, with blue being the lowest and red being the strongest. These graphical conventions will be used consistently with subsequent plots. We observe that the σART metric in this case indeed has a peak at the transmitter location.

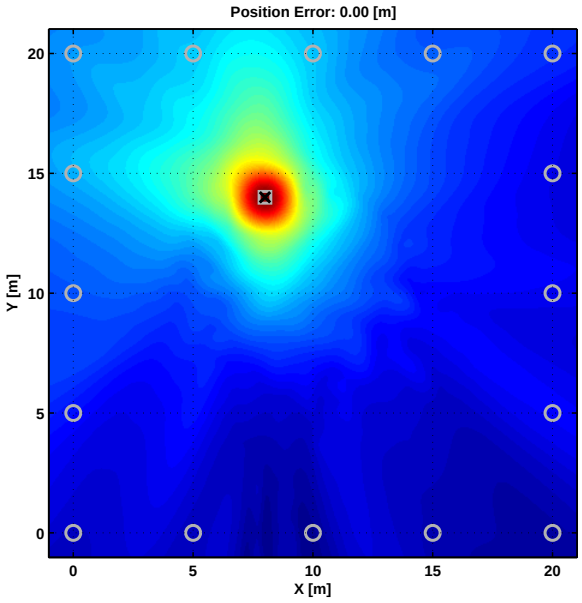

Figure 2.8: Ideal σART Simulation

σART is currently implemented and used by the real-time WPI PPL system. It has produced accurate results with real data in various environments, and is considered the current state of the art in precision indoor location.

Chapter 3

Transactional Array Reconciliation Tomography

Ever in pursuit of avenues to improve our system, it is often useful to question the assumptions on which an approach is based, and even explore the ramifications of these not being true. Such was the origin of Transactional Array Reconciliation Tomography (TART), the contribution of this dissertation.

3.1 TART Algorithm

The assumption challenged was that our received signals must be subject to a random time-offset $\tilde{\tau}$. What if there were no random time-offset on received data? With $\tilde{\tau} = 0$ our received signals would have TOA-like synchronization. Reconsidering our rephased received signal matrix,

$$\mathbf{R}' = \mathbf{R}'_{ideal} \begin{bmatrix} e^{j\tilde{\theta}_1} & \dots & 0 \\ \vdots & \ddots & 0 \\ 0 & 0 & e^{j\tilde{\theta}_P} \end{bmatrix}. \tag{3.1}$$

We can then remove the premultiplication matrix that applied the random time-offset and simply apply a random frequency independent phase offset on each column of the $\mathbf{R}'_{ideal}$.

In Equation 2.41 we observed a constant term across frequency when rephased to the correct location with ideal data. Once the non-ideal synchronization was considered, this DC component

was shifted to some random frequency by the random time-offset. With $\tilde{\tau} = 0$ however, our DC term remains, albeit with a random frequency independent phase term applied to each column.

$$\overset{\star}{\mathbf{R}}' = \left[\ldots \gamma_{0,p} e^{j\tilde{\theta}_p} \mathbf{1}_{M\times 1} + e^{j(\overset{\#}{\boldsymbol{\omega}} t_{0,p} + \tilde{\theta}_p)} \circ \sum_{n=1}^{N_p - 1} \gamma_{n,p}\, e^{-j\boldsymbol{\omega} t_{n,p}} \ \ldots \right]. \tag{3.2}$$

We can therefore evaluate a metric more directly than by using the first singular value, by computing the DC component of each column.

If we take the sum of the columns of our rephased matrix, the DC terms will add constructively (in phase), whereas the other sinusoids will average out to zero, assuming a large signal bandwidth. This issue of bandwidth will be discussed further in Section 3.2.2.

$$\mathbf{1}_{1\times M}\ \overset{\star}{\mathbf{R}}' = M \left[\ \gamma_{0,1} e^{j\tilde{\theta}_1} \ldots \gamma_{0,p} e^{j\tilde{\theta}_p} \ldots \gamma_{0,P} e^{j\tilde{\theta}_P} \ \right] \tag{3.3}$$

We can then take the absolute value of each element (the "elm" operation defined in Table 1.2) to get the magnitude of the DC term.

$$\mathrm{elm}(\mathbf{1}_{1\times M}\ \overset{\star}{\mathbf{R}}') = M \left[\ \gamma_{0,1} \ldots \gamma_{0,p} \ldots \gamma_{0,P} \ \right] \tag{3.4}$$

We then sum those terms in order to get a measure of the DC present in all columns, which is the metric for Transactional Array Reconciliation Tomography (TART).

$$\mathrm{elm}(\mathbf{1}_{1\times M}\ \overset{\star}{\mathbf{R}}')\mathbf{1}_{P\times 1} = M \left[\gamma_{0,1} + \ldots \gamma_{0,p} + \ldots \gamma_{0,P} \right] \tag{3.5}$$

The scale factor M is a constant which would scale the value of the TART metric the same amount at all scan locations, not changing the location of the global maximum, which is the position estimate.

The allowed random phase offset on different antennas accommodates data which is not coherent, a freedom not allowed by traditional phased array techniques.[6]

3.2 Simulated Results

An alternative approach to σART has been proposed, TART, which assumes $\tilde{\tau} = 0$ and uses an alternative metric computation. This section will illustrate advantageous properties that TART has compared to σART, using simple cases with simulated signal data.

First we will re-examine the case depicted in Figure 2.8, in which ideal data with no reflections was received by 16 receive antennas surrounding a test area. The effects of distance based amplitude

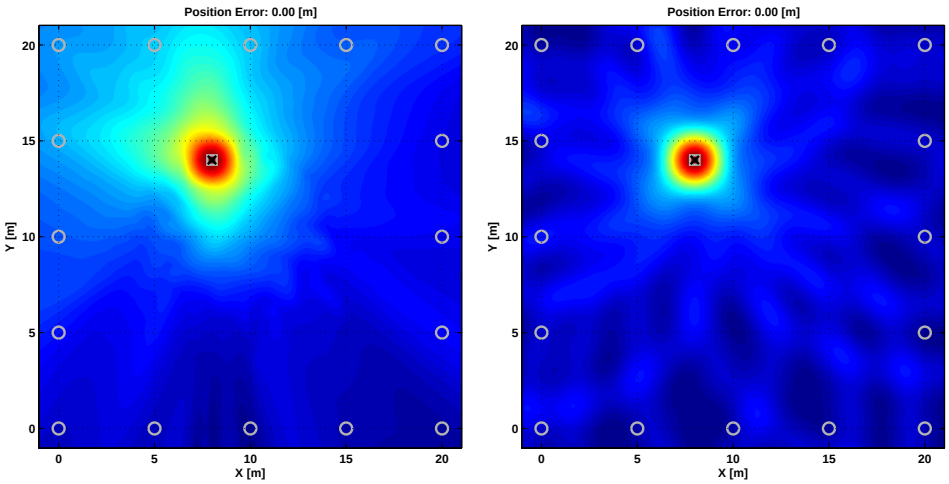

(a) σART (b) TART

Figure 3.1: σART vs. TART - Ideal Simulation

decay is ignored, $\gamma = 1$. Figure 3.1 shows this case using both σART and TART. We see that both metrics have a peak at the correct location, with no error in this ideal case. The images of the metrics are slightly different, but there is no clear indication of which approach is preferable.

3.2.1 Reflectors

Next we will consider the effects of introducing an ideal omnidirectional reflector. In this case the received signal at each receiver will consist of the sum of two paths with different delays. First, the direct path $t_{0,p}$ (the delay undergone from the transmitter to receiver) and then the reflected path $t_{1,p} = \Delta_1 + \Delta_{2,p}$ (the delay undergone from the transmitter to the reflector Δ_1 in addition to the delay undergone from the reflector to each receiver $\Delta_{2,p}$).

$$\mathbf{r}_p = \mathbf{x} \circ \left(e^{-j\boldsymbol{\omega} t_{0,p}} + e^{-j\boldsymbol{\omega}(\Delta_1 + \Delta_{2,p})} \right) e^{j\tilde{\theta}_p} \tag{3.6}$$

As discussed previously, it is expected that both σART and TART will have a maximum at the location of the transmitter even in the presence of multipath. Let us consider for this case what happens when scanned to the location of the reflector, $\overset{\#}{t}_{0,p} = \Delta_{2,p}$.

$$\overset{\Delta}{\mathbf{R}}' = \left[\ldots \; e^{-j(\boldsymbol{\omega}(t_{0,p} - \Delta_{2,p}) + \tilde{\theta}_p)} + e^{-j(\boldsymbol{\omega}\Delta_1 + \tilde{\theta}_p)} \; \ldots \right]. \tag{3.7}$$

We observe that the reflected signal component becomes a sinusoid with a frequency that the same in all columns. This causes the first singular value to be large and a maximum in the σART metric.

Since the reflected signal component is not DC, TART will not identify the reflector location as a maximum.

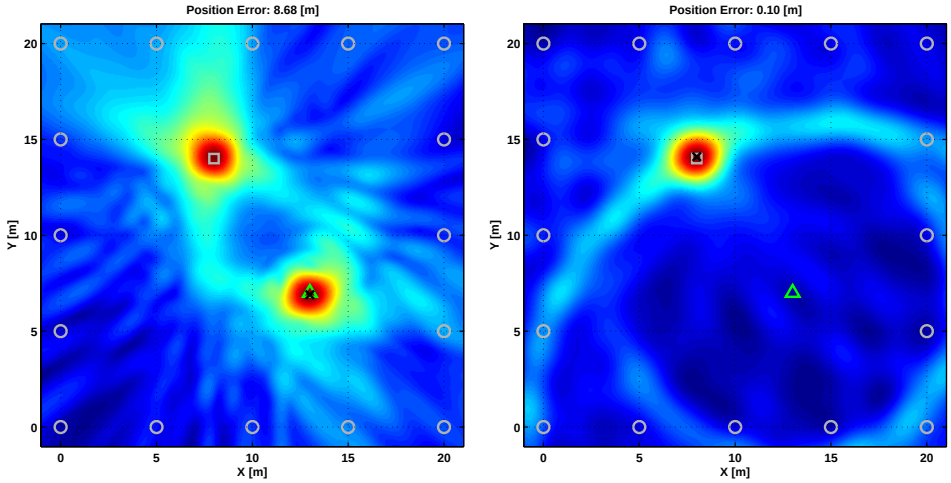

(a) σART (b) TART

Figure 3.2: σART vs. TART - Single Reflector Simulation

This behavior is illustrated in Figure 3.2 which shows a simulation result with an omnidirectional reflector as described. The reflector location (marked with a triangle) indeed shows a maximum at both the transmitter and reflector location for σART, whereas TART does not identify the reflector location as a maximum. Indeed, the simulation actually chose the incorrect peak yielding a 8.68 meter error. The TART result shows an error of 0.10 meters; it is important to note that the presence of multipath does have an degradative effect on the accuracy of TART, however the performance in this case is clearly preferable to σART.

Figure 3.3 shows a more drastic example with six reflectors randomly distributed throughout the test region. We see again that σART fails to identify the correct solution and has a gross error of 10.77 meters. TART avoids identifying reflectors as maxima and yields a much smaller 0.40 meter error.

3.2.2 Bandwidth

When describing the computation of the TART metric it was mentioned that any AC terms present in the rephased matrix would have an average value of zero. This is only true if the AC sinusoids happen to have an integer number of periods in the window sampled by our multicarrier

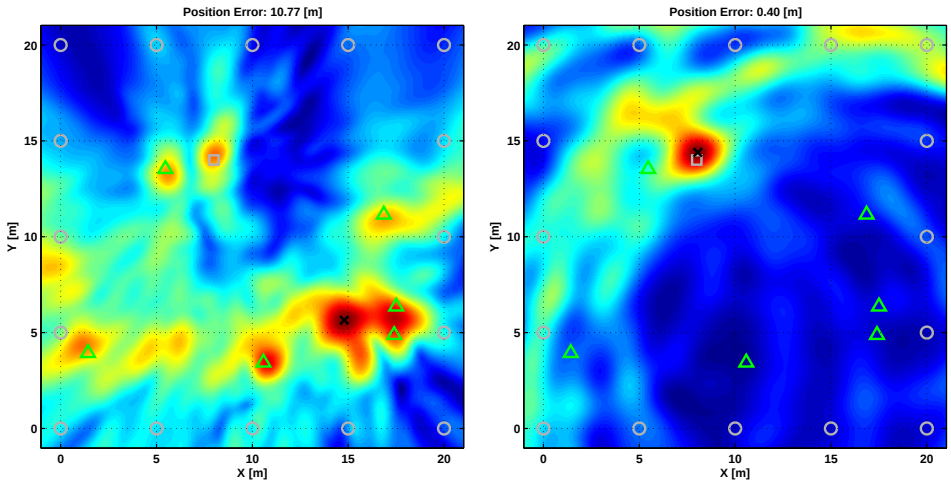

(a) σART (b) TART

Figure 3.3: σART vs. TART - Multi-Reflector Simulation

signal, or in the ideal case of an infinitely large window (infinite bandwidth). Using finite bandwidth signals in our real system causes the AC components to not be orthogonal to DC, but to have some finite correlation. This is the reason why the metric images presented thus far do not have peaks that are infinitely narrow. The width of these peaks is proportional to the bandwidth of the multicarrier signal.

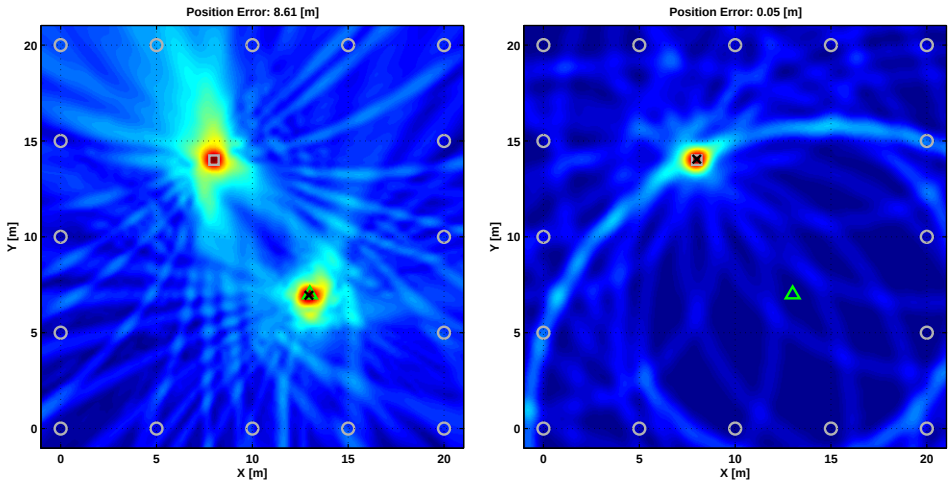

(a) σART (b) TART

Figure 3.4: σART vs. TART - Single Reflector Simulation with Double Bandwidth

Figure 3.4 shows the same single reflector case as Figure 3.2, with the only change being that

the bandwidth of the multicarrier signal was doubled. We observe that for both σART and TART the peaks in the metric images become tighter. The position estimation error for TART also is reduced by one half as well. The cause of the error is the lack of true orthogonality between the reflected signal components and the direct path components in the rephased matrix. Increasing the bandwidth makes them more orthogonal and more separable.

Thus, increasing the bandwidth has desirable effects on performance, and is a parameter of the system that should be maximized. Factors limiting the amount of possible bandwidth of the system are RF design challenges (circuits, antennas) and spectral licensing from the Federal Communications Commission.

3.2.3 Limited Geometry

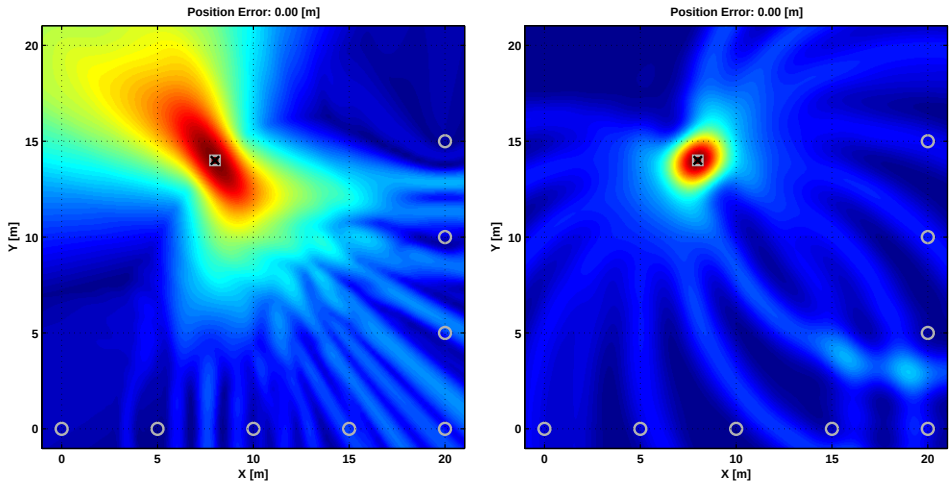

(a) σART (b) TART

Figure 3.5: σART vs. TART - 8 Receiver Simulation

Next we will consider the effect of limited receiver geometry. In a system deployed by first responders, it will likely not be feasible to have receive antennas fully surrounding a building. The next simulation presented shows the performance of σART and TART with receive antennas on only two sides of the scan region and no reflections.

We observe that the σART metric image seems to have a high degree of ambiguity in one direction, while the TART metric image has a peak which is much more localized. In this ideal simulation both methods have no error. However, previous work with σART has indicated that in

the presence of noise and multipath this type of ambiguity in the metric images often coincides with large errors in the direction of ambiguity. This will also be shown directly in Chapter 5. This suggests that TART will perform better in a limited geometry situation such as this one.

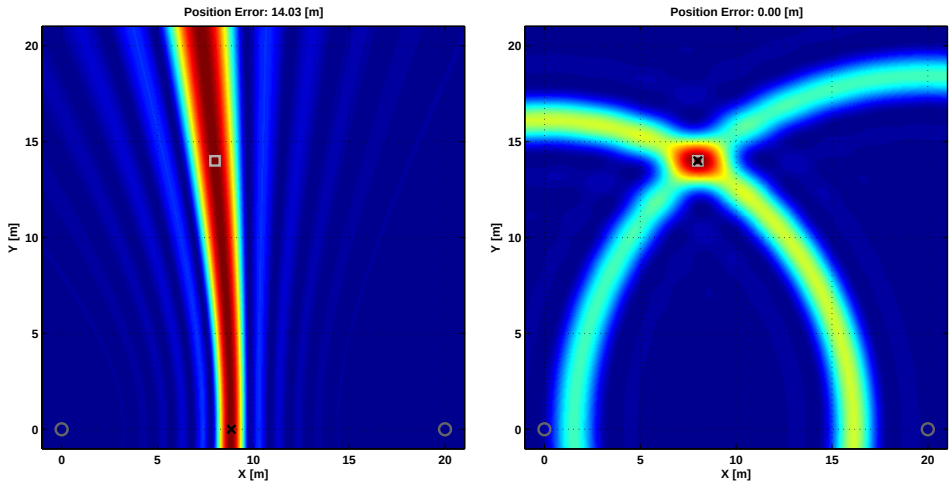

(a) σART (b) TART

Figure 3.6: σART vs. TART - 2 Receiver Simulation

A similar case is shown in Figure 3.6 in which only 2 receive antennas are used. This example clearly illustrates the fundamental difference between σART and TART. Like a classic TOA triangulation system, we observe how the TART metric image consists of intersecting circles. In contrast, σART is like a TDOA system, depending on only relative range information and is underdetermined in this case. The transmitter could be at any location along a hyperbola that is the locus of identical time delay differences between the received signals.

3.2.4 Three-Dimensional Scanning

While much can be learned from two-dimensional σART /TART scans as presented previously, our requirement is to estimate position in three-dimensions. We will now observe the behavior of a full three-dimensional scan in the ideal case shown in Figure 3.1. A three-dimensional scan results in a metric volume as opposed to an image, which we can depict using slices through the volume, as shown in Figure 3.7. We observe the horizontal slice through our metric volume matches the metric images in Figure 3.1.

The vertical slice for TART reveals the intersecting spheres summed to create a maximum at the

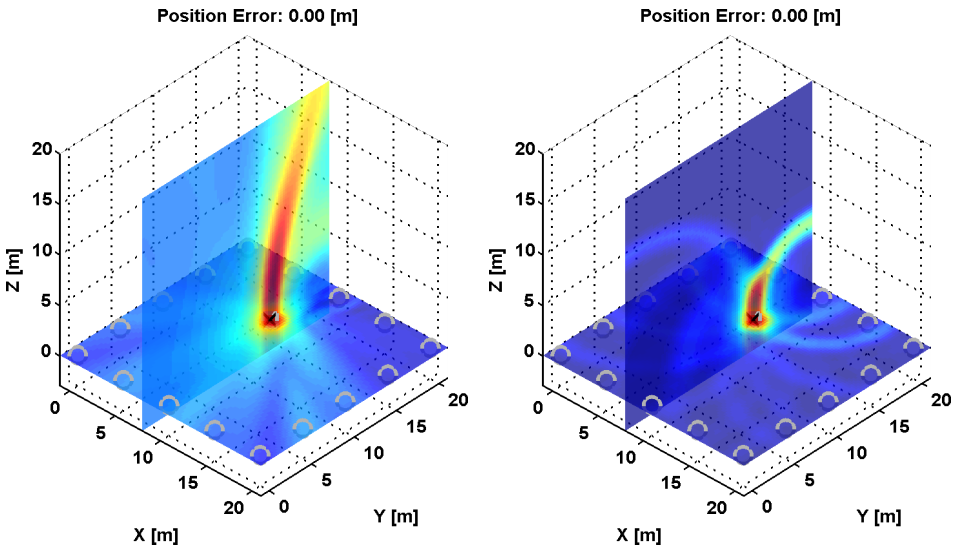

(a) σART (b) TART

Figure 3.7: σART vs. TART - Three-Dimensional Simulation

true location. We see that the TART metric forms a tighter peak in the horizontal plane than it does in the vertical plane. This is an effect of the geometry in use which has the transmitter and receivers in one plane, thus the intersecting spheres are nearly parallel to each other at the transmitter location, increasing solution ambiguity.

The vertical slice for σART reveals far more ambiguity in the vertical dimension than TART however. The relative distance information used by σART results in large vertical ambiguity when the receive antennas are co-planar, or even close to co-planar. Results with real data over the past several years using σART in our system have shown that this ambiguity directly results in large vertical position errors.

The next simulation presented is identical to the previous one but with the location of the transmit antenna being raised out of the plane of the receive antennas, shown in Figure 3.8. We again observe similar ambiguity of σART metric peak in the vertical dimension, while the TART metric peak is now more symmetrical, as the intersecting spheres are no longer all parallel.

Finally we will show an example that reflects a more general situation likely to be found in practice. This example again uses only 8 reference antennas on two sides of the scan region. In this example height diversity has been added to the reference antennas so that they are not all coplanar. Alternating antennas have been raised to a height of 2 meters. The mobile antenna has been

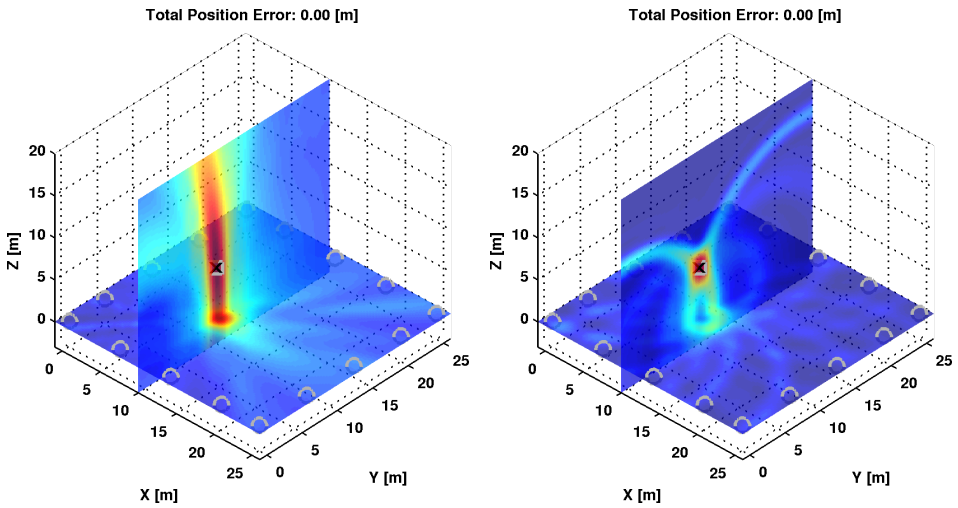

(a) σART (b) TART

Figure 3.8: σART vs. TART - Three-Dimensional Simulation with Raised Transmitter

elevated to a height of 3 meters, so it is above the region encompassed by the reference antennas. Although the reference antennas are no longer coplanar, they still have much more spatial diversity in the horizontal dimensions, which results in σART still having significant ambiguity in the vertical dimension. TART however has a significantly more localized metric peak both vertically and horizontally. It is important to note however that it is not symmetrical, it is considerably elongated in the vertical dimension; system geometry certainly does have an effect on the shape of the TART peak.

3.2.5 Computation Time

Another important comparison between σART and TART is computation time. The algorithms are identical in many respects. The pre-processing steps (described in Section 2.2.3) are the same, as well as the rephasing. The sole difference is the evaluation of the metric at each scan location.

σART requires the computation of the first singular value of $\mathbf{R}'$. The current implementation of the PPL system uses MATLAB for processing received signals at the base station PC. The fastest known method of computing uses the relationship

$$\sigma_1(\mathbf{A}) = \sqrt{\lambda_1(\mathbf{A}^H\mathbf{A})}, [24] \tag{3.8}$$

where $\sigma_1(\mathbf{A})$ is the largest singular value of a matrix $\mathbf{A}$ and $\lambda_1(\mathbf{A}^H\mathbf{A})$ is the largest eigenvalue of

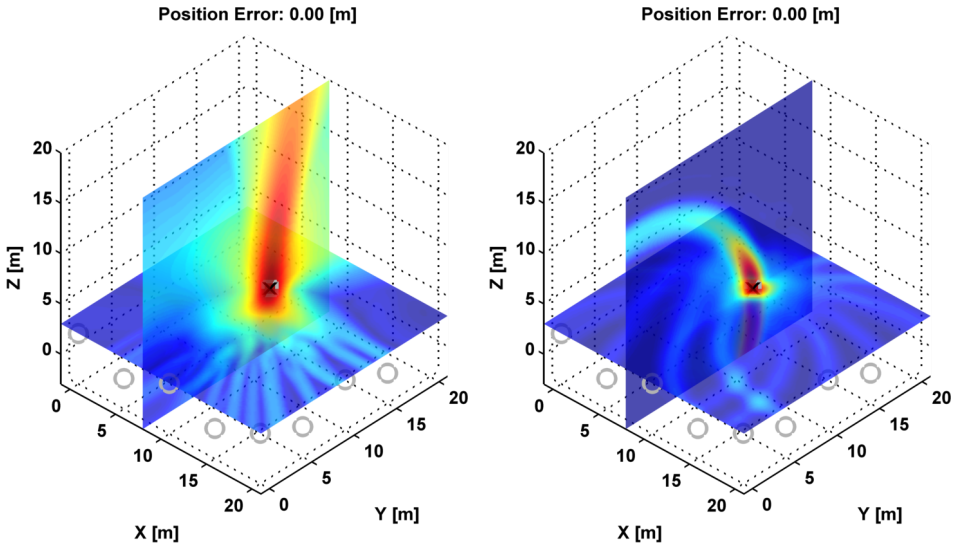

(a) σART (b) TART

Figure 3.9: σART vs. TART - Three-Dimensional Simulation with Practical Geometry

$\mathbf{A}^H\mathbf{A}$. This is implemented in MATLAB as:

```
sigma2 = eig(R_prime'*R_prime);
sART_metric = sqrt(sigma2(end));
```

To determine a typical computation time for a metric evaluation, this was performed on a complex matrix $\mathbf{R}' \in \mathbb{C}^{16\times100}$, representing the typical case of 16 receive antennas and 100 carriers. This was performed on the current PPL base station PC, with dual quad-core Intel Xeon CPUs clocked at 2.33 GHz and 4 GB of RAM. The metric was evaluated 100,000 times with an average computation time of 104.7 μs.

Alternatively, the TART metric is $\text{elm}(\mathbf{1}_{1\times M}\mathbf{R}')\mathbf{1}_{P\times1}$. This is implemented in MATLAB as:

```
TART_metric = sum(abs(sum(R_prime,1)).^2);
```

This metric was tested under the same condition and showed to have an average computation time of 8.5 μs per metric evaluation, more than 10 times faster than the σART metric.

Of course, when scanning a large solution space, each position estimate is the result of a large number of metric evaluation. Most of the computation time for each position estimate is used during the metric evaluation and the rephasing multiplication at each scan location. For this reason

the promise of faster computation time is another potential advantage of using TART rather than σART.

3.3 Transactional Synchronization

The simulated results presented in Section 3.2 suggest various improvements to the performance of the PPL system by replacing the current σART algorithm with the TART algorithm. However, with the architecture of the current system our received signals are subject to a random time-offset $\tilde{\tau}$, which is not in compliance with the requirements of the TART algorithm. In this section an alternative system architecture is proposed, along with a synchronization scheme to support it, in which the received signal data is suitable for TART, meeting the requirement that $\tilde{\tau} = 0$.

The current system architecture involves a unidirectional ranging signal, transmitted from the personnel within the building to the receiver stations outside the building. The alternative system architecture being proposed involves bidirectional signals. The mobile units to be tracked inside the building would be transceivers, capable of both transmitting and receiving a multicarrier ranging signal. Similarly the stationary reference units outside the building (mounted on firetrucks, deployable ladder systems, etc.) would also be transceivers. A signaling transaction would occur, in which a signal is transmitted by each reference unit and captured by the mobile unit, and also a signal transmitted by the mobile unit is captured by each reference unit.

3.3.1 Transactional Synchronization Concept

A simplified version of this transactional scheme is illustrated in Figure 3.10. Consider momentarily that the transmitted signal is simply an impulse in the time domain, $x(t) = \delta(t)$. The ideal received signal received after the signal travels through a multipath channel is the impulse response of the channel $h(t)$. This input/output relationship is illustrated by an example in the top portion of Fig. 3.10. We see the impulse response consists of several summed versions of the input signal, with various attenuations and delays, which is consistent with our multipath channel model.

Now consider a two unsynchronized transceivers, a mobile transceiver q and a reference transceiver p. At the time of a transaction, the two units will have a random time-offset between $\tilde{\tau}_p$. Thus the symbol windows will not line up in time, but be shifted from one another by $\tilde{\tau}_p$ as shown in Fig 3.10.

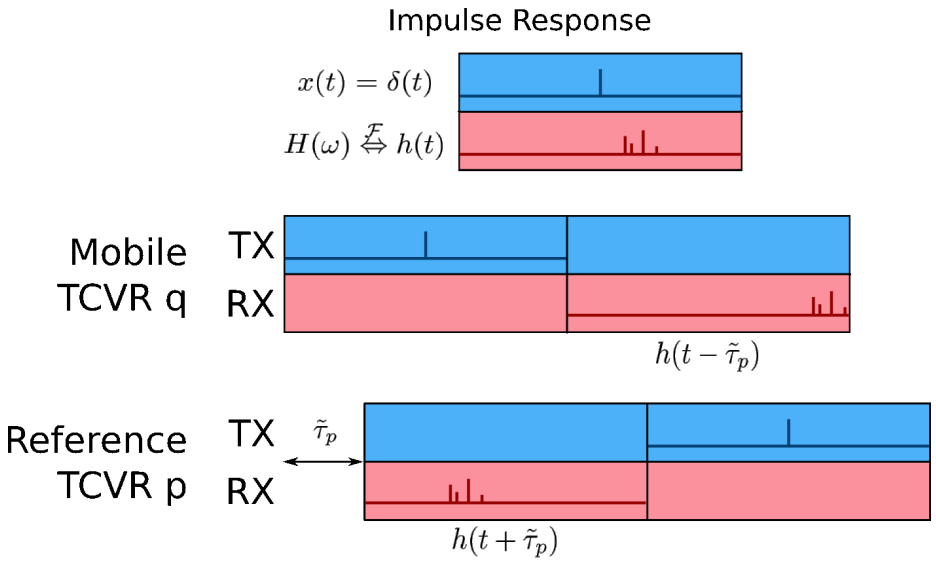

Figure 3.10: Transactional Synchronization

If the mobile transceiver transmits the signal $x(t)$, the reference transceiver would receive $h(t - \tilde{\tau}_p)$. This complies with our notion of received signals having a random time-offset. Shortly after this initial signal capture however, a second capture takes place where the reference transceiver transmits and the mobile transceiver receives. This received signal will be $h(t + \tilde{\tau})$, the same as the first received signal but in with a shift of $\tilde{\tau}_p$ in the opposite direction. This assumes that the radio channel response obeys Lorentz Reciprocity.[6] It will be shown that knowledge of $h(t - \tilde{\tau}_p)$ and $h(t + \tilde{\tau}_p)$ allows solving for the unknown random time-offset $\tilde{\tau}_p$.

3.3.2 Time-offset Ambiguity

Next we will consider a transaction with our multicarrier signal and non-ideal synchronization model. The received signals in the frequency domain would be:

$$\mathbf{r}_q = \mathbf{x} \circ \mathbf{h}_{q,p} \circ e^{-j(\boldsymbol{\omega}\tilde{\tau}_p + \tilde{\theta}_q)}, \tag{3.9}$$

$$\mathbf{r}_p = \mathbf{x} \circ \mathbf{h}_{q,p} \circ e^{-j(-\boldsymbol{\omega}\tilde{\tau}_p + \tilde{\theta}_p)}. \tag{3.10}$$

Where $\mathbf{r}_q$ and $\mathbf{r}_p$ are the signals received by the mobile transceiver q and reference transceiver p respectively, $\mathbf{x}$ is the transmitted signal and $\mathbf{h}_{q,p}$ is the reciprocal channel response between the two units. We see that each received signal has the same random time-offset in the opposite direction.

If we entrywise divide the received signals, the transmitted signal and channel response terms cancel:

$$\frac{[\mathbf{r}_p]}{[\mathbf{r}_q]} = e^{j(\boldsymbol{\omega} 2\tilde{\tau}_p - \tilde{\theta}_p + \tilde{\theta}_q)}. \tag{3.11}$$

The result is a complex sinusoid with a periodicity that corresponds to $2\tilde{\tau}_p$. We can estimate the periodicity of this complex sinusoid using the Direct State Space pole solver [2, 34], a frequency estimation technique using the Singular Value Decomposition. This technique ignores frequency independent phase terms, this the random frequency independent phase terms $-\tilde{\theta}_p + \tilde{\theta}_q$ are acceptable. The resultant "pole" is:

$$\text{pole}\frac{[\mathbf{r}_p]}{[\mathbf{r}_q]} = e^{j(2\Delta\omega\tilde{\tau}_p)}. \tag{3.12}$$

Taking the angle of the complex pole:

$$\angle\text{pole}\frac{[\mathbf{r}_p]}{[\mathbf{r}_q]} = 2\Delta\omega\tilde{\tau}_p + 2\pi a, \tag{3.13}$$

where a is an integer. Solving for $\tilde{\tau}_p$,

$$\frac{\angle\text{pole}\frac{[\mathbf{r}_p]}{[\mathbf{r}_q]}}{2\Delta\omega} = \tilde{\tau}_p + \frac{2\pi a}{2\Delta\omega}, \tag{3.14}$$

$$\tilde{\tau}_p = \frac{\angle\text{pole}\frac{[\mathbf{r}_p]}{[\mathbf{r}_q]}}{2\Delta\omega} - \frac{\pi a}{\Delta\omega}, \tag{3.15}$$

$$\frac{\pi a}{\Delta\omega} = \frac{\pi a}{2\pi\Delta f} = \frac{a}{2\Delta f} = \frac{aT}{2}, \tag{3.16}$$

$$\tilde{\tau}_p = \frac{\angle\text{pole}\frac{[\mathbf{r}_p]}{[\mathbf{r}_q]}}{2\Delta\omega} - \frac{aT}{2}. \tag{3.17}$$

Where T is the period of our multicarrier signal. We observe that solving for $\tilde{\tau}_p$ yields infinite solutions, one for each integer value of a.

Since our multicarrier signal is periodic any transmitted or received signal is unaffected by a time shift that is an integer number of periods.

$$r(t) = r(t + aT) \tag{3.18}$$

$$\mathbf{r} = \mathbf{r} \circ e^{j\boldsymbol{\omega} aT} \tag{3.19}$$

For this reason we need only consider solutions for $\tilde{\tau}_p$ in the interval $[0, T)$. This results in two possible solutions,

$$\tilde{\tau}_p = \frac{\angle\text{pole}\frac{[\mathbf{r}_p]}{[\mathbf{r}_q]}}{2\Delta\omega} \quad \text{or} \quad \tilde{\tau}_p = \frac{\angle\text{pole}\frac{[\mathbf{r}_p]}{[\mathbf{r}_q]}}{2\Delta\omega} + \frac{T}{2}. \tag{3.20}$$

Unfortunately there is no information to distinguish which of these solutions is correct, and choosing incorrectly would result in a large timing error ($T/2$ is determined in practice by our choice of $\Delta\omega$ to be hundreds of meters).

3.3.3 Time-offset Ambiguity Resolution

We have observed that it is possible to use a transactional approach to measure the random time-offset between two transceiver units $\tilde{\tau}_p \pmod{T/2}$, when using a multicarrier signal with period T. In order to have our estimate of this random time-offset be usable to rectify received signals we would need $\tilde{\tau}_p \pmod{T}$ however.

While this issue was initially troubling, a relatively simple solution was discovered. Suppose we have a multicarrier signal with twice as many carriers and half of the carrier spacing,

$$\ddot{x}(t) = \sum_{m=0}^{2M-1} e^{-j(t(\omega_0 + m\frac{\Delta\omega}{2}) + \theta_m)}. \tag{3.21}$$

The period of this multicarrier signal would be $2T = \frac{2}{2\pi\Delta\omega}$. Therefore, if this signal was used with the proposed transactional synchronization scheme, the random time-offset could be estimated $\tilde{\tau}_p \pmod{T}$, as desired for the original multicarrier signal.

$$\tilde{\tau}_p = \frac{\angle\text{pole}\frac{[\ddot{\mathbf{r}}_p]}{[\ddot{\mathbf{r}}_q]}}{2\Delta\omega} \tag{3.22}$$

Where $\ddot{\mathbf{r}}_p$ and $\ddot{\mathbf{r}}_p$ denote received signal vectors at transceivers p and q respectively, when the transmitted signal is $\ddot{x}(t)$.

Observe also that the carrier frequencies of the original signal $x(t)$ are a subset of the frequencies of $\ddot{x}(t)$. This means that a received signal vector $\mathbf{r}$ can be constructed as a subset of $\ddot{\mathbf{r}}$:

$$\mathbf{r} = \left[(\ddot{\mathbf{r}})_1\ (\ddot{\mathbf{r}})_3\ (\ddot{\mathbf{r}})_5 \ldots (\ddot{\mathbf{r}})_{2M}\right]^T \tag{3.23}$$

This relationship allows us to use $\ddot{x}(t)$ for the purpose of solving for the random time-offset, and reverting to $x(t)$ for subsequent processing.

3.3.4 Received Signal Rectification

Recall the received signal from the reference transceiver p:

$$\mathbf{r}_p = \mathbf{x} \circ \mathbf{h}_{q,p} \circ e^{-j(-\boldsymbol{\omega}\tilde{\tau}_p + \tilde{\theta}_p)}. \tag{3.24}$$

We can use the known transmitted signal $\mathbf{x}$ and our estimate of $\tilde{\tau}_p$ to rectify the captured signal $\mathbf{r}_p$ to form $\mathbf{s}_p$,

$$\mathbf{s}_p = \mathbf{r}_p \circ \frac{1}{\mathbf{x}} \circ e^{-j\boldsymbol{\omega}\tilde{\tau}_p}, \tag{3.25}$$

$$\mathbf{s}_p = \frac{[\mathbf{x}]}{[\mathbf{x}]} \circ \mathbf{h}_{1,p} \circ e^{-j(-\boldsymbol{\omega}\tilde{\tau}_p + \tilde{\theta}_p)} \circ e^{-j\boldsymbol{\omega}\tilde{\tau}_p}, \tag{3.26}$$

$$\mathbf{s}_p = \mathbf{h}_{1,p} \circ e^{-j\tilde{\theta}_p}. \tag{3.27}$$

This new rectified signal $\mathbf{s}_q$ now satisfies the TART assumption of having no random time-offset, and may be used as the column p of the received data matrix $\mathbf{R}$.

3.3.5 Alternative Scheme

In this section an alternative scheme for transactional synchronization is proposed, which has the benefit of not requiring the signal received by the mobile unit to be sent to the base station via a data communications channel. Suppose the previously described signal transaction takes place, such that the received signal at the mobile transceiver q and the reference antenna p are,

$$\mathbf{r}_q = \mathbf{x} \circ \mathbf{h}_{q,p} \circ e^{-j(\boldsymbol{\omega}\tilde{\tau}_p + \tilde{\theta}_q)}, \text{ and} \tag{3.28}$$

$$\mathbf{r}_p = \mathbf{x} \circ \mathbf{h}_{q,p} \circ e^{-j(-\boldsymbol{\omega}\tilde{\tau}_p + \tilde{\theta}_p)} \tag{3.29}$$

respectively.

Now suppose that the mobile unit processes its received signal to generate a new transmit waveform, $\mathbf{x}^{\leftarrow}$. To do this it inverts each value of the received signal vector.

$$\mathbf{x}^{\leftarrow} = \frac{[\mathbf{1}]}{[\mathbf{r}_q]} = \frac{[\mathbf{1}]}{[\mathbf{x} \circ \mathbf{h}_{q,p}]} \circ e^{j(\boldsymbol{\omega}\tilde{\tau}_p + \tilde{\theta}_q)} \tag{3.30}$$

This signal is then transmitted by the mobile unit. The reference unit receives a second signal,

$$\begin{aligned}\mathbf{r}_p^{\leftarrow} &= \mathbf{x}^{\leftarrow} \circ \mathbf{h}_{q,p} \circ e^{-j(-\omega\tilde{\tau}_p+\tilde{\theta}_p)} \\ &= \frac{[\mathbf{1}]}{[\mathbf{x} \circ \mathbf{h}_{q,p}]} \circ e^{j(\omega\tilde{\tau}_p+\tilde{\theta}_q)} \circ \mathbf{h}_{q,p} \circ e^{-j(-\omega\tilde{\tau}_p+\tilde{\theta}_p)} \qquad (3.31)\end{aligned}$$

$$\begin{aligned}\mathbf{r}_p^{\leftarrow} \circ \mathbf{x} &= \frac{[\mathbf{1}]}{[\mathbf{x}]} \circ e^{j(2\omega\tilde{\tau}_p-\tilde{\theta}_p+\tilde{\theta}_q)} \mathbf{r}_p^{\leftarrow} \circ \mathbf{x} \\ &= e^{j(2\omega\tilde{\tau}_p-\tilde{\theta}_p+\tilde{\theta}_q)} \qquad (3.32)\end{aligned}$$

We see that the second signal received by the reference transmitter can be multiplied by the known original signal $\mathbf{x}$ to produce a complex exponential whose periodicity is proportional to $2\tilde{\tau_p}$, identical to what is obtained in Equation 3.11. We can therefore estimate $\tilde{\tau_p}$ in the same manner described in Section 3.3.3 and use it to rectify the first signal received by the reference transceiver, without the need for the signal received by the mobile transceiver to be sent to the base station via a data link.

Additional computation on the mobile unit would be required to support this approach. The received time domain samples would need to be converted to the frequency domain via the FFT, then the non-carrier frequencies would be set to zero and the values at the carrier frequencies would be inverted. The signal would be converted back to the time domain with an inverse FFT and the resulting time domain waveform would then be scaled so it could be transmitted using the full dynamic range of the DAC.

Removing the need for the mobile transceiver unit to transmit data to the base station would be desirable in a deployable system, as it would require a considerable amount of data bandwidth. For example, a mobile transceiver sending received signals from 16 reference transceivers consisting of 32-bit complex numbers for 150 carriers at a rate of once per second would require 76.8 kbps of data throughput. This an undesirable prospect as it requires costly high speed wireless communication hardware on each mobile unit. Maintaining this data rate also becomes more difficult as the mobile unit travels further into the building and the received signal strength weakens. The alternative scheme described only requires data be sent from the reference units to the base station, where it is less of an issue to add wireless communication hardware and the communication signal strengths should remain constant.

The development of this alternative transactional synchronization scheme occurred late in the writing of this thesis, so all experimental results to be presented in Chapter 6 used the original

synchronization scheme. For remainder of this dissertation it will be implied that the original transactional synchronization is in use, unless specified otherwise.

Chapter 4

Hardware Considerations for TART

There are yet further issues that must be considered in order to implement the proposed transactional synchronization scheme with the PPL system hardware. Figure 4.1 shows the proposed system architecture which uses bidirectional ranging signals. In contrast to Figure 2.4, Figure 4.1

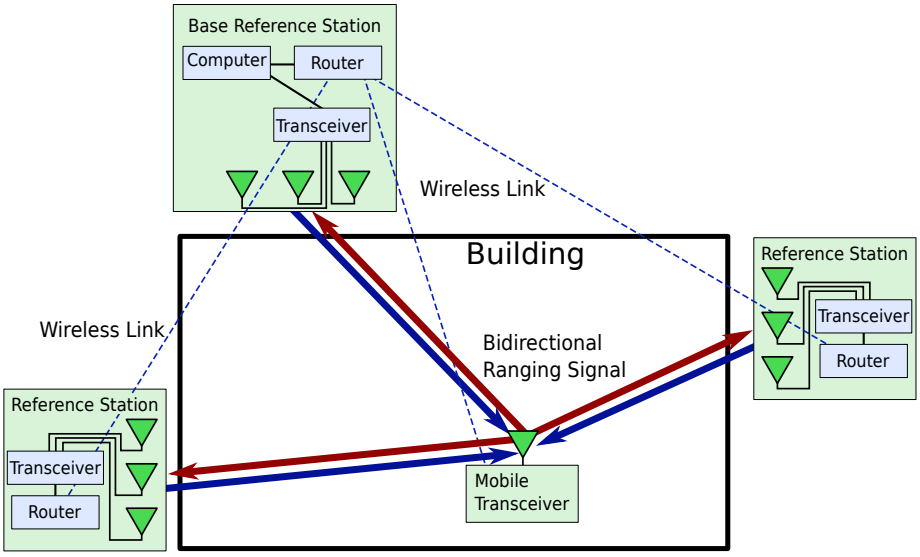

Figure 4.1: Transactional PPL System Architecture

illustrates the bidirectional signal used in the transactional approach, and the use of transceivers instead of a transmitter and receivers. Also depicted is the addition of a wireless data link to convey received signals from a mobile transceiver to the base station to be processed. The data link between the mobile unit and the base station may be removed by using the alternative transactional

synchronization scheme described in Section 3.3.5.

We have shown that a transaction between two unsynchronized transceivers can produce a rectified received signal with no random time-offset, suitable for TART processing. TART of course uses data from several reference antennas outside of the building, attached to different transceivers, so several transactions would need to be performed in succession in order to obtain all of the signal data to perform TART. These transactions would need to be completed fast enough so that the channel response can be approximated to be constant. Also, it is important that the transactions be fast enough so that $\tilde{\tau}(t)$ can be assumed to be constant as well. This will be discussed further in Section 4.4.

4.1 Transceiver Units

The WPI PPL research team has recently a developed a custom, 4-channel transceiver unit intended for use at the reference stations outside of the building. A picture of one of these units is shown in Figure 4.2. Even when using σART with the existing PPL system, it is important that

Figure 4.2: PPL Transceiver

the reference stations have the ability to transmit as well as receive in order to perform Geomet-

ric Autoconfiguration (GAC), as well as synchronizing the units for σART. It is for these reasons the transceiver units were developed, however they have also proven useful to test the concept of transactional synchronization with TART.

These units have four parallel receive channels with independent receive circuitry and ADCs. This means that samples can be captured from four different antennas simultaneously. There is a single transmitter circuit, the output of which is passed through a switch that selects a particular antenna, so the unit can transmit out of any one antenna at a time. A Field Programmable Gate Array (FPGA) controls the functionality of the unit and organizes received ADC data to be transmitted out of an ethernet port through a wireless data link to the base station. The transceiver circuit boards also provide the ability to access both input and output baseband signals, a feature intended for debugging.

The base station PC communicates with each transceiver using the custom PPL Control And Messaging Protocol (CAMP). This protocol allows the PC to send the transceiver various commands including commands that indicate when to capture data, when to transmit, and even send to arbitrary transmit waveforms.

4.2 Intra-unit Synchronization

A significant assumption that was tacitly made when describing the transactional synchronization was that the transmit and receive symbol windows were synchronized on a given transceiver. In Figure 3.10 for example, the illustration depicts the transmit and receive symbol windows in perfect alignment.

Unfortunately this is not the case with our existing transceiver units, as it was not a requirement of the design. Measurement on an oscilloscope showed the transmit and receive symbol windows to be misaligned by several hundred nanoseconds, and worse yet the time-offset varied when the transceiver circuit was powered on and off. Left unchecked, this time-offset between the transmit and receive symbol windows within a transceiver unit would destroy the very timing information that transactional synchronization aims to obtain.

Fortunately a way to circumvent this problem was found. Since the transceiver circuits were designed with the baseband inputs and outputs accessible, it is possible to connect the transmitted

baseband signal to the baseband input on one of the receive paths. Thus we can effectively connect the transmitter DAC directly to one of our receiver ADCs in a loopback capture. By analyzing the received symbols from that ADC, we can observe the timing relationship between the two.

Since we are only concerned with the transmit and receive symbol windows having no time-offset relative to each other, we can assume that the receive symbol window is "correct" and the transmitted signal is in error with a time-offset.

Recall the ideal transmitted signal is

$$X(\omega) = \sum_{m=0}^{M-1} \delta((\omega - (\omega_0 + m\Delta\omega))e^{j\theta_m}. \tag{4.1}$$

Alternatively this can be represented as a vector of carrier values,

$$\mathbf{x} = [e^{j\theta_0} \quad e^{j\theta_1} \quad \dots \quad e^{j\theta_m}]. \tag{4.2}$$

We will denote $\bar{\mathbf{x}}$ as the shifted transmit signal that we wish to rectify,

$$\bar{\mathbf{x}} = \mathbf{x} \circ e^{-j\boldsymbol{\omega}\widetilde{\mathcal{T}}}. \tag{4.3}$$

Where $\widetilde{\mathcal{T}}$ represents the random unknown time-offset between the ADC and the DAC on a particular transceiver. This is the signal we expect to receive at the ADC in this loopback mode.

If a received signal is captured, and entrywise divided by the ideal signal, then the result is a complex exponential whose periodicity corresponds to $\widetilde{\mathcal{T}}$.

$$\frac{[\bar{\mathbf{x}}]}{[\mathbf{x}]} = e^{-j\boldsymbol{\omega}\widetilde{\mathcal{T}}} \tag{4.4}$$

Figure 4.3 shows an example with real data captured from a PPL transceiver unit, displaying the magnitude and phase of $\frac{[\bar{\mathbf{x}}]}{[\mathbf{x}]}$. We observe a complex exponential as expected, characterized by a nearly constant magnitude and linear phase versus frequency. The magnitude variation of about 1.5 dB across frequency is expected and is due to the characteristics of using non-ideal baseband filters.

The value of $\widetilde{\mathcal{T}}$ can be estimated using the Direct State Space pole solver mentioned previously.

$$\text{pole}\frac{[\bar{\mathbf{x}}]}{[\mathbf{x}]} = e^{-j\Delta\omega\widetilde{\mathcal{T}}} \tag{4.5}$$

$$\widetilde{\mathcal{T}} = \frac{-\angle\text{pole}\frac{[\bar{\mathbf{x}}]}{[\mathbf{x}]}}{\Delta\omega} + aT \tag{4.6}$$

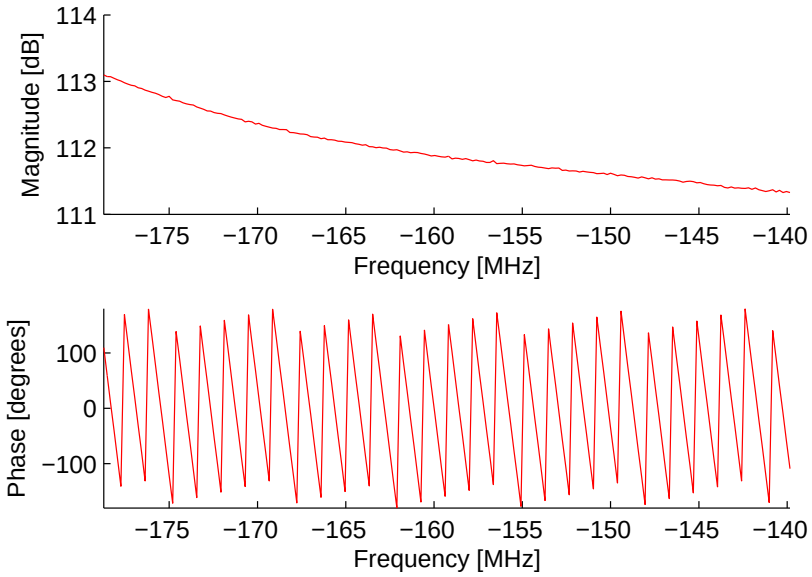

Figure 4.3: Intra-Unit Synchronization: Real data $\frac{[\bar{\mathbf{x}}]}{[\mathbf{x}]}$

In this case we can measure the time-offset $\widetilde{\mathcal{T}} \pmod{T}$, which is acceptable without any ambiguity problem like the transactional synchronization. For the real data shown in Figure 4.3 $\widetilde{\mathcal{T}}$ was estimated to be -710.27 ns.

Once $\widetilde{\mathcal{T}}$ has been solved for on each transceiver unit, the value may be used to regenerate the transmitted waveform such that the transmit symbol window matches the receive symbol window. If the signal $\mathbf{x} \circ e^{j\omega\widetilde{\mathcal{T}}}$ is generated and used as the digital waveform to be transmitted, then the transmit and receive windows will be aligned.

Since our transceiver units have the ability to reset the transmit waveform at any time, we can set the appropriate waveform each time the unit is powered on, after the intra-unit synchronization procedure runs and $\widetilde{\mathcal{T}}$ is estimated.

4.3 Frequency Response Calibration

Another significant consideration that must be made before using TART in a real system, is the frequency responses of non-ideal hardware. In a real system transmitter and receiver circuitry, cables and antennas can have significant effect on received signals.

Figure 4.4 depicts the various stages the signal must undergo before being received. Let us

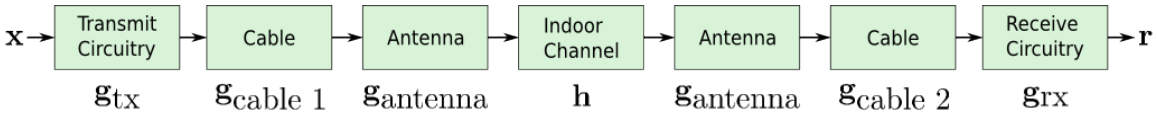

Figure 4.4: Frequency Response Diagram

consider the original signal as the complex vector $\mathbf{x}$. At the output of the DAC, we assume the desired signal is produced. Next the signal must propagate through various filters, amplifiers and a mixer before the RF signal is output from the transmitter/transceiver. The transmitter circuitry is certainly not linear; the input is a baseband signal and the output is an RF signal. Nonetheless there is a one-to-one correspondence between carriers at the input and output, and a theoretically known relationship of the magnitude and phase of these carriers. Thus we can use the notion of a transfer function commonly used for a linear system. For a classic linear system, the transfer function $G(\omega)$ is defined as

$$G(\omega) = \frac{B(\omega)}{A(\omega)}, \tag{4.7}$$

where $A(\omega)$ is the input to the system represented in the frequency domain, and $B(\omega)$ is the resultant output. For our transmitter circuitry we have a similar relation,

$$G(\omega) = \frac{Y(\omega)}{X(\omega - f_c)}, \tag{4.8}$$

$$\mathbf{g}_{\text{tx}} = \frac{[Y(\boldsymbol{\omega})]}{[X(\boldsymbol{\omega} - f_c)]} = \frac{[\mathbf{y}]}{[\mathbf{x}]}, \tag{4.9}$$

where Y is the output of the transmitter circuitry. The vector $\mathbf{g}_{\text{tx}}$ behaves like a transfer function in that it characterizes the relationship between the input and the output of the system.

After the RF signal is transmitted from the transmitter/transceiver, it must travel over a cable which connects to the transmit antenna. Currently we use coaxial cables that are approximately 15 meters long. These cables have a significant effect on the signal. They add significant delay and attenuation, and these effects vary from cable to cable since they can not be manufactured identically. These cables can be modeled by a classic transfer function, or a transfer vector of values at our carrier frequencies. We will denote the transfer vector for the cable from the transmitter to the transmit antenna as $\mathbf{g}_{\text{cable 1}}$.

The cable connects to an antenna which radiates the signal into the radio channel. The antenna itself however may have significant effects on the signal, which can be represented as a transfer

vector $\mathbf{g}_{\text{antenna}}$.

The signal then propagates through the indoor RF channel, which has the transfer vector $\mathbf{h}$. This is, of course, what we're ultimately interested in measuring because it contains information about the relative position of the transmit and receive antenna.

Next the signal propagates through a receive antenna and cable with transfer vectors $\mathbf{g}_{\text{antenna}}$ and $\mathbf{g}_{\text{cable 2}}$ respectively. Next the signal propagates through receiver circuitry before being sampled, which affects the signal similarly to the transmit circuitry, with transfer vector $\mathbf{g}_{\text{rx}}$.

The received signal $\mathbf{r}$ is the aggregate of these effects, along with the non-ideal synchronization term,

$$\mathbf{r} = \mathbf{x} \circ \mathbf{g}_{\text{tx}} \circ \mathbf{g}_{\text{cable 1}} \circ \mathbf{g}_{\text{antenna}} \circ \mathbf{h} \circ \mathbf{g}_{\text{antenna}} \circ \mathbf{g}_{\text{cable 2}} \circ \mathbf{g}_{\text{rx}} \circ e^{-j(\omega\tilde{\tau}+\tilde{\theta})} \tag{4.10}$$

Our goal is to determine $\mathbf{h}$ from our received signal, which is obscured by the other various effects present in the system. Unlike the synchronization problems discussed, the transfer vectors are not time-varying so they could potentially be removed with a one-time calibration. The following sections will discuss the procedures developed to estimate the necessary frequency response parameters in order to calibrate out hardware effects to estimate $\mathbf{h}$.

To estimate the calibration parameters of a particular cable a laboratory procedure was developed, depicted in Figure 4.5. Two transceiver units were used, however one was solely used as a

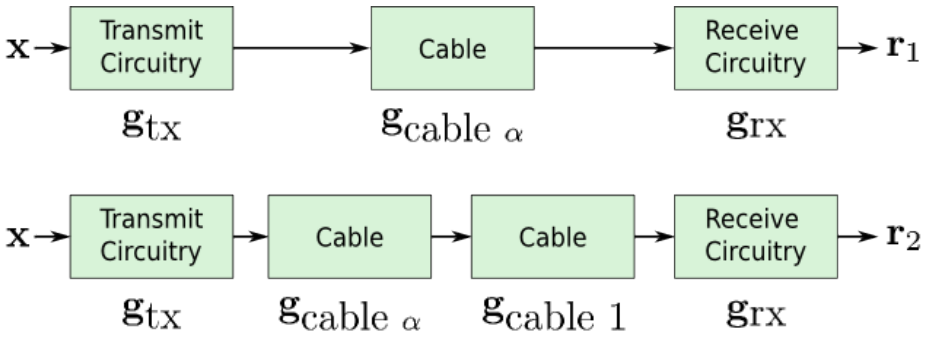

Figure 4.5: Cable Calibration Procedure

transmitter while the other was used solely as a receiver. The two units were driven with a common external oscillator, eliminating relative sample clock drift such that the time-offset between transmitted and received symbols $\tilde{\tau}$ was constant. The two units were connected by a short cable α, which is not the cable we are interested in calibrating, but has its own frequency response vector

$\mathbf{g}_{\text{cable }\alpha}$. This configuration results in a received signal:

$$\mathbf{r}_1 = \mathbf{x} \circ \mathbf{g}_{\text{tx}} \circ \mathbf{g}_{\text{cable }\alpha} \circ \mathbf{g}_{\text{rx}} \circ e^{-j(\boldsymbol{\omega}\tilde{\tau}+\tilde{\theta}_1)}. \tag{4.11}$$

Next the cable to be calibrated, Cable 1 for example, is inserted in series with Cable x. This configuration results in a received signal:

$$\mathbf{r}_2 = \mathbf{x} \circ \mathbf{g}_{\text{tx}} \circ \mathbf{g}_{\text{cable }\alpha} \circ \mathbf{g}_{\text{cable }1} \circ \mathbf{g}_{\text{rx}} \circ e^{-j(\boldsymbol{\omega}\tilde{\tau}+\tilde{\theta}_2)}. \tag{4.12}$$

Note that we have assumed that the frequency independent phase offset term $\tilde{\theta}$ may be different between the two captures, but $\tilde{\tau}$ must be constant.

If the two received signal vectors are entrywise divided, we obtain

$$\frac{[\mathbf{r}_2]}{[\mathbf{r}_1]} = \mathbf{g}_{\text{cable }1} \circ e^{-j(\tilde{\theta}_2-\tilde{\theta}_1)}, \tag{4.13}$$

which is the frequency response of the cable with an random frequency independent phase offset. Since TART was designed to ignore frequency independent phase offsets on received signals, it is sufficient that we have estimated $\mathbf{g}_{\text{cable }1}$ with that additional degree of freedom. We will define

$$\mathbf{c}_{\text{cable }1} = \frac{[\mathbf{r}_1]}{[\mathbf{r}_2]} = \frac{1}{\mathbf{g}_{\text{cable }1}} \circ e^{j\tilde{\theta}}, \tag{4.14}$$

the "calibration vector" which inverts the frequency response of the cable.

In order to calibrate for the effects of transmit and receive circuitry, a similar procedure was developed. This procedure involves two transceivers that are connected by a cable with a known frequency response. A transactional capture takes place, producing received signals $\mathbf{r}_1$ and $\mathbf{r}_2$, as depicted in Figure 4.6. Using the method described in Section 3.3, the random time-offset $\tilde{\tau}$ can be determined. The only difference when using the method here is that the reciprocal channel response represents the aggregate of the cascaded frequency response vectors, instead of just the radio channel.

The estimate of the random time-offset between the units $\tilde{\tau}$ is then used to create a rectified signal:

$$\mathbf{s} = \mathbf{x} \circ \mathbf{g}_{\text{tx}} \circ \mathbf{g}_{\text{cable }1} \circ \mathbf{g}_{\text{rx}} \circ e^{-j(\boldsymbol{\omega}\tilde{\theta})}. \tag{4.15}$$

Dividing by the known transmitted signal and frequency response of the cable we obtain,

$$\frac{[\mathbf{s}]}{[\mathbf{x} \circ \mathbf{g}_{\text{cable }1}]} = \mathbf{g}_{\text{tx}} \circ \mathbf{g}_{\text{rx}} \circ e^{-j(\boldsymbol{\omega}\tilde{\theta})}. \tag{4.16}$$

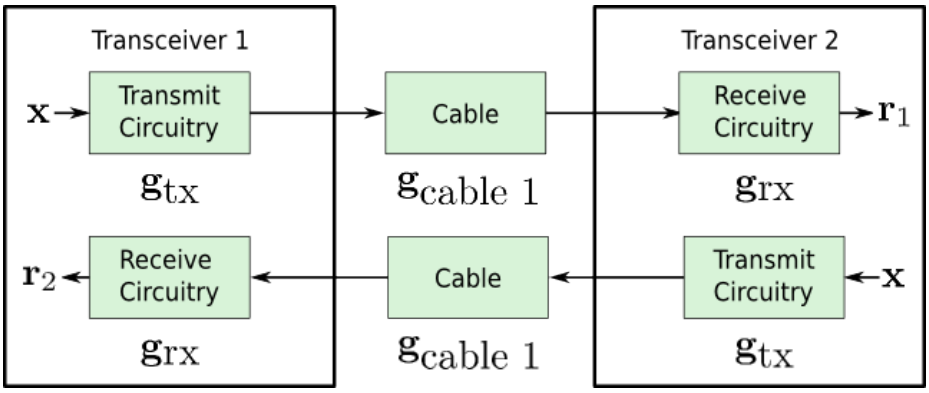

Figure 4.6: Transceiver Calibration Procedure

This can then be inverted to obtain the calibration vector which undoes the effects of the transmitter and receiver circuitry of the transceivers.

$$\mathbf{c}_{\text{tx,rx}} = \frac{[\mathbf{x} \circ \mathbf{g}_{\text{cable 1}}]}{[\mathbf{s}]} = \frac{1}{\mathbf{g}_{\text{tx}} \circ \mathbf{g}_{\text{rx}}} \circ e^{j\omega\tilde{\theta}} \tag{4.17}$$

Again this calibration vector has an acceptable unknown random frequency independent phase offset.

The calibration vectors for the antennas are more difficult to obtain. Such measurements can be made in an anechoic chamber which allows the antennas to be measured using an accurately known channel. Alternatively, the frequency response of the antennas may be simulated using antenna modeling software. Neither of these approaches are readily implementable the author, so the frequency responses of the antennas have been approximated as time delays of approximately 0.75 ns.

$$\mathbf{c}_{\text{antenna}} = e^{-0.75 \cdot 10^{-9} j\omega} \tag{4.18}$$

This was value determined empirically from real signals captured in a line of sight configuration. It is suggested that further research be performed in the area of antenna calibration, particularly to compensate for phase changes as a function of antenna angle.

Now recall the received signal model from Equation 4.10. Applying our calibration vectors to the received signal we obtain

$$\mathbf{r} \circ \mathbf{c}_{\text{rx,tx}} \circ \mathbf{c}_{\text{cable 1}} \circ \mathbf{c}_{\text{antenna}} \circ \mathbf{c}_{\text{antenna}} \circ \mathbf{c}_{\text{cable 2}} \circ \frac{1}{\mathbf{x}} = \mathbf{h} \circ e^{-j(\omega\tilde{\tau}+\tilde{\theta})} \tag{4.19}$$

Thus after applying the calibration vectors, our received signal matches the model assumed by the transactional synchronization approach.

4.4 Clock Stability

Next we must address the issue that the time-offset between two transceivers driven by independent oscillators is time-varying, $\tilde{\tau}(t)$. Our transactional synchronization method however assumes that this time-offset is the same for the pair of received signals. The signals exchanged during a transaction can not be simultaneous, so there must be some difference $\tilde{\tau}(t_b) - \tilde{\tau}(t_a)$ between the time-offset on each received signal, where t_a and t_b are the times at which each signal in the transaction is captured.

If the difference $t_b - t_a$ is significantly large, then $\tilde{\tau}(t_b) - \tilde{\tau}(t_a)$ may be so large that this timing error will corrupt the rectified received signal after transactional synchronization. Thus in order for our approach to work $t_b - t_a$ must be small enough relative to the rate at which the transceiver clocks drift apart to ensure $\tilde{\tau}(t_b) \approx \tilde{\tau}(t_a)$. A trade-off exists between shortening the amount of time between the pair of signal captures and using a more accurate clock to extend the amount of time it takes for $\tilde{\tau}(t_b) - \tilde{\tau}(t_a)$ to become significant.

Let us reconsider the case described Section 2.3.1. Suppose we used the same crystal oscillator on the mobile transceiver unit and Rubidium atomic clock on the reference transceiver units. The worst case relative clock drift is approximately 2.5 ppm. Historically on this project we have used the value 0.5 ns as the allowable timing error threshold.[2] This corresponds to approximately 15 cm of ranging error. With a relative drift rate of 2.5 ppm, the difference between two clocks would reach the 0.5 ns threshold in 200 μs. Thus to directly perform the transactional synchronization approach with the current oscillators used by our system, the time between the exchanged signals should be less than 200 μs.

If this time is prohibitively small, there are measures that can be taken to increase it. First, a more accurate clock may be used on the mobile unit, such as an oven controlled crystal oscillator or Rubidium atomic clock. This generally comes at the cost of increased size, power consumption and price.

Additionally clock modeling may allow for better performance. If the relationship between

a pair of clocks is measured at times t_i and t_{i+1}, then the average of the instantaneous frequency difference between the two clocks over that interval is

$$\bar{y}_i^{\mathcal{T}} = \frac{\tilde{\tau}(t_{i+1}) - \tilde{\tau}(t_i)}{\mathcal{T}} \tag{4.20}$$

where $\mathcal{T} = t_{i+1} - t_i$ for all i. The Allan Variance is defined as

$$\sigma_y^2(\mathcal{T}) = \frac{1}{2} E\left\{\left(\bar{y}_{i+1}^{\mathcal{T}} - \bar{y}_i^{\mathcal{T}}\right)^2\right\} \tag{4.21}$$

where $E\{\cdot\}$ represents the expectation operator.[1] The Allan Variance is a measure of clock stability, and is often plotted as a function of size of the interval $\mathcal{T}$. The Allan Deviation is the square root of the Allan Variance, $\sigma_y(\mathcal{T}) = \sqrt{\sigma_y^2(\mathcal{T})}$.

This implies that if the clock drift function $\tilde{\tau}(t)$ was evaluated at times t_0, t_1 and t_2, then difference between the average frequencies over the two intervals, (t_0, t_1) and (t_1, t_2), would have variance $2\sigma_y^2(\mathcal{T})$ over set of many repeated trials. If $\tilde{\tau}(t_0)$ and $\tilde{\tau}(t_1)$ are known, they they may be used to estimate $\tilde{\tau}(t_2)$ with a linear projection

$$\tilde{\tau}(t_2) = \tilde{\tau}(t_1) + \mathcal{T}\bar{y}_1^{\mathcal{T}} \approx \tau(\tilde{t}_1) + \mathcal{T}\bar{y}_0^{\mathcal{T}}, \tag{4.22}$$

based on the assumption that the average frequencies of the two intervals are approximately equal. The estimation error would be

$$\mathcal{E} = \mathcal{T}\left(\bar{y}_1^{\mathcal{T}} - \bar{y}_0^{\mathcal{T}}\right), \tag{4.23}$$

with corresponding variance (assuming zero mean)

$$\sigma_e^2 = E\left\{\mathcal{E}^2\right\} = 2\mathcal{T}^2\sigma_y(\mathcal{T})^2, \tag{4.24}$$

and standard deviation

$$\sigma_e = \sqrt{2}\mathcal{T}\sigma_y(\mathcal{T}). \tag{4.25}$$

Figure 4.7 shows the Allan Deviation of common oscillator types. According to Fig.4.7, a quartz crystal oscillator may actually have comparable stability to a more expensive atomic clock for shorter time intervals, whereas in the long term the atomic clocks have better performance. Our goal is to provide position estimates once per second, so we are only interested in time intervals less than one second.

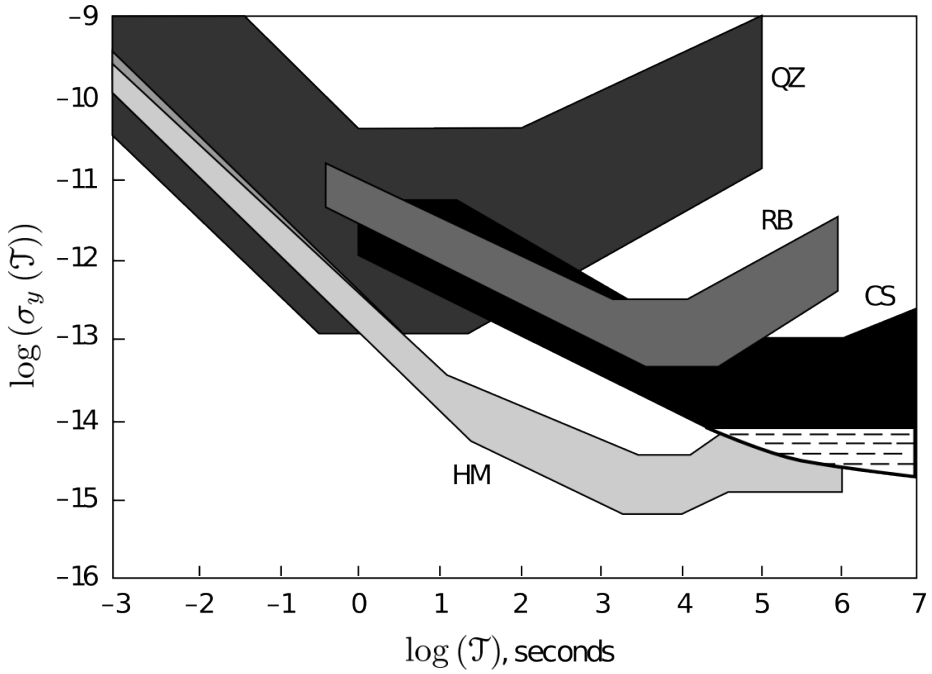

Figure 4.7: "A frequency stability diagram, for most of the precision clocks and oscillators used widely within the time and frequency community and by an ever-increasing number of users of precision timing devices. The dashed region at the bottom of the cesium (CS) stability plot shows the improved long-term stability of the HP 5071A Frequency RB Standard. QZ=Quartz Crystal Oscillator, RB=Rubidium Gas-Cell Frequency Standard, CS=Cesium-beam Frequency Standard, HM=ActiveHydrogen-Maser Frequency Standard."[1]

So suppose we modify our transactional synchronization approach slightly, capturing three signals instead of two. At times t_0 and t_1 the reference transceiver p will receive signals transmitted by the mobile transceiver q, and at time t_2 transceiver q will receive a signal transmitted by transceiver p.

$$\mathbf{r}_q(t_0) = \mathbf{h}_{q,p} \circ e^{-j(\boldsymbol{\omega}\tilde{\tau}_p(t_0)+\tilde{\theta}_q)} \tag{4.26}$$

$$\mathbf{r}_q(t_1) = \mathbf{h}_{q,p} \circ e^{-j(\boldsymbol{\omega}\tilde{\tau}_p(t_1)+\tilde{\theta}_q)} \tag{4.27}$$

$$\mathbf{r}_p(t_2) = \mathbf{h}_{q,p} \circ e^{-j(-\boldsymbol{\omega}\tilde{\tau}_p(t_2)+\tilde{\theta}_p)} \tag{4.28}$$

The average frequency over the interval (t_0, t_1) can be estimated,

$$\bar{y}_0^{\mathcal{T}} = \frac{\tilde{\tau}(t_1) - \tilde{\tau}(t_0)}{\mathcal{T}} = \frac{\angle\text{pole}\frac{[\mathbf{r}_q(t_1)]}{[\mathbf{r}_q(t_0)]}}{2\Delta\omega\mathcal{T}}. \tag{4.29}$$

This can then be used to predict $\tilde{\tau}_p(t_2)$ with Equation 4.22. This method can also be extended for the case of the alternative transactional synchronization described in Section 3.3.5.

A test was conducted to determine whether this scheme would perform accurately enough for our needs. Our current mobile transmitter prototype was directly connected to one of our PPL transceiver units. The mobile unit used an internal crystal oscillator and the transceiver used an atomic clock, just as would be used in a TART implementation. The transceiver performed successive signal captures at times t_0,t_1 and t_2 with spacing $\mathcal{T}$. The error in predicting $\tilde{\tau}(t_2)$ from $\tilde{\tau}(t_0)$,$\tilde{\tau}(t_1)$ then measured. This procedure was repeated for 1000 trials and different interval sizes. The results of this experiment are shown in Figure 4.8.

Figure 4.8 shows the 3σ error for the clock predictions, which is three times the standard deviation. For a normal distribution 99.7 percent of estimates will have an error of less than the 3σ value. This means that for interval sizes less than 0.3 seconds, we can expect to have clock prediction errors of less than our 0.5 ns threshold 99.7 percent of the time.

This shows that a typical crystal oscillator on the mobile units may be acceptable with a time between transactions as large as 0.3 seconds, significantly improved over the worst case analysis described. In practice the interval size would certainly be chosen to be significantly smaller than 0.3 seconds, since TART also relies on the constant channel assumption. It is possible that in 0.3 seconds the mobile unit or other object in the RF environment has moved to significantly change

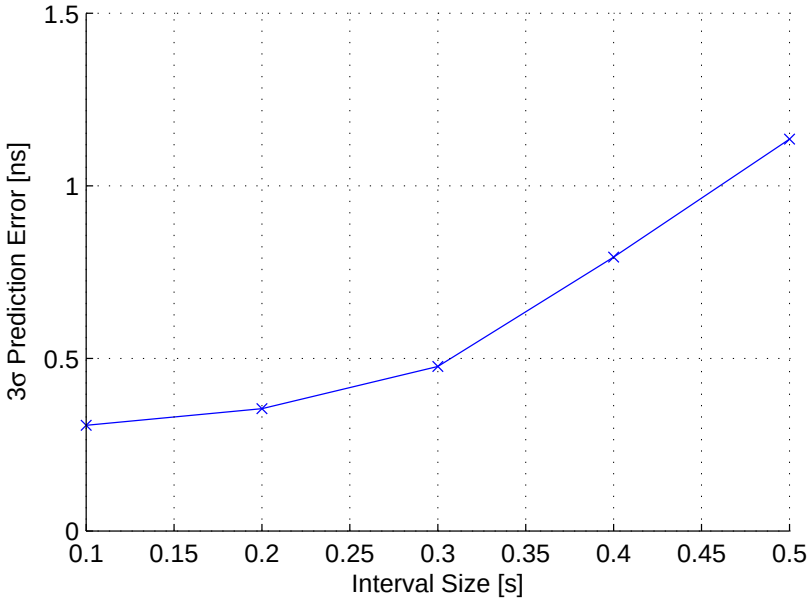

Figure 4.8: 3σ Clock Prediction Error for Different Interval Sizes

the channel response. For this reason the interval size should be no more than the order of tens of milliseconds.

Chapter 5

TART Perturbation Analysis

This chapter explores the behavior of TART when received signals are corrupted by noise. An analytic approximation for the performance of TART as a function of signal to noise ratio (SNR) will be presented, which is intended to provide intuition as to how TART position error is affected in different system geometries. This analysis will make simplifying assumptions to obtain a tractable analytic approximation, considering only the multipath-free case. The utility of the analytic approximation will then be verified with numerical simulation results. Ideal frequency response calibration and ideal transactional synchronization will also be assumed.

5.1 TART Reformulation

Let us first consider a more compact definition of the TART algorithm.

$$\overset{\star}{\mathbf{v}}_l = \underset{\overset{\#}{\mathbf{v}}_l}{\operatorname{argmax}} \sum_{p=1}^{P} \left| \left[e^{j\boldsymbol{\omega} \overset{\#}{t}_{0,p}\left(\overset{\#}{\mathbf{v}}_l\right)} \right]^T \mathbf{r}_p \right| \tag{5.1}$$

where the $\overset{\#}{t}_{0,p}$ is a function of $\overset{\#}{\mathbf{v}}_l$ as described in Equation 2.36, and $\overset{\star}{\mathbf{v}}_l$ is the TART position estimate. In summary, the received signal vector from reference antenna p is first rephased by $\overset{\#}{t}_{0,p}$; then the resulting vector's entries are summed. Both of these operations occur within the inner product in Equation 5.1. The resultant scalar has it's complex magnitude computed, and these magnitude values are summed over all P reference antennas to produce the TART metric. Whichever position vector $\overset{\#}{\mathbf{v}}_l$ maximizes this quantity is the estimate of the position of the mobile locator.

A received signal vector to be processed by TART has the form $\mathbf{r}_p = \mathbf{h}_p e^{j\tilde{\theta}}$. TART however was specifically defined to ignore the frequency independent phase offset $\tilde{\theta}$, as discussed in Section 3.1. Thus without loss of generality, we can assume that $\tilde{\theta} = 0$; that is $\mathbf{h}_p$ and $\mathbf{h}_p e^{j\tilde{\theta}}$ must produce the same TART metric and position estimate.

We will consider the ideal channel where $\mathbf{r}_p = e^{-j\boldsymbol{\omega} t_{0,p}}$. After the rephasing and first summation step, we have

$$\left[e^{j\boldsymbol{\omega}\overset{\#}{t}_{0,p}\left(\overset{\#}{\mathbf{v}}_l\right)}\right]^T e^{-j\boldsymbol{\omega} t_{0,p}} = \sum_{m=1}^{M} e^{-j(\boldsymbol{\omega})_m\left(t_{0,p}-\overset{\#}{t}_{0,p}\left(\overset{\#}{\mathbf{v}}_l\right)\right)} \tag{5.2}$$

which is actually a multicarrier signal expressed as a function of $t_{0,p} - \overset{\#}{t}_{0,p}\left(\overset{\#}{\mathbf{v}}_l\right)$, the error between the test time delay and the true time delay. Unlike our original multicarrier definition in Equation 2.7, the terms have no phase shift relative to each other, so at the correct location $t_{0,p} - \overset{\#}{t}_{0,p}\left(\overset{\#}{\mathbf{v}}_l\right) = 0$ all terms add constructively to the value M. Thus our overall expression for the TART algorithm for this special case simplifies to

$$\overset{\star}{\mathbf{v}}_l = \underset{\overset{\#}{\mathbf{v}}_l}{\operatorname{argmax}} \sum_{p=1}^{P} \left| \sum_{m=1}^{M} e^{-j(\boldsymbol{\omega})_m\left(t_{0,p}-\overset{\#}{t}_{0,p}\left(\overset{\#}{\mathbf{v}}_l\right)\right)} \right|. \tag{5.3}$$

Let $\bar{\omega} = \omega_0 + \frac{M\Delta\omega}{2}$, the average value of the carrier frequencies. The TART expression can be rewritten as,

$$\overset{\star}{\mathbf{v}}_l = \underset{\overset{\#}{\mathbf{v}}_l}{\operatorname{argmax}} \sum_{p=1}^{P} \left| \sum_{m=1}^{M} e^{-j(\boldsymbol{\omega})_m\left(t_{0,p}-\overset{\#}{t}_{0,p}\left(\overset{\#}{\mathbf{v}}_l\right)\right)} \right| = \underset{\overset{\#}{\mathbf{v}}_l}{\operatorname{argmax}} \sum_{p=1}^{P} \left| \sum_{m=1}^{M} e^{-j((\boldsymbol{\omega})_m-\bar{\omega})\left(t_{0,p}-\overset{\#}{t}_{0,p}\left(\overset{\#}{\mathbf{v}}_l\right)\right)} e^{-j\bar{\omega}\left(t_{0,p}-\overset{\#}{t}_{0,p}\left(\overset{\#}{\mathbf{v}}_l\right)\right)} \right|. \tag{5.4}$$

Since $\left| e^{-j\bar{\omega}\left(t_{0,p}-\overset{\#}{t}_{0,p}\left(\overset{\#}{\mathbf{v}}_l\right)\right)} \right| = 1$,

$$\overset{\star}{\mathbf{v}}_l = \underset{\overset{\#}{\mathbf{v}}_l}{\operatorname{argmax}} \sum_{p=1}^{P} \left| \sum_{m=1}^{M} e^{-j((\boldsymbol{\omega})_m-\bar{\omega})\left(t_{0,p}-\overset{\#}{t}_{0,p}\left(\overset{\#}{\mathbf{v}}_l\right)\right)} \right|. \tag{5.5}$$

By subtracting the average carrier frequency we have centered the carrier frequencies about zero, with pairs of corresponding positive and negative frequencies. Henceforth we will make the substitution $\boldsymbol{\omega}_c = \boldsymbol{\omega} - \bar{\omega}\mathbf{1}_{M\times 1}$, and name the outcome the "centered" set of carrier frequencies. In the case where M is even we have,

$$\overset{\star}{\mathbf{v}}_l = \underset{\overset{\#}{\mathbf{v}}_l}{\operatorname{argmax}} \sum_{p=1}^{P} \left| \sum_{m=1}^{M/2} e^{-j(\boldsymbol{\omega}_c)_m\left(t_{0,p}-\overset{\#}{t}_{0,p}\left(\overset{\#}{\mathbf{v}}_l\right)\right)} + e^{j(\boldsymbol{\omega}_c)_m\left(t_{0,p}-\overset{\#}{t}_{0,p}\left(\overset{\#}{\mathbf{v}}_l\right)\right)} \right|, \tag{5.6}$$

which simplifies to

$$\overset{\star}{\mathbf{v}}_l = \underset{\overset{\#}{\mathbf{v}}_l}{\operatorname{argmax}} \sum_{p=1}^{P} \left| \sum_{m=1}^{M} \cos\left((\boldsymbol{\omega}_c)_m \left(t_{0,p} - \overset{\#}{t}_{0,p} \left(\overset{\#}{\mathbf{v}}_l \right) \right) \right) \right|. \tag{5.7}$$

In the case where M is odd we have,

$$\overset{\star}{\mathbf{v}}_l = \underset{\overset{\#}{\mathbf{v}}_l}{\operatorname{argmax}} \sum_{p=1}^{P} \left| 1 + 2 \sum_{m=1}^{(M-1)/2} \cos\left((\boldsymbol{\omega}_c)_m \left(t_{0,p} - \overset{\#}{t}_{0,p} \left(\overset{\#}{\mathbf{v}}_l \right) \right) \right) \right|. \tag{5.8}$$

For the remainder of this perturbation analysis we will treat on the case where M is even. This is for the sake of having a less cluttered argument. The treatment of the odd case may be derived in a nearly identical fashion if desired.

In the noise-free, multipath-free case it is known that the TART metric will be maximized at the true position, $\mathbf{v}_l$. For illustrative purposes we will consider a very simple case, in which there is a single reference antenna ($P = 1$) located at $\mathbf{v}_1 = [-10\ 0\ 0]^T$, the mobile locator at $\mathbf{v}_l = [0\ 0\ 0]^T$ and the solution scan space is restricted to the one-dimensional case along the x-axis, that is $\left(\overset{\#}{\mathbf{v}}_l \right)_1 \in (-10, 10)$ and $\left(\overset{\#}{\mathbf{v}}_l \right)_2 = \left(\overset{\#}{\mathbf{v}}_l \right)_3 = 0$. We will consider the multicarrier signal to be a typical case in practice for our past experiments, with $M = 86$, $\omega_0 = 3.7699 \cdot 10^9$ and $\Delta\omega = 7.3631 \cdot 10^6$. The resultant TART metric for each scan location along the x-axis is depicted by the blue curve in Figure 5.1. We see that the value of the curve is always greater than zero, as implied by the fact that the TART metric results from an absolute value operation.

We are interested in how the central peak of this curve will be perturbed when the received signals are corrupted with noise. As we are considering the small noise case, we will assume that only the shape of the curve near the peak is relevant. Recall our expression for TART,

$$\overset{\star}{\mathbf{v}}_l = \underset{\overset{\#}{\mathbf{v}}_l}{\operatorname{argmax}} \sum_{p=1}^{P} \left| \sum_{m=1}^{M} \cos\left((\boldsymbol{\omega}_c)_m \left(t_{0,p} - \overset{\#}{t}_{0,p} \left(\overset{\#}{\mathbf{v}}_l \right) \right) \right) \right|. \tag{5.9}$$

For the case that $\overset{\#}{\mathbf{v}}_l$ is close to the true location $\mathbf{v}_l$, the expression inside the absolute value must be positive and therefore the absolute value operation can be ignored in that case. Thus the TART metric near the central peak can be expressed as

$$\overset{\star}{\mathbf{v}}_l = \underset{\overset{\#}{\mathbf{v}}_l}{\operatorname{argmax}} \sum_{p=1}^{P} \sum_{m=1}^{M} \cos\left((\boldsymbol{\omega}_c)_m \left(t_{0,p} - \overset{\#}{t}_{0,p} \left(\overset{\#}{\mathbf{v}}_l \right) \right) \right). \tag{5.10}$$

This equivalent expression for the central peak is depicted as the dashed red line in Figure 5.1 for the one-dimensional case.

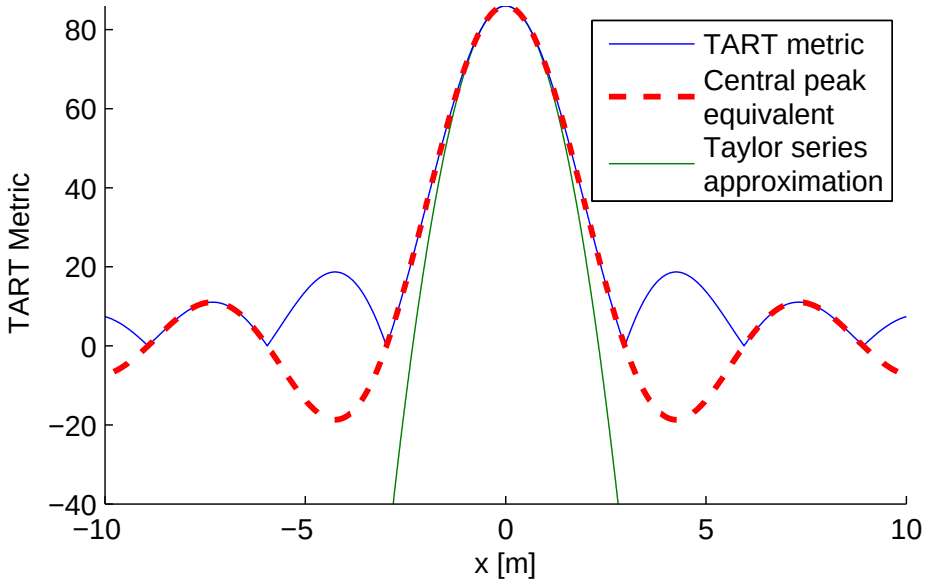

Figure 5.1: Simulation: One-Dimensional TART Scan

5.2 Received Signals with Complex Gaussian Noise

Next we will define the complex normal distribution. Suppose that $\tilde{\mathbf{a}}$ and $\tilde{\mathbf{b}}$ are vectors in $\mathbb{R}^m$ where each element is a normally distributed random variable. Then the vector

$$\tilde{\mathbf{z}} = \tilde{\mathbf{a}} + j\tilde{\mathbf{b}} \tag{5.11}$$

has the complex normal distribution. This distribution can be characterized with three parameters,

$$\boldsymbol{\mu} = E\{\tilde{\mathbf{z}}\}, \boldsymbol{\Gamma} = E\left\{(\tilde{\mathbf{z}} - \boldsymbol{\mu})(\tilde{\mathbf{z}} - \boldsymbol{\mu})^H\right\}, \text{ and } \mathbf{C} = E\left\{(\tilde{\mathbf{z}} - \boldsymbol{\mu})(\tilde{\mathbf{z}} - \boldsymbol{\mu})^T\right\}, \tag{5.12}$$

where ^{H} denotes the Hermitian (conjugate) transpose operation. The parameter $\boldsymbol{\mu}$ represents the mean value, $\boldsymbol{\Gamma}$ is the covariance matrix, and $\mathbf{C}$ is the relation matrix. A complex normal distribution is said to be circular if $\mathbf{C} = \mathbf{0}$. For the purposes of this perturbation analysis we will assume circular complex normal distributions defined with only two parameters, e.g. $\tilde{\mathbf{z}} \sim C(\boldsymbol{\mu}, \boldsymbol{\Gamma})$. The probability density function for the circularly symmetric case is

$$p(\mathbf{w}) = \frac{1}{\pi^m \det \boldsymbol{\Gamma}} e^{-(\mathbf{w}-\boldsymbol{\mu})^H \boldsymbol{\Gamma}^{-1}(\mathbf{w}-\boldsymbol{\mu})}, \tag{5.13}$$

where "det" represents the determinant operation.[18]

We will define a particular zero-mean complex Gaussian random variable $\tilde{\mathbf{w}}_p \sim C(\mathbf{0}, \sigma^2\mathbf{I})$, to be the noise vector added to the ideal signal for the pth reference antenna. It is assumed that all of the noise terms in each vector $\tilde{\mathbf{w}}_p$ are independent and uncorrelated (hence $\mathbf{\Gamma} = \sigma^2\mathbf{I}$) and the noise vectors for each reference antenna are also independent and uncorrelated. This is true when the received signal noise is dominated by thermal noise, as is encountered in practice.

The received signal for antenna p in this case for an ideal channel with noise is therefore

$$\mathbf{r}_p = e^{-j\boldsymbol{\omega}t_{0,p}} + \tilde{\mathbf{w}}_p. \tag{5.14}$$

Using this as our received signal in our TART expression we have,

$$\overset{\star}{\mathbf{v}}_l = \underset{\overset{\#}{\mathbf{v}}_l}{\operatorname{argmax}} \sum_{p=1}^{P} \left| \left[e^{j\boldsymbol{\omega}\overset{\#}{t}_{0,p}\left(\overset{\#}{\mathbf{v}}_l\right)} \right]^T \left(e^{-j\boldsymbol{\omega}t_{0,p}} + \tilde{\mathbf{w}}_p \right) \right|, \tag{5.15}$$

$$\overset{\star}{\mathbf{v}}_l = \underset{\overset{\#}{\mathbf{v}}_l}{\operatorname{argmax}} \sum_{p=1}^{P} \left| \left(\sum_{m=1}^{M} e^{-j(\boldsymbol{\omega})_m \left(t_{0,p} - \overset{\#}{t}_{0,p}\left(\overset{\#}{\mathbf{v}}_l\right) \right)} \right) + \left[e^{j\boldsymbol{\omega}\overset{\#}{t}_{0,p}\left(\overset{\#}{\mathbf{v}}_l\right)} \right]^T \tilde{\mathbf{w}}_p \right|. \tag{5.16}$$

We can again "center" our frequencies by removing $\bar{\omega}$.

$$\overset{\star}{\mathbf{v}}_l = \underset{\overset{\#}{\mathbf{v}}_l}{\operatorname{argmax}} \sum_{p=1}^{P} \left| \left(\sum_{m=1}^{M} e^{-j(\boldsymbol{\omega}_c)_m \left(t_{0,p} - \overset{\#}{t}_{0,p}\left(\overset{\#}{\mathbf{v}}_l\right) \right)} \right) + e^{j\bar{\omega}\left(t_{0,p} - \overset{\#}{t}_{0,p}\left(\overset{\#}{\mathbf{v}}_l\right) \right)} \left[e^{j\boldsymbol{\omega}\overset{\#}{t}_{0,p}\left(\overset{\#}{\mathbf{v}}_l\right)} \right]^T \tilde{\mathbf{w}}_p \right|, \tag{5.17}$$

$$\overset{\star}{\mathbf{v}}_l = \underset{\overset{\#}{\mathbf{v}}_l}{\operatorname{argmax}} \sum_{p=1}^{P} \left| \left(\sum_{m=1}^{M} \cos\left((\boldsymbol{\omega}_c)_m \left(t_{0,p} - \overset{\#}{t}_{0,p}\left(\overset{\#}{\mathbf{v}}_l\right) \right) \right) \right) + e^{j\bar{\omega}t_{0,p}} \left[e^{j\boldsymbol{\omega}_c\overset{\#}{t}_{0,p}\left(\overset{\#}{\mathbf{v}}_l\right)} \right]^T \tilde{\mathbf{w}}_p \right|. \tag{5.18}$$

5.3 Rephasing and Summation Step

Let us consider the effects of the rephasing and summation step with a noisy received signal. Using our transformation to "centered" frequencies, the rephasing step becomes,

$$\left[e^{j\boldsymbol{\omega}\overset{\#}{t}_{0,p}\left(\overset{\#}{\mathbf{v}}_l\right)} \right]^T \left(e^{-j\boldsymbol{\omega}t_{0,p}} + \tilde{\mathbf{w}}_p \right) = \left(\sum_{m=1}^{M} \cos\left((\boldsymbol{\omega}_c)_m \left(t_{0,p} - \overset{\#}{t}_{0,p}\left(\overset{\#}{\mathbf{v}}_l\right) \right) \right) \right) + e^{j\bar{\omega}t_{0,p}} \left[e^{j\boldsymbol{\omega}_c\overset{\#}{t}_{0,p}\left(\overset{\#}{\mathbf{v}}_l\right)} \right]^T \tilde{\mathbf{w}}_p \tag{5.19}$$

A useful property of complex multivariate normal random vectors is that after a linear transformation the output also has a complex multivariate normal distribution. Specifically, for a complex multivariate Gaussian vector $\tilde{\mathbf{a}} \sim C(\boldsymbol{\mu}, \mathbf{\Gamma})$, if $\tilde{\mathbf{b}} = \mathbf{C}\tilde{\mathbf{a}}$, then $\tilde{\mathbf{b}} \sim C\left(\mathbf{C}\boldsymbol{\mu}, \mathbf{C}\mathbf{\Gamma}\mathbf{C}^H\right)$.[18] This implies that the rephased noise term

$$e^{j\bar{\omega}t_{0,p}} \left[e^{j\boldsymbol{\omega}_c\overset{\#}{t}_{0,p}\left(\overset{\#}{\mathbf{v}}_l\right)} \right]^T \tilde{\mathbf{w}}_p \sim C\left(e^{j\bar{\omega}t_{0,p}} \left[e^{j\boldsymbol{\omega}_c\overset{\#}{t}_{0,p}\left(\overset{\#}{\mathbf{v}}_l\right)} \right]^T \mathbf{0}, e^{j\bar{\omega}t_{0,p}} \left[e^{j\boldsymbol{\omega}_c\overset{\#}{t}_{0,p}\left(\overset{\#}{\mathbf{v}}_l\right)} \right]^T \sigma^2\mathbf{I} \left(e^{j\bar{\omega}t_{0,p}} \left[e^{j\boldsymbol{\omega}_c\overset{\#}{t}_{0,p}\left(\overset{\#}{\mathbf{v}}_l\right)} \right]^T \right)^H \right), \tag{5.20}$$

which simplifies to

$$\overbrace{e^{j\bar{\omega}t_{0,p}}\left[e^{j\boldsymbol{\omega}_c \overset{\#}{t}_{0,p}\left(\overset{\#}{\mathbf{v}}_l\right)}\right]^T \tilde{\mathbf{w}}_p}^{\tilde{w}_p^r\left(\overset{\#}{\mathbf{v}}_l\right)} \sim C\left(0, M\sigma^2\right). \tag{5.21}$$

For convenience we will denote this quantity, the noise component that has been rephased and summed to test location $\overset{\#}{\mathbf{v}}_l$, as $\tilde{w}_p^r\left(\overset{\#}{\mathbf{v}}_l\right)$. The superscript r is an abbreviation for "rephased and summed." As we propagate the noise terms through the various steps of the TART algorithm we will also introduce $\tilde{w}_p^{r,m}\left(\overset{\#}{\mathbf{v}}_l\right)$ and $\tilde{w}^{r,m,s}\left(\overset{\#}{\mathbf{v}}_l\right)$, where the superscript m is an abbreviation for "magnitude" and s for "summed."

Equation 5.21 implies that the result of the rephasing and summation step has a distribution that does not depend on the time shift $\overset{\#}{t}_{0,p}\left(\overset{\#}{\mathbf{v}}_l\right)$. We are interested in rephasing with many possible time shifts as TART scans the solution space to maximize its metric. Consider the received signal being rephased to two different locations, $\overset{\#}{\mathbf{v}}_{l,1}$ and $\overset{\#}{\mathbf{v}}_{l,1}$. We can observe the relationship of the results of the rephasing and summation step for the two cases by creating a vector from the two results, which can be factored as follows,

$$\begin{bmatrix} \tilde{w}_p^r\left(\overset{\#}{\mathbf{v}}_{l,1}\right) \\ \tilde{w}_p^r\left(\overset{\#}{\mathbf{v}}_{l,2}\right) \end{bmatrix} = \begin{bmatrix} e^{j\bar{\omega}t_{0,p}}\left[e^{j\boldsymbol{\omega}_c \overset{\#}{t}_{0,p}\left(\overset{\#}{\mathbf{v}}_{l,1}\right)}\right]^T \tilde{\mathbf{w}}_p \\ e^{j\bar{\omega}t_{0,p}}\left[e^{j\boldsymbol{\omega}_c \overset{\#}{t}_{0,p}\left(\overset{\#}{\mathbf{v}}_{l,2}\right)}\right]^T \tilde{\mathbf{w}}_p \end{bmatrix} = e^{j\bar{\omega}t_{0,p}}\left[e^{j\boldsymbol{\omega}_c \overset{\#}{t}_{0,p}\left(\overset{\#}{\mathbf{v}}_{l,1}\right)} \quad e^{j\boldsymbol{\omega}_c \overset{\#}{t}_{0,p}\left(\overset{\#}{\mathbf{v}}_{l,2}\right)}\right]^T \tilde{\mathbf{w}}_p. \tag{5.22}$$

We again have a complex multivariate normal random vector undergoing a linear transformation. The the joint distribution can be determined to be

$$\begin{bmatrix} \tilde{w}_p^r\left(\overset{\#}{\mathbf{v}}_{l,1}\right) \\ \tilde{w}_p^r\left(\overset{\#}{\mathbf{v}}_{l,2}\right) \end{bmatrix} \sim C\left(\mathbf{0}, \sigma^2\begin{bmatrix} M & \sum_{m=1}^M e^{j(\boldsymbol{\omega}_c)_m\left(\overset{\#}{t}_{0,p}\left(\overset{\#}{\mathbf{v}}_{l,1}\right)-\overset{\#}{t}_{0,p}\left(\overset{\#}{\mathbf{v}}_{l,2}\right)\right)} \\ \sum_{m=1}^M e^{j(\boldsymbol{\omega}_c)_m\left(\overset{\#}{t}_{0,p}\left(\overset{\#}{\mathbf{v}}_{l,2}\right)-\overset{\#}{t}_{0,p}\left(\overset{\#}{\mathbf{v}}_{l,1}\right)\right)} & M \end{bmatrix}\right). \tag{5.23}$$

Since we are using centered frequencies,

$$\begin{bmatrix} \tilde{w}_p^r\left(\overset{\#}{\mathbf{v}}_{l,1}\right) \\ \tilde{w}_p^r\left(\overset{\#}{\mathbf{v}}_{l,2}\right) \end{bmatrix} \sim \dots$$

$$C\left(\mathbf{0}, \sigma^2\begin{bmatrix} M & \sum_{m=1}^M \cos\left((\boldsymbol{\omega}_c)_m\left(\overset{\#}{t}_{0,p}\left(\overset{\#}{\mathbf{v}}_{l,1}\right)-\overset{\#}{t}_{0,p}\left(\overset{\#}{\mathbf{v}}_{l,2}\right)\right)\right) \\ \sum_{m=1}^M \cos\left((\boldsymbol{\omega}_c)_m\left(\overset{\#}{t}_{0,p}\left(\overset{\#}{\mathbf{v}}_{l,2}\right)-\overset{\#}{t}_{0,p}\left(\overset{\#}{\mathbf{v}}_{l,1}\right)\right)\right) & M \end{bmatrix}\right). \tag{5.24}$$

5.4 Complex Magnitude Step

In summary, after the rephasing and summation step, the received signal vector from each antenna has been reduced to a scalar value with an ideal component and a noise component (see Equation 5.19). The sum of the zero-mean noise term with the ideal term can be said to have distribution

$$\sum_{m=1}^{M} \cos\left((\boldsymbol{\omega}_c)_m \left(t_{0,p} - \overset{\#}{t}_{0,p}\left(\overset{\#}{\mathbf{v}}_l\right)\right)\right) + \tilde{w}_p^r\left(\overset{\#}{\mathbf{v}}_l\right) \sim C\left(\sum_{m=1}^{M} \cos\left((\boldsymbol{\omega}_c)_m \left(t_{0,p} - \overset{\#}{t}_{0,p}\left(\overset{\#}{\mathbf{v}}_l\right)\right)\right), M\sigma^2\right), \quad (5.25)$$

where the ideal term has become the mean of this complex normal distribution.

Next we will define the Rice probability distribution. For independent normal random variables $\tilde{a} \sim N\left(\nu\cos\theta, \sigma^2\right)$ and $\tilde{b} \sim N\left(\nu\sin\theta, \sigma^2\right)$, then $\tilde{z} = \sqrt{\tilde{a}^2 + \tilde{b}^2}$ is said to have a Rice distribution for any real number θ. Thus the magnitude of a complex normal random variable has the Rice distribution. The Rice distribution is uniquely determined by the two parameters ν and σ^2, e.g. $\tilde{z} \sim R\left(\nu, \sigma^2\right)$. The probability density function is

$$p\left(x\,|\nu, \sigma^2\right) = \frac{x}{\sigma^2} e^{\left(\frac{-\left(x^2+\nu^2\right)}{2\sigma^2}\right)} I_0\left(\frac{x\nu}{\sigma^2}\right), \quad (5.26)$$

where I_0 is a modified Bessel function of the first kind with order 0. The parameters ν, σ^2 do not represent the mean and the variance of the distribution. Determining these requires the more complicated formulations below:

$$E\left\{\tilde{z}\right\} = \sigma\sqrt{\frac{\pi}{2}} L_{1/2}\left(\frac{-\nu^2}{2\sigma^2}\right), \quad (5.27)$$

$$E\left\{\left(\tilde{z} - E\left\{\tilde{z}\right\}\right)^2\right\} = 2\sigma^2 + \nu^2 - \frac{\pi\sigma^2}{2} L_{1/2}\left(\frac{-\nu^2}{2\sigma^2}\right), \quad (5.28)$$

where $L_{1/2}$ denotes a Laguerre polynomial,

$$L_{1/2}(x) = e^{\frac{x}{2}}\left[(1-x)I_0\left(\frac{-x}{2}\right) - xI_1\left(\frac{-x}{2}\right)\right], \quad (5.29)$$

where I_0 and I_1 are modified Bessel functions of the first kind with orders 0 and 1 respectively.[5]

After the rephasing and summation step of the TART process, the resultant complex scalar has its magnitude computed, which results in a random variable with the Rice distribution,

$$\left|\sum_{m=1}^{M} \cos\left((\boldsymbol{\omega}_c)_m \left(t_{0,p} - \overset{\#}{t}_{0,p}\left(\overset{\#}{\mathbf{v}}_l\right)\right)\right) + \tilde{w}_p^r\left(\overset{\#}{\mathbf{v}}_l\right)\right| \sim R\left(\sum_{m=1}^{M} \cos\left((\boldsymbol{\omega}_c)_m \left(t_{0,p} - \overset{\#}{t}_{0,p}\left(\overset{\#}{\mathbf{v}}_l\right)\right)\right), M\sigma^2\right). \quad (5.30)$$

As shown, the equations governing the Rice distribution are considerably more complicated than the Gaussian distribution. These must be represented in terms of modified Bessel functions for which no closed form exists. Further, representations of the joint distribution between two Rice distributed random variables are even more complicated, generally being expressed as an infinite series.[15]

The purpose of the analytic perturbation analysis to follow is to gain intuition as to how the performance in TART degrades for different geometries, which would almost certainly be obscured by the complexity of the Rice distribution equations. For this reason, an approximation will be made at this step in the analysis, where the Rice distribution will be approximated as a Gaussian distribution. This is valid for cases with large signal to noise ratio; in terms of the Rice parameters this is the case wherein ν is large relative to σ^2. This relationship is depicted in Figure 5.2, which shows the probability density functions for normal distributions $N(\mu, \sigma^2)$ and Rice distributions $R(\nu, \sigma^2)$. The value of σ is set to 1, while the value of μ is varied from 0 to 8. Since μ is real in this case we have $\mu = \nu$. We see that for large values of $\frac{\nu}{\sigma^2}$ the distributions are approximately equal.

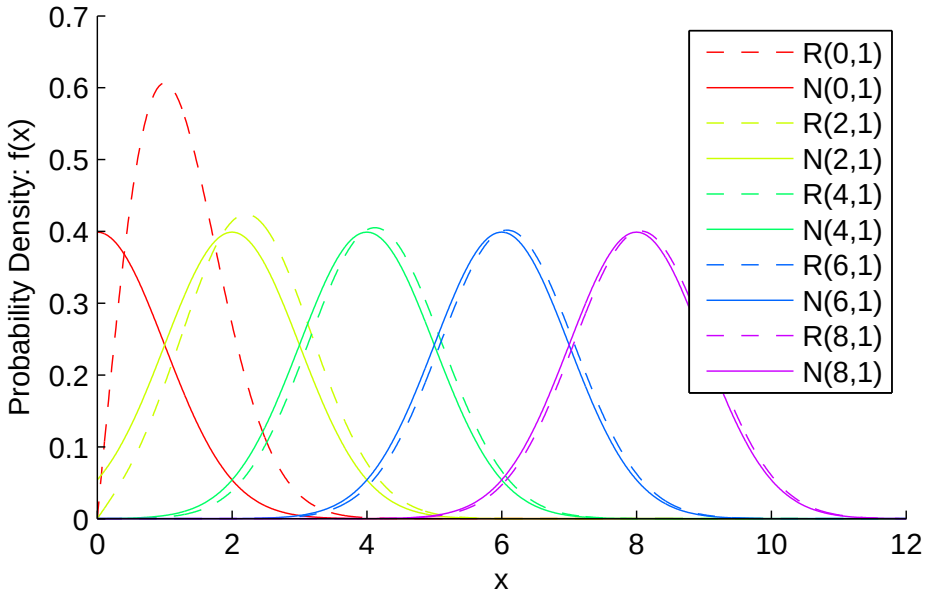

Figure 5.2: Relationship between Rice and Gaussian Distributions

Next we will discuss how to determine the Gaussian distribution with which to approximate the Rice distribution for our case. Conveniently, in our case ν takes on only real values. Consider an example in which we have a random variable $\tilde{w} \sim C(8 + 0j, 1)$. Figure 5.3 shows level contours of the probability density function of $\tilde{w}$ (given in Equation 5.13), which are concentric circles about

the mean, $8 + 0j$. Also shown are the level contours of $|\tilde{w}|$ from the corresponding Rice distribution which are centered about the origin, as the magnitude of a complex number is the Euclidean distance to the origin in the context of this Cartesian plot. We can see that the absolute value of the real part

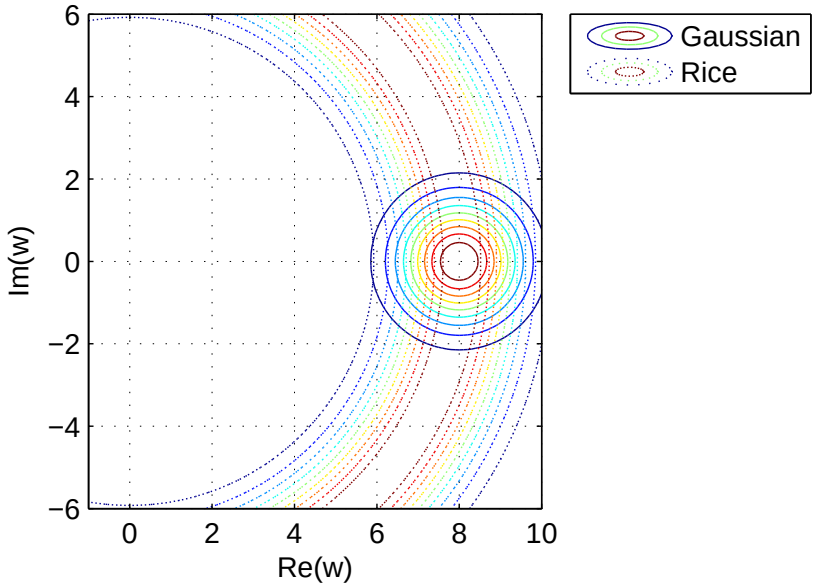

Figure 5.3: Gaussian and Rice Level Contours

of the Gaussian distribution is approximately equal to its magnitude.

For values of $\overset{\#}{\mathbf{v}}_l$ near the central peak, we have the case that ν is both real and positive. Thus we can make the approximation that

$$\left|\sum_{m=1}^{M}\cos\left((\boldsymbol{\omega}_c)_m\left(t_{0,p}-\overset{\#}{t}_{0,p}\left(\overset{\#}{\mathbf{v}}_l\right)\right)\right)+\tilde{w}_p^r\left(\overset{\#}{\mathbf{v}}_l\right)\right|\approx\sum_{m=1}^{M}\cos\left((\boldsymbol{\omega}_c)_m\left(t_{0,p}-\overset{\#}{t}_{0,p}\left(\overset{\#}{\mathbf{v}}_l\right)\right)\right)+\mathrm{Re}\left(\tilde{w}_p^r\left(\overset{\#}{\mathbf{v}}_l\right)\right). \tag{5.31}$$

The real and imaginary components of a circular complex random vector $\tilde{\mathbf{w}} \sim C(\boldsymbol{\mu}, \boldsymbol{\Gamma})$ can be considered a real multivariate normal distribution with

$$\begin{bmatrix}\mathrm{Re}(\tilde{\mathbf{w}})\\ \mathrm{Im}(\tilde{\mathbf{w}})\end{bmatrix}\sim N\left(\begin{bmatrix}\mathrm{Re}(\boldsymbol{\mu})\\ \mathrm{Im}(\boldsymbol{\mu})\end{bmatrix},\frac{1}{2}\begin{bmatrix}\mathrm{Re}(\boldsymbol{\Gamma}) & -\mathrm{Im}(\boldsymbol{\Gamma})\\ \mathrm{Im}(\boldsymbol{\Gamma}) & \mathrm{Re}(\boldsymbol{\Gamma})\end{bmatrix}\right).[18] \tag{5.32}$$

Since $\tilde{w}_p^r\left(\overset{\#}{\mathbf{v}}_l\right) \sim C\left(0, M\sigma^2\right)$, this implies $\mathrm{Re}\left(\tilde{w}_p^r\left(\overset{\#}{\mathbf{v}}_l\right)\right) \sim N\left(0, \frac{1}{2}M\sigma^2\right)$. We will denote $\tilde{w}_p^{r,m}\left(\overset{\#}{\mathbf{v}}_l\right)$ to be equal to $\mathrm{Re}\left(\tilde{w}_p^r\left(\overset{\#}{\mathbf{v}}_l\right)\right)$, the noise term after the rephasing/summation and magnitude steps.

Now let us again consider the relationship between the results of rephasing at two different test

locations. From Equations 5.24 and 5.32 we have

$$\begin{bmatrix} \tilde{w}_p^{r,m}\left(\overset{\#}{\mathbf{v}}_{l,1}\right) \\ \tilde{w}_p^{r,m}\left(\overset{\#}{\mathbf{v}}_{l,2}\right) \end{bmatrix} \sim \dots$$
$$N\left(\mathbf{0}, \frac{\sigma^2}{2}\begin{bmatrix} M & \sum_{m=1}^{M}\cos\left((\boldsymbol{\omega}_c)_m\left(\overset{\#}{t}_{0,p}\left(\overset{\#}{\mathbf{v}}_{l,1}\right)-\overset{\#}{t}_{0,p}\left(\overset{\#}{\mathbf{v}}_{l,2}\right)\right)\right) \\ \sum_{m=1}^{M}\cos\left((\boldsymbol{\omega}_c)_m\left(\overset{\#}{t}_{0,p}\left(\overset{\#}{\mathbf{v}}_{l,1}\right)-\overset{\#}{t}_{0,p}\left(\overset{\#}{\mathbf{v}}_{l,2}\right)\right)\right) & M \end{bmatrix}\right) \tag{5.33}$$

5.5 Second Summation Step

After the complex magnitude is computed, the resultant values are summed for each of P reference antennas generating the TART metric value for a particular test location. With the aforementioned approximation

$$\sum_{p=1}^{P}\left|\sum_{m=1}^{M}\cos\left((\boldsymbol{\omega}_c)_m\left(t_{0,p}-\overset{\#}{t}_{0,p}\left(\overset{\#}{\mathbf{v}}_l\right)\right)\right)+\tilde{w}_p^r\right| \approx \sum_{p=1}^{P}\left|\sum_{m=1}^{M}\cos\left((\boldsymbol{\omega}_c)_m\left(t_{0,p}-\overset{\#}{t}_{0,p}\left(\overset{\#}{\mathbf{v}}_l\right)\right)\right)\right| + \overbrace{\sum_{p=1}^{P}\tilde{w}_p^{r,m}\left(\overset{\#}{\mathbf{v}}_l\right)}^{\tilde{w}^{r,m,s}\left(\overset{\#}{\mathbf{v}}_l\right)}. \tag{5.34}$$

The noise term after this summation will be denoted $\tilde{w}^{r,m,s}\left(\overset{\#}{\mathbf{v}}_l\right)$. After the summation over the antennas the noise term becomes

$$\tilde{w}^{r,m,s}\left(\overset{\#}{\mathbf{v}}_l\right) = \mathbf{1}_{1\times P}\left[\tilde{w}_1^{r,m}\left(\overset{\#}{\mathbf{v}}_l\right)\dots\tilde{w}_p^{r,m}\left(\overset{\#}{\mathbf{v}}_l\right)\dots\tilde{w}_P^{r,m}\left(\overset{\#}{\mathbf{v}}_l\right)\right]^T. \tag{5.35}$$

As stated previously, the noise terms for each antenna are assumed to be independent, therefore

$$\left[\tilde{w}_1^{r,m}\left(\overset{\#}{\mathbf{v}}_l\right)\dots\tilde{w}_p^{r,m}\left(\overset{\#}{\mathbf{v}}_l\right)\dots\tilde{w}_P^{r,m}\left(\overset{\#}{\mathbf{v}}_l\right)\right]^T \sim N\left(\mathbf{0}, \frac{1}{2}M\sigma^2\mathbf{I}\right). \tag{5.36}$$

After the summation over antennas we have,

$$\tilde{w}^{r,m,s}\left(\overset{\#}{\mathbf{v}}_l\right) \sim N\left(0, \frac{1}{2}MP\sigma^2\right). \tag{5.37}$$

Relating two different test locations,

$$\begin{bmatrix} \tilde{w}^{r,m,s}\left(\overset{\#}{\mathbf{v}}_{l,1}\right) \\ \tilde{w}^{r,m,s}\left(\overset{\#}{\mathbf{v}}_{l,2}\right) \end{bmatrix} = \begin{bmatrix} 1 & 0 & \dots & 1 & 0 & \dots & 1 & 0 \\ 0 & 1 & \dots & 0 & 1 & \dots & 0 & 1 \end{bmatrix} \begin{bmatrix} \tilde{w}_1^{r,m}\left(\overset{\#}{\mathbf{v}}_{l,1}\right) \\ \tilde{w}_1^{r,m}\left(\overset{\#}{\mathbf{v}}_{l,2}\right) \\ \vdots \\ \tilde{w}_p^{r,m}\left(\overset{\#}{\mathbf{v}}_{l,1}\right) \\ \tilde{w}_p^{r,m}\left(\overset{\#}{\mathbf{v}}_{l,2}\right) \\ \vdots \\ \tilde{w}_P^{r,m}\left(\overset{\#}{\mathbf{v}}_{l,1}\right) \\ \tilde{w}_P^{r,m}\left(\overset{\#}{\mathbf{v}}_{l,2}\right) \end{bmatrix} \tag{5.38}$$

The distribution is found to be

$$\begin{bmatrix} \tilde{w}_p^{r,m,s}\left(\overset{\#}{\mathbf{v}}_{l,1}\right) \\ \tilde{w}_p^{r,m,s}\left(\overset{\#}{\mathbf{v}}_{l,2}\right) \end{bmatrix} \sim \dots$$

$$N\left(\mathbf{0}, \frac{\sigma^2}{2}\sum_{p=1}^{P}\begin{bmatrix} M & \sum_{m=1}^{M}\cos\left((\boldsymbol{\omega}_c)_m\left(\overset{\#}{t}_{0,p}\left(\overset{\#}{\mathbf{v}}_{l,1}\right) - \overset{\#}{t}_{0,p}\left(\overset{\#}{\mathbf{v}}_{l,2}\right)\right)\right) \\ \sum_{m=1}^{M}\cos\left((\boldsymbol{\omega}_c)_m\left(\overset{\#}{t}_{0,p}\left(\overset{\#}{\mathbf{v}}_{l,1}\right) - \overset{\#}{t}_{0,p}\left(\overset{\#}{\mathbf{v}}_{l,2}\right)\right)\right) & M \end{bmatrix}\right) \tag{5.39}$$

In summary we have shown that the TART metric for received signals with noise can be approximated with an additive noise model, in which an ideal metric value is summed with a normally distributed noise term. Expressions for the mean and variance of the metric noise term, and covariance of the metric noise between any two test locations have been derived.

5.6 Argument of the Maximum Step

Next we will consider the final step the TART algorithm, in which the position that maximizes the TART metric is chosen as the position estimate. We will approximate the TART position estimate error by using a second order Taylor series model of the ideal TART metric and a first order Taylor series model of the noise term near the ideal solution. If we denote the ideal TART metric as $f\left(\overset{\#}{\mathbf{v}}_l\right)$,

then our current model of the TART metric will be approximated near the true location $\mathbf{v}_l$ by,

$$f\left(\overset{\#}{\mathbf{v}}_l\right) + \tilde{w}^{r,m,s}\left(\overset{\#}{\mathbf{v}}_l\right) \approx f(\mathbf{v}_l) + [\overset{\#}{\mathbf{v}}_l - \mathbf{v}_l]^T \nabla f(\mathbf{v}_l) + \frac{1}{2}[\overset{\#}{\mathbf{v}}_l - \mathbf{v}_l]^T \nabla\nabla^T f(\mathbf{v}_l)\,[\mathbf{v}_l - \overset{\#}{\mathbf{v}}_l] \ldots + \tilde{w}^{r,m,s}(\mathbf{v}_l) + [\overset{\#}{\mathbf{v}}_l - \mathbf{v}_l]^T \nabla \tilde{w}^{r,m,s}(\mathbf{v}_l)\,. \tag{5.40}$$

Note that $\nabla\nabla^T f(\mathbf{v}_l)$ produces the Hessian matrix of $f(\mathbf{v}_l)$, which is assumed to be symmetric as all derivatives of $f(\mathbf{v}_l)$ are continuous. Since $\nabla f(\mathbf{v}_l) = \mathbf{0}$ (the ideal metric has a maximum at the true location), we have

$$f\left(\overset{\#}{\mathbf{v}}_l\right) + \tilde{w}^{r,m,s}\left(\overset{\#}{\mathbf{v}}_l\right) \approx f(\mathbf{v}_l) + \frac{1}{2}[\overset{\#}{\mathbf{v}}_l - \mathbf{v}_l]^T \nabla\nabla^T f(\mathbf{v}_l)\,[\mathbf{v}_l - \overset{\#}{\mathbf{v}}_l] \ldots + \tilde{w}^{r,m,s}(\mathbf{v}_l) + [\overset{\#}{\mathbf{v}}_l - \mathbf{v}_l]^T \nabla \tilde{w}^{r,m,s}(\mathbf{v}_l)\,. \tag{5.41}$$

Figure 5.1 depicts the second order Taylor series approximation of the ideal TART metric for our one-dimensional example.

The position estimate $\overset{\star}{\mathbf{v}}_l$ is the value of $\overset{\#}{\mathbf{v}}_l$ at which the TART metric is maximized, which is the location at which the gradient of our model of the peak is zero. Taking the gradient of the above expression with respect to $\overset{\#}{\mathbf{v}}_l$ and equating it to zero we obtain,

$$\begin{aligned}\mathbf{0} =& \nabla\big(f(\mathbf{v}_l) + \frac{1}{2}[\overset{\star}{\mathbf{v}}_l - \mathbf{v}_l]^T \nabla\nabla^T f(\mathbf{v}_l)\,[[\overset{\star}{\mathbf{v}}_l - \mathbf{v}_l] \ldots \\ &+ \tilde{w}^{r,m,s}(\mathbf{v}_l) + [\overset{\star}{\mathbf{v}}_l - \mathbf{v}_l]^T \nabla \tilde{w}^{r,m,s}(\mathbf{v}_l)\big) \\ =& \frac{1}{2}\nabla[\overset{\star}{\mathbf{v}}_l - \mathbf{v}_l]^T \nabla\nabla^T f(\mathbf{v}_l)\,[\overset{\star}{\mathbf{v}}_l - \mathbf{v}_l] + \nabla[\overset{\star}{\mathbf{v}}_l - \mathbf{v}_l]^T \nabla \tilde{w}^{r,m,s}(\mathbf{v}_l)\end{aligned} \tag{5.42}$$

We can rewrite the quadratic term as,

$$\frac{1}{2}\nabla[\overset{\star}{\mathbf{v}}_l - \mathbf{v}_l]^T \nabla\nabla^T f(\mathbf{v}_l)[\overset{\star}{\mathbf{v}}_l - \mathbf{v}_l] = \frac{1}{2}\nabla[\overset{\star}{\mathbf{v}}_l - \mathbf{v}_l]^T \begin{bmatrix} \frac{d^2 f(\mathbf{v}_l)}{dx^2} & \frac{d^2 f(\mathbf{v}_l)}{dxdy} & \frac{d^2 f(\mathbf{v}_l)}{dxdz} \\ \frac{d^2 f(\mathbf{v}_l)}{dxdy} & \frac{d^2 f(\mathbf{v}_l)}{dy^2} & \frac{d^2 f(\mathbf{v}_l)}{dydz} \\ \frac{d^2 f(\mathbf{v}_l)}{dxdz} & \frac{d^2 f(\mathbf{v}_l)}{dydz} & \frac{d^2 f(\mathbf{v}_l)}{dz^2} \end{bmatrix} [\overset{\star}{\mathbf{v}}_l - \mathbf{v}_l]$$

$$= \frac{1}{2}\nabla\Bigg(\frac{d^2 f(\mathbf{v}_l)}{dx^2}\left(\left(\overset{\star}{\mathbf{v}}_l\right)_1 - (\mathbf{v}_l)_1\right)^2 + \frac{d^2 f(\mathbf{v}_l)}{dxy}\left(\left(\overset{\star}{\mathbf{v}}_l\right)_1 - (\mathbf{v}_l)_1\right)\left(\left(\overset{\star}{\mathbf{v}}_l\right)_2 - (\mathbf{v}_l)_2\right)\dots$$

$$+ \frac{d^2 f(\mathbf{v}_l)}{dxz}\left(\left(\overset{\star}{\mathbf{v}}_l\right)_1 - (\mathbf{v}_l)_1\right)\left(\left(\overset{\star}{\mathbf{v}}_l\right)_3 - (\mathbf{v}_l)_3\right)\frac{d^2 f(\mathbf{v}_l)}{dy^2}\left(\left(\overset{\star}{\mathbf{v}}_l\right)_2 - (\mathbf{v}_l)_2\right)^2\dots$$

$$+ \frac{d^2 f(\mathbf{v}_l)}{dyz}\left(\left(\overset{\star}{\mathbf{v}}_l\right)_2 - (\mathbf{v}_l)_2\right)\left(\left(\overset{\star}{\mathbf{v}}_l\right)_3 - (\mathbf{v}_l)_3\right)\frac{d^2 f(\mathbf{v}_l)}{dz^2}\left(\left(\overset{\star}{\mathbf{v}}_l\right)_3 - (\mathbf{v}_l)_3\right)^2\Bigg)$$

$$= \begin{bmatrix} \frac{d^2 f(\mathbf{v}_l)}{dx^2}\left(\left(\overset{\star}{\mathbf{v}}_l\right)_1 - (\mathbf{v}_l)_1\right) + \frac{d^2 f(\mathbf{v}_l)}{dxy}\left(\left(\overset{\star}{\mathbf{v}}_l\right)_2 - (\mathbf{v}_l)_2\right) + \frac{d^2 f(\mathbf{v}_l)}{dxz}\left(\left(\overset{\star}{\mathbf{v}}_l\right)_3 - (\mathbf{v}_l)_3\right) \\ \frac{d^2 f(\mathbf{v}_l)}{dxy}\left(\left(\overset{\star}{\mathbf{v}}_l\right)_1 - (\mathbf{v}_l)_1\right) + \frac{d^2 f(\mathbf{v}_l)}{dy^2}\left(\left(\overset{\star}{\mathbf{v}}_l\right)_2 - (\mathbf{v}_l)_2\right) + \frac{d^2 f(\mathbf{v}_l)}{dyz}\left(\left(\overset{\star}{\mathbf{v}}_l\right)_3 - (\mathbf{v}_l)_3\right) \\ \frac{d^2 f(\mathbf{v}_l)}{dxz}\left(\left(\overset{\star}{\mathbf{v}}_l\right)_1 - (\mathbf{v}_l)_1\right) + \frac{d^2 f(\mathbf{v}_l)}{dyz}\left(\left(\overset{\star}{\mathbf{v}}_l\right)_2 - (\mathbf{v}_l)_2\right) + \frac{d^2 f(\mathbf{v}_l)}{dz^2}\left(\left(\overset{\star}{\mathbf{v}}_l\right)_3 - (\mathbf{v}_l)_3\right) \end{bmatrix}$$

$$= \nabla\nabla^T f(\mathbf{v}_l)[\overset{\star}{\mathbf{v}}_l - \mathbf{v}_l] \tag{5.43}$$

Substituting this result into Equation 5.42, it simplifies to,

$$\mathbf{0} = \nabla\nabla^T f(\mathbf{v}_l)[\overset{\star}{\mathbf{v}}_l - \mathbf{v}_l] + \nabla\tilde{w}^{r,m,s}(\mathbf{v}_l). \tag{5.44}$$

It follows that,

$$\nabla\nabla^T f(\mathbf{v}_l)[\overset{\star}{\mathbf{v}}_l - \mathbf{v}_l] = -\nabla\tilde{w}^{r,m,s}(\mathbf{v}_l). \tag{5.45}$$

The position estimate error is therefore found using the inverse of the Hessian matrix,

$$[\overset{\star}{\mathbf{v}}_l - \mathbf{v}_l] = -\left(\nabla\nabla^T f(\mathbf{v}_l)\right)^{-1}\nabla\tilde{w}^{r,m,s}(\mathbf{v}_l). \tag{5.46}$$

The probablity distribution of the position estimate error is therefore,

$$[\overset{\star}{\mathbf{v}}_l - \mathbf{v}_l] \sim N\left(\mathbf{0}, \left(\nabla\nabla^T f(\mathbf{v}_l)\right)^{-1}\mathrm{cov}\left(\nabla\tilde{w}^{r,m,s}(\mathbf{v}_l)\right)\left(\left(\nabla\nabla^T f(\mathbf{v}_l)\right)^{-1}\right)^T\right) \tag{5.47}$$

In the following sections derivations for the Hessian of the ideal TART metric and the gradient of the noise term will be presented.

5.6.1 Hessian of Ideal TART metric

Let us consider the first element of the Hessian matrix of the ideal TART metric, $\frac{d^2 f\left(\overset{\#}{\mathbf{v}}_l\right)}{dx^2}$. Taking the derivative of the ideal TART metric near the central peak from Equation 5.10 we obtain

$$\frac{df\left(\overset{\#}{\mathbf{v}}_l\right)}{dx} = -\sum_{p=1}^{P}\sum_{m=1}^{M}\frac{(\boldsymbol{\omega}_c)_m}{c}\sin\left(\frac{(\boldsymbol{\omega}_c)_m}{c}\left(\left\|\mathbf{v}_l-\mathbf{v}_p\right\|-\left\|\overset{\#}{\mathbf{v}}_l-\mathbf{v}_p\right\|\right)\right)\frac{\left(\overset{\#}{\mathbf{v}}_l\right)_1-\left(\mathbf{v}_p\right)_1}{\left\|\overset{\#}{\mathbf{v}}_l-\mathbf{v}_p\right\|}. \tag{5.48}$$

The previous step also involved substitution of ranges for time delays via Equation 2.36.

In order to differentiate a second time we must use the product rule. Let us first compute the derivatives of the two components,

$$\frac{d}{dx}\frac{\left(\overset{\#}{\mathbf{v}}_l\right)_1-\left(\mathbf{v}_p\right)_1}{\left\|\overset{\#}{\mathbf{v}}_l-\mathbf{v}_p\right\|} = \frac{1}{\left\|\overset{\#}{\mathbf{v}}_l-\mathbf{v}_p\right\|}-\frac{\left(\left(\overset{\#}{\mathbf{v}}_l\right)_1-\left(\mathbf{v}_p\right)_1\right)^2}{\left(\left\|\overset{\#}{\mathbf{v}}_l-\mathbf{v}_p\right\|\right)^3} \tag{5.49}$$

$$\begin{aligned}&\frac{d}{dx}\frac{(\boldsymbol{\omega}_c)_m}{c}\sin\left(\frac{(\boldsymbol{\omega}_c)_m}{c}\left(\left\|\mathbf{v}_l-\mathbf{v}_p\right\|-\left\|\overset{\#}{\mathbf{v}}_l-\mathbf{v}_p\right\|\right)\right) = \dots\\ &\frac{\left(\overset{\#}{\mathbf{v}}_l\right)_1-\left(\mathbf{v}_p\right)_1}{\left\|\overset{\#}{\mathbf{v}}_l-\mathbf{v}_p\right\|}\frac{(\boldsymbol{\omega}_c)_m^2}{c^2}\cos\left(\frac{(\boldsymbol{\omega}_c)_m}{c}\left(\left\|\mathbf{v}_l-\mathbf{v}_p\right\|-\left\|\overset{\#}{\mathbf{v}}_l-\mathbf{v}_p\right\|\right)\right).\end{aligned} \tag{5.50}$$

Using these expressions we can now use the product rule to differentiate Equation 5.48,

$$\begin{aligned}\frac{d^2 f\left(\overset{\#}{\mathbf{v}}_l\right)}{dx^2} = &-\sum_{p=1}^{P}\sum_{m=1}^{M}\frac{(\boldsymbol{\omega}_c)_m}{c}\sin\left(\frac{(\boldsymbol{\omega}_c)_m}{c}\left(\left\|\mathbf{v}_l-\mathbf{v}_p\right\|-\left\|\overset{\#}{\mathbf{v}}_l-\mathbf{v}_p\right\|\right)\right)\left(\frac{1}{\left\|\overset{\#}{\mathbf{v}}_l-\mathbf{v}_p\right\|}-\frac{\left(\left(\overset{\#}{\mathbf{v}}_l\right)_1-\left(\mathbf{v}_p\right)_1\right)^2}{\left(\left\|\overset{\#}{\mathbf{v}}_l-\mathbf{v}_p\right\|\right)^3}\right)\dots\\ &+\frac{(\boldsymbol{\omega}_c)_m^2}{c^2}\cos\left(\frac{(\boldsymbol{\omega}_c)_m}{c}\left(\left\|\mathbf{v}_l-\mathbf{v}_p\right\|-\left\|\overset{\#}{\mathbf{v}}_l-\mathbf{v}_p\right\|\right)\right)\frac{\left(\left(\overset{\#}{\mathbf{v}}_l\right)_1-\left(\mathbf{v}_p\right)_1\right)^2}{\left\|\overset{\#}{\mathbf{v}}_l-\mathbf{v}_p\right\|^2}.\end{aligned} \tag{5.51}$$

We are interested in the Hessian evalutated at $\mathbf{v}_l$. For this term we obtain,

$$\frac{d^2 f\left(\mathbf{v}_l\right)}{dx^2} = -\sum_{p=1}^{P}\sum_{m=1}^{M}\left(\frac{(\boldsymbol{\omega}_c)_m}{c}\frac{(\mathbf{v}_l)_1-\left(\mathbf{v}_p\right)_1}{\left\|\mathbf{v}_l-\mathbf{v}_p\right\|}\right)^2. \tag{5.52}$$

Similiarly we can obtain,

$$\frac{d^2 f\left(\mathbf{v}_l\right)}{dy^2} = -\sum_{p=1}^{P}\sum_{m=1}^{M}\left(\frac{(\boldsymbol{\omega}_c)_m}{c}\frac{(\mathbf{v}_l)_2-\left(\mathbf{v}_p\right)_2}{\left\|\mathbf{v}_l-\mathbf{v}_p\right\|}\right)^2, \quad \frac{d^2 f\left(\mathbf{v}_l\right)}{dz^2} = -\sum_{p=1}^{P}\sum_{m=1}^{M}\left(\frac{(\boldsymbol{\omega}_c)_m}{c}\frac{(\mathbf{v}_l)_3-\left(\mathbf{v}_p\right)_3}{\left\|\mathbf{v}_l-\mathbf{v}_p\right\|}\right)^2, \tag{5.53}$$

Next we will consider the off-diagonal terms of the Hessian matrix, starting with $\frac{d^2 f(\mathbf{v}_l)}{dxy}$. We can obtain this by differentiating Equation 5.48 with respect to y. Again we must use the product rule, using the following derivative terms

$$\frac{d}{dy}\frac{\left(\overset{\#}{\mathbf{v}}_l\right)_1 - \left(\mathbf{v}_p\right)_1}{\left\|\overset{\#}{\mathbf{v}}_l - \mathbf{v}_p\right\|} = \frac{\left(\left(\overset{\#}{\mathbf{v}}_l\right)_1 - \left(\mathbf{v}_p\right)_1\right)\left(\left(\overset{\#}{\mathbf{v}}_l\right)_2 - \left(\mathbf{v}_p\right)_2\right)}{\left\|\overset{\#}{\mathbf{v}}_l - \mathbf{v}_p\right\|^3} \tag{5.54}$$

$$\begin{aligned}&\frac{d}{dy}\frac{(\boldsymbol{\omega}_c)_m}{c}\sin\left(\frac{(\boldsymbol{\omega}_c)_m}{c}\left(\left\|\mathbf{v}_l - \mathbf{v}_p\right\| - \left\|\overset{\#}{\mathbf{v}}_l - \mathbf{v}_p\right\|\right)\right) = \dots \\ &\frac{\left(\overset{\#}{\mathbf{v}}_l\right)_2 - \left(\mathbf{v}_p\right)_2}{\left\|\overset{\#}{\mathbf{v}}_l - \mathbf{v}_p\right\|}\frac{(\boldsymbol{\omega}_c)_m^2}{c^2}\cos\left(\frac{(\boldsymbol{\omega}_c)_m}{c}\left(\left\|\mathbf{v}_l - \mathbf{v}_p\right\| - \left\|\overset{\#}{\mathbf{v}}_l - \mathbf{v}_p\right\|\right)\right).\end{aligned} \tag{5.55}$$

Applying the product rule we then obtain,

$$\begin{aligned}\frac{d^2 f\left(\overset{\#}{\mathbf{v}}_l\right)}{dxy} = &-\sum_{p=1}^{P}\sum_{m=1}^{M}\frac{(\boldsymbol{\omega}_c)_m}{c}\sin\left(\frac{(\boldsymbol{\omega}_c)_m}{c}\left(\left\|\mathbf{v}_l - \mathbf{v}_p\right\| - \left\|\overset{\#}{\mathbf{v}}_l - \mathbf{v}_p\right\|\right)\right)\frac{\left(\left(\overset{\#}{\mathbf{v}}_l\right)_1 - \left(\mathbf{v}_p\right)_1\right)\left(\left(\overset{\#}{\mathbf{v}}_l\right)_2 - \left(\mathbf{v}_p\right)_2\right)}{\left\|\overset{\#}{\mathbf{v}}_l - \mathbf{v}_p\right\|^3}\dots \\ &+\frac{(\boldsymbol{\omega}_c)_m^2}{c^2}\cos\left(\frac{(\boldsymbol{\omega}_c)_m}{c}\left(\left\|\mathbf{v}_l - \mathbf{v}_p\right\| - \left\|\overset{\#}{\mathbf{v}}_l - \mathbf{v}_p\right\|\right)\right)\frac{\left(\left(\overset{\#}{\mathbf{v}}_l\right)_1 - \left(\mathbf{v}_p\right)_1\right)\left(\left(\overset{\#}{\mathbf{v}}_l\right)_2 - \left(\mathbf{v}_p\right)_2\right)}{\left\|\overset{\#}{\mathbf{v}}_l - \mathbf{v}_p\right\|^2}.\end{aligned} \tag{5.56}$$

Evaluating at $\mathbf{v}_l$ we obtain,

$$\frac{d^2 f\left(\mathbf{v}_l\right)}{dxy} = -\sum_{p=1}^{P}\sum_{m=1}^{M}\frac{(\boldsymbol{\omega}_c)_m^2}{c^2}\frac{\left((\mathbf{v}_l)_1 - \left(\mathbf{v}_p\right)_1\right)\left((\mathbf{v}_l)_2 - \left(\mathbf{v}_p\right)_2\right)}{\left\|\mathbf{v}_l - \mathbf{v}_p\right\|^2}. \tag{5.57}$$

Similarly we obtain,

$$\frac{d^2 f\left(\mathbf{v}_l\right)}{dxz} = -\sum_{p=1}^{P}\sum_{m=1}^{M}\frac{(\boldsymbol{\omega}_c)_m^2}{c^2}\frac{\left((\mathbf{v}_l)_1 - \left(\mathbf{v}_p\right)_1\right)\left((\mathbf{v}_l)_3 - \left(\mathbf{v}_p\right)_3\right)}{\left\|\mathbf{v}_l - \mathbf{v}_p\right\|^2}, \tag{5.58}$$

$$\frac{d^2 f\left(\mathbf{v}_l\right)}{dyz} = -\sum_{p=1}^{P}\sum_{m=1}^{M}\frac{(\boldsymbol{\omega}_c)_m^2}{c^2}\frac{\left((\mathbf{v}_l)_2 - \left(\mathbf{v}_p\right)_2\right)\left((\mathbf{v}_l)_3 - \left(\mathbf{v}_p\right)_3\right)}{\left\|\mathbf{v}_l - \mathbf{v}_p\right\|^2}. \tag{5.59}$$

The full Hessian matrix can be populated as,

$$\begin{aligned}\nabla\nabla^T f\left(\mathbf{v}_l\right) &= -\sum_{p=1}^{P}\frac{[\mathbf{v}_l - \mathbf{v}_p][\mathbf{v}_l - \mathbf{v}_p]^T}{c^2\left\|\mathbf{v}_l - \mathbf{v}_p\right\|^2}\sum_{m=1}^{M}(\boldsymbol{\omega}_c)_m^2 \\ &= -\frac{\|\boldsymbol{\omega}_c\|^2}{c^2}\sum_{p=1}^{P}\frac{[\mathbf{v}_l - \mathbf{v}_p][\mathbf{v}_l - \mathbf{v}_p]^T}{\left\|\mathbf{v}_l - \mathbf{v}_p\right\|^2}\end{aligned} \tag{5.60}$$

5.6.2 Gradient of Noise Term

Now let us consider the gradient of the noise term. Since we have an additive noise model where our metric is the sum of an ideal component and a noise term, the gradient of the metric must be the sum of the gradient of the ideal term and the gradient of the noise term because the gradient is a linear operation. Let us define the unit vectors associated with the x, y and z axes of the solution space,

$$\hat{\mathbf{i}} = \begin{bmatrix} 1 \\ 0 \\ 0 \end{bmatrix}, \quad \hat{\mathbf{j}} = \begin{bmatrix} 0 \\ 1 \\ 0 \end{bmatrix} \quad \text{and} \quad \hat{\mathbf{k}} = \begin{bmatrix} 0 \\ 0 \\ 1 \end{bmatrix}. \tag{5.61}$$

First we will consider the first element of the gradient vector, which is the derivative with respect to x; that is, in the $\hat{\mathbf{i}}$ direction. The derivative of the noise term can be defined as the limit of the finite difference approximation,

$$\frac{d}{dx}\tilde{w}^{r,m,s}\left(\overset{\#}{\mathbf{v}}_l\right) = \lim_{\epsilon \to 0} \frac{\tilde{w}^{r,m,s}\left(\overset{\#}{\mathbf{v}}_l + \hat{\mathbf{i}}\epsilon\right) - \tilde{w}^{r,m,s}\left(\overset{\#}{\mathbf{v}}_l\right)}{\epsilon}. \tag{5.62}$$

This can equivalently be expressed as,

$$\frac{d}{dx}\tilde{w}^{r,m,s}\left(\overset{\#}{\mathbf{v}}_l\right) = \lim_{\epsilon \to 0} \frac{1}{\epsilon} \begin{bmatrix} -1 & 1 \end{bmatrix} \begin{bmatrix} \tilde{w}^{r,m,s}\left(\overset{\#}{\mathbf{v}}_l\right) \\ \tilde{w}^{r,m,s}\left(\overset{\#}{\mathbf{v}}_l + \hat{\mathbf{i}}\epsilon\right) \end{bmatrix} \tag{5.63}$$

From the Equation 5.39 it is known that,

$$\begin{bmatrix} \tilde{w}^{r,m,s}\left(\overset{\#}{\mathbf{v}}_l\right) \\ \tilde{w}^{r,m,s}\left(\overset{\#}{\mathbf{v}}_l + \hat{\mathbf{i}}\epsilon\right) \end{bmatrix} \sim \dots$$

$$N\left(\mathbf{0}, \frac{\sigma^2}{2}\sum_{p=1}^{P}\begin{bmatrix} M & \sum_{m=1}^{M}\cos\left((\boldsymbol{\omega}_c)_m\left(\overset{\#}{t}_{0,p}\left(\overset{\#}{\mathbf{v}}_l\right) - \overset{\#}{t}_{0,p}\left(\overset{\#}{\mathbf{v}}_l + \hat{\mathbf{i}}\epsilon\right)\right)\right) \\ \sum_{m=1}^{M}\cos\left((\boldsymbol{\omega}_c)_m\left(\overset{\#}{t}_{0,p}\left(\overset{\#}{\mathbf{v}}_l\right) - \overset{\#}{t}_{0,p}\left(\overset{\#}{\mathbf{v}}_l + \hat{\mathbf{i}}\epsilon\right)\right)\right) & M \end{bmatrix}\right). \tag{5.64}$$

Since we have another multivariate normal distribution undergoing a linear transformation we have,

$$\frac{d}{dx}\tilde{w}^{r,m,s}\left(\overset{\#}{\mathbf{v}}_l\right) \sim N\Bigg(0, \frac{1}{\epsilon^2}\begin{bmatrix} -1 & 1 \end{bmatrix}\dots$$
$$\frac{\sigma^2}{2}\sum_{p=1}^{P}\begin{bmatrix} M & \sum_{m=1}^{M}\cos\left((\boldsymbol{\omega}_c)_m\left(\overset{\#}{t}_{0,p}\left(\overset{\#}{\mathbf{v}}_l\right) - \overset{\#}{t}_{0,p}\left(\overset{\#}{\mathbf{v}}_l + \hat{\mathbf{i}}\epsilon\right)\right)\right) \\ \sum_{m=1}^{M}\cos\left((\boldsymbol{\omega}_c)_m\left(\overset{\#}{t}_{0,p}\left(\overset{\#}{\mathbf{v}}_l\right) - \overset{\#}{t}_{0,p}\left(\overset{\#}{\mathbf{v}}_l + \hat{\mathbf{i}}\epsilon\right)\right)\right) & M \end{bmatrix}\begin{bmatrix} -1 \\ 1 \end{bmatrix}\Bigg)$$
$$\frac{d}{dx}\tilde{w}^{r,m,s}\left(\overset{\#}{\mathbf{v}}_l\right) \sim N\left(0, \lim_{\epsilon\to 0}\frac{\sigma^2}{\epsilon^2}\left(PM - \sum_{p=1}^{P}\sum_{m=1}^{M}\cos\left((\boldsymbol{\omega}_c)_m\left(\overset{\#}{t}_{0,p}\left(\overset{\#}{\mathbf{v}}_l\right) - \overset{\#}{t}_{0,p}\left(\overset{\#}{\mathbf{v}}_l + \hat{\mathbf{i}}\epsilon\right)\right)\right)\right)\right). \tag{5.65}$$

Substituting ranges for time delays we have,

$$\frac{d}{dx}\tilde{w}^{r,m,s}\left(\overset{\#}{\mathbf{v}}_l\right) \sim N\left(0, \lim_{\epsilon\to 0}\frac{\sigma^2}{\epsilon^2}\left(PM - \sum_{p=1}^{P}\sum_{m=1}^{M}\cos\left(\frac{(\boldsymbol{\omega}_c)_m}{c}\left(\left\|\overset{\#}{\mathbf{v}}_l + \hat{\mathbf{i}}\epsilon - \mathbf{v}_p\right\| - \left\|\overset{\#}{\mathbf{v}}_l - \mathbf{v}_p\right\|\right)\right)\right)\right). \tag{5.66}$$

In this case we have the limit of a fraction. The limit of the denominator, ϵ^2, clearly is zero as ϵ approaches zero. The numerator of this expression also has a limit of zero, as the argument of the cosine terms become zero, which when summed cancel with the PM term. This implies that we need to use l'Hôpital's rule to find the limit of the expression. Applying this yields,

$$\frac{d}{dx}\tilde{w}^{r,m,s}\left(\overset{\#}{\mathbf{v}}_l\right) \sim N\left(0, \lim_{\epsilon\to 0}\frac{1}{2\epsilon}\frac{d}{d\epsilon}\sigma^2\left(PM - \sum_{p=1}^{P}\sum_{m=1}^{M}\cos\left(\frac{(\boldsymbol{\omega}_c)_m}{c}\left(\left\|\overset{\#}{\mathbf{v}}_l + \hat{\mathbf{i}}\epsilon - \mathbf{v}_p\right\| - \left\|\overset{\#}{\mathbf{v}}_l - \mathbf{v}_p\right\|\right)\right)\right)\right). \tag{5.67}$$

Differentiating we obtain,

$$\frac{d}{dx}\tilde{w}^{r,m,s}\left(\overset{\#}{\mathbf{v}}_l\right) \sim \dots$$
$$N\left(0, \lim_{\epsilon\to 0}\frac{1}{2\epsilon}\frac{\sigma^2}{c}\sum_{p=1}^{P}\frac{\left(\overset{\#}{\mathbf{v}}_l\right)_1 + \epsilon - \left(\mathbf{v}_p\right)_1}{\left\|\overset{\#}{\mathbf{v}}_l + \hat{\mathbf{i}}\epsilon - \mathbf{v}_p\right\|}\sum_{m=1}^{M}(\boldsymbol{\omega}_c)_m\sin\left(\frac{(\boldsymbol{\omega})_m}{c}\left(\left\|\overset{\#}{\mathbf{v}}_l + \hat{\mathbf{i}}\epsilon - \mathbf{v}_p\right\| - \left\|\overset{\#}{\mathbf{v}}_l - \mathbf{v}_p\right\|\right)\right)\right). \tag{5.68}$$

We again have the limit of a fraction where both the numerator and denominator have a limit of zero. The limit of the numerator is clearly zero because each of the sine terms approach zero as epsilon approaches zero. We need to apply l'Hôpital's rule a second time,

$$\frac{d}{dx}\tilde{w}^{r,m,s}\left(\overset{\#}{\mathbf{v}}_l\right) \sim \dots$$
$$N\left(0, \lim_{\epsilon\to 0}\frac{d}{d\epsilon}\frac{\sigma^2}{2c}\sum_{p=1}^{P}\frac{\left(\overset{\#}{\mathbf{v}}_l\right)_1 + \epsilon - \left(\mathbf{v}_p\right)_1}{\left\|\overset{\#}{\mathbf{v}}_l + \hat{\mathbf{i}}\epsilon - \mathbf{v}_p\right\|}\sum_{m=1}^{M}(\boldsymbol{\omega}_c)_m\sin\left(\frac{(\boldsymbol{\omega})_m}{c}\left(\left\|\overset{\#}{\mathbf{v}}_l + \hat{\mathbf{i}}\epsilon - \mathbf{v}_p\right\| - \left\|\overset{\#}{\mathbf{v}}_l - \mathbf{v}_p\right\|\right)\right)\right). \tag{5.69}$$

To take the remaining derivative the product rule is required. Let us first compute the derivatives of the two components.

$$\frac{d}{d\epsilon}\frac{\left(\overset{\#}{\mathbf{v}}_l\right)_1 + \epsilon - \left(\mathbf{v}_p\right)_1}{\left\|\overset{\#}{\mathbf{v}}_l + \hat{\mathbf{i}}\epsilon - \mathbf{v}_p\right\|} = \frac{1}{\left\|\overset{\#}{\mathbf{v}}_l + \hat{\mathbf{i}}\epsilon - \mathbf{v}_p\right\|} - \frac{\left(\left(\overset{\#}{\mathbf{v}}_l\right)_1 + \epsilon - \left(\mathbf{v}_p\right)_1\right)^2}{\left(\left\|\overset{\#}{\mathbf{v}}_l + \hat{\mathbf{i}}\epsilon - \mathbf{v}_p\right\|\right)^3} \tag{5.70}$$

$$\begin{aligned}&\frac{d}{d\epsilon}\sum_{m=1}^{M}(\boldsymbol{\omega}_c)_m \sin\left(\frac{(\boldsymbol{\omega}_c)_m}{c}\left(\left\|\overset{\#}{\mathbf{v}}_l + \hat{\mathbf{i}}\epsilon - \mathbf{v}_p\right\| - \left\|\overset{\#}{\mathbf{v}}_l - \mathbf{v}_p\right\|\right)\right) = \dots \\ &\frac{\left(\overset{\#}{\mathbf{v}}_l\right)_1 + \epsilon - \left(\mathbf{v}_p\right)_1}{\left\|\overset{\#}{\mathbf{v}}_l + \hat{\mathbf{i}}\epsilon - \mathbf{v}_p\right\|}\sum_{m=1}^{M}\frac{(\boldsymbol{\omega}_c)_m^2}{c}\cos\left(\frac{(\boldsymbol{\omega}_c)_m}{c}\left(\left\|\overset{\#}{\mathbf{v}}_l + \hat{\mathbf{i}}\epsilon - \mathbf{v}_p\right\| - \left\|\overset{\#}{\mathbf{v}}_l - \mathbf{v}_p\right\|\right)\right)\end{aligned} \tag{5.71}$$

We can use these to take the derivative in Equation 5.69,

$$\begin{aligned}&\frac{d}{d\epsilon}\sum_{p=1}^{P}\frac{\sigma^2}{2c}\frac{\left(\overset{\#}{\mathbf{v}}_l\right)_1 + \epsilon - \left(\mathbf{v}_p\right)_1}{\left\|\overset{\#}{\mathbf{v}}_l + \hat{\mathbf{i}}\epsilon - \mathbf{v}_p\right\|}\sum_{m=1}^{M}(\boldsymbol{\omega}_c)_m \sin\left(\frac{(\boldsymbol{\omega}_c)_m}{c}\left(\left\|\overset{\#}{\mathbf{v}}_l + \hat{\mathbf{i}}\epsilon - \mathbf{v}_p\right\| - \left\|\overset{\#}{\mathbf{v}}_l - \mathbf{v}_p\right\|\right)\right) = \dots \\ &\sum_{p=1}^{P}\frac{\sigma^2}{2c}\left(\frac{1}{\left\|\overset{\#}{\mathbf{v}}_l + \hat{\mathbf{i}}\epsilon - \mathbf{v}_p\right\|} - \frac{\left(\left(\overset{\#}{\mathbf{v}}_l\right)_1 + \epsilon - \left(\mathbf{v}_p\right)_1\right)^2}{\left(\left\|\overset{\#}{\mathbf{v}}_l + \hat{\mathbf{i}}\epsilon - \mathbf{v}_p\right\|\right)^3}\right)\sum_{m=1}^{M}(\boldsymbol{\omega}_c)_m \sin\left(\frac{(\boldsymbol{\omega}_c)_m}{c}\left(\left\|\overset{\#}{\mathbf{v}}_l + \hat{\mathbf{i}}\epsilon - \mathbf{v}_p\right\| - \left\|\overset{\#}{\mathbf{v}}_l - \mathbf{v}_p\right\|\right)\right) + \dots \\ &\sum_{p=1}^{P}\frac{\sigma^2}{2c^2}\left(\frac{\left(\overset{\#}{\mathbf{v}}_l\right)_1 + \epsilon - \left(\mathbf{v}_p\right)_1}{\left\|\overset{\#}{\mathbf{v}}_l + \hat{\mathbf{i}}\epsilon - \mathbf{v}_p\right\|}\right)^2\sum_{m=1}^{M}(\boldsymbol{\omega}_c)_m^2 \cos\left(\frac{(\boldsymbol{\omega}_c)_m}{c}\left(\left\|\overset{\#}{\mathbf{v}}_l + \hat{\mathbf{i}}\epsilon - \mathbf{v}_p\right\| - \left\|\overset{\#}{\mathbf{v}}_l - \mathbf{v}_p\right\|\right)\right)\end{aligned} \tag{5.72}$$

Taking the limit of this expression as ϵ goes to zero yields,

$$\frac{d}{dx}\tilde{w}^{r,m,s}\left(\overset{\#}{\mathbf{v}}_l\right) \sim N\left(0, \frac{\sigma^2}{2c^2}\sum_{p=1}^{P}\left(\frac{\left(\overset{\#}{\mathbf{v}}_l\right)_1 - \left(\mathbf{v}_p\right)_1}{\left\|\overset{\#}{\mathbf{v}}_l - \mathbf{v}_p\right\|}\right)^2\sum_{m=1}^{M}(\boldsymbol{\omega}_c)_m^2\right), \tag{5.73}$$

which further simplifies to

$$\frac{d}{dx}\tilde{w}^{r,m,s}\left(\overset{\#}{\mathbf{v}}_l\right) \sim N\left(0, \sum_{p=1}^{P}\left(\frac{\sigma\|\boldsymbol{\omega}_c\|}{\sqrt{2}c}\frac{\left(\overset{\#}{\mathbf{v}}_l\right)_1 - \left(\mathbf{v}_p\right)_1}{\left\|\overset{\#}{\mathbf{v}}_l - \mathbf{v}_p\right\|}\right)^2\right). \tag{5.74}$$

In the same manner we can obtain,

$$\frac{d}{dy}\tilde{w}^{r,m,s}\left(\overset{\#}{\mathbf{v}}_l\right) \sim N\left(0, \sum_{p=1}^{P}\left(\frac{\sigma\|\boldsymbol{\omega}_c\|}{\sqrt{2}c}\frac{\left(\overset{\#}{\mathbf{v}}_l\right)_2 - \left(\mathbf{v}_p\right)_2}{\left\|\overset{\#}{\mathbf{v}}_l - \mathbf{v}_p\right\|}\right)^2\right), \tag{5.75}$$

$$\frac{d}{dz}\tilde{w}^{r,m,s}\left(\overset{\#}{\mathbf{v}}_l\right) \sim N\left(0, \sum_{p=1}^{P}\left(\frac{\sigma\|\boldsymbol{\omega}_c\|}{\sqrt{2}c}\frac{\left(\overset{\#}{\mathbf{v}}_l\right)_3 - \left(\mathbf{v}_p\right)_3}{\left\|\overset{\#}{\mathbf{v}}_l - \mathbf{v}_p\right\|}\right)^2\right). \tag{5.76}$$

Next we will consider the covariance first two elements of the gradient vector, which can be expressed as

$$\begin{bmatrix} \frac{d}{dx}\tilde{w}^{r,m,s}\left(\overset{\#}{\mathbf{v}}_l\right) \\ \frac{d}{dy}\tilde{w}^{r,m,s}\left(\overset{\#}{\mathbf{v}}_l\right) \end{bmatrix} = \lim_{\epsilon\to 0}\begin{bmatrix} -\frac{1}{\epsilon} & \frac{1}{\epsilon} & 0 \\ -\frac{1}{\epsilon} & 0 & \frac{1}{\epsilon} \end{bmatrix}\begin{bmatrix} \tilde{w}^{r,m,s}\left(\overset{\#}{\mathbf{v}}_l\right) \\ \tilde{w}^{r,m,s}\left(\overset{\#}{\mathbf{v}}_l + \hat{\mathbf{i}}\epsilon\right) \\ \tilde{w}^{r,m,s}\left(\overset{\#}{\mathbf{v}}_l + \hat{\mathbf{j}}\epsilon\right) \end{bmatrix} \tag{5.77}$$

As this represents another multivariate normal random vector undergoing a linear transformation we can obtain

$$\begin{aligned}\operatorname{cov}\left(\frac{d}{dx}\tilde{w}^{r,m,s}\left(\overset{\#}{\mathbf{v}}_l\right), \frac{d}{dy}\tilde{w}^{r,m,s}\left(\overset{\#}{\mathbf{v}}_l\right)\right) = \lim_{\epsilon\to 0}\frac{\sigma^2}{2\epsilon^2}\sum_{p=1}^{P}\sum_{m=1}^{M}\left(1 - \cos\left((\boldsymbol{\omega}_c)_m\left(\overset{\#}{t}_{0,p}\left(\overset{\#}{\mathbf{v}}_l\right) - \overset{\#}{t}_{0,p}\left(\overset{\#}{\mathbf{v}}_l + \hat{\mathbf{i}}\epsilon\right)\right)\right)\right)\dots \\ - \cos\left((\boldsymbol{\omega}_c)_m\left(\overset{\#}{t}_{0,p}\left(\overset{\#}{\mathbf{v}}_l\right) - \overset{\#}{t}_{0,p}\left(\overset{\#}{\mathbf{v}}_l + \hat{\mathbf{j}}\epsilon\right)\right)\right) + \cos\left((\boldsymbol{\omega}_c)_m\left(\overset{\#}{t}_{0,p}\left(\overset{\#}{\mathbf{v}}_l + \hat{\mathbf{i}}\epsilon\right) - \overset{\#}{t}_{0,p}\left(\overset{\#}{\mathbf{v}}_l + \hat{\mathbf{j}}\epsilon\right)\right)\right)\Bigg)\end{aligned} \tag{5.78}$$

We must again apply l'Hôpital's rule twice in order do determine the limit.

$$\begin{aligned}\operatorname{cov}\left(\frac{d}{dx}\tilde{w}^{r,m,s}\left(\overset{\#}{\mathbf{v}}_l\right), \frac{d}{dy}\tilde{w}^{r,m,s}\left(\overset{\#}{\mathbf{v}}_l\right)\right) = \lim_{\epsilon\to 0}\frac{\sigma^2}{4}\frac{d^2}{d\epsilon^2}\sum_{p=1}^{P}\sum_{m=1}^{M}\left(1 - \cos\left((\boldsymbol{\omega}_c)_m\left(\overset{\#}{t}_{0,p}\left(\overset{\#}{\mathbf{v}}_l\right) - \overset{\#}{t}_{0,p}\left(\overset{\#}{\mathbf{v}}_l + \hat{\mathbf{i}}\epsilon\right)\right)\right)\right)\dots \\ - \cos\left((\boldsymbol{\omega}_c)_m\left(\overset{\#}{t}_{0,p}\left(\overset{\#}{\mathbf{v}}_l\right) - \overset{\#}{t}_{0,p}\left(\overset{\#}{\mathbf{v}}_l + \hat{\mathbf{j}}\epsilon\right)\right)\right) + \cos\left((\boldsymbol{\omega}_c)_m\left(\overset{\#}{t}_{0,p}\left(\overset{\#}{\mathbf{v}}_l + \hat{\mathbf{i}}\epsilon\right) - \overset{\#}{t}_{0,p}\left(\overset{\#}{\mathbf{v}}_l + \hat{\mathbf{j}}\epsilon\right)\right)\right)\Bigg)\end{aligned} \tag{5.79}$$

Distributing we obtain,

$$\begin{aligned}\operatorname{cov}\left(\frac{d}{dx}\tilde{w}^{r,m,s}\left(\overset{\#}{\mathbf{v}}_l\right), \frac{d}{dy}\tilde{w}^{r,m,s}\left(\overset{\#}{\mathbf{v}}_l\right)\right) = \lim_{\epsilon\to 0}\frac{d^2}{d\epsilon^2}\frac{\sigma^2}{4}MP\dots \\ - \frac{d^2}{d\epsilon^2}\frac{\sigma^2}{4}\sum_{p=1}^{P}\sum_{m=1}^{M}\cos\left((\boldsymbol{\omega}_c)_m\left(\overset{\#}{t}_{0,p}\left(\overset{\#}{\mathbf{v}}_l\right) - \overset{\#}{t}_{0,p}\left(\overset{\#}{\mathbf{v}}_l + \hat{\mathbf{i}}\epsilon\right)\right)\right)\dots \\ - \frac{d^2}{d\epsilon^2}\frac{\sigma^2}{4}\sum_{p=1}^{P}\sum_{m=1}^{M}\cos\left((\boldsymbol{\omega}_c)_m\left(\overset{\#}{t}_{0,p}\left(\overset{\#}{\mathbf{v}}_l\right) - \overset{\#}{t}_{0,p}\left(\overset{\#}{\mathbf{v}}_l + \hat{\mathbf{j}}\epsilon\right)\right)\right)\dots \\ + \frac{d^2}{d\epsilon^2}\frac{\sigma^2}{4}\sum_{p=1}^{P}\sum_{m=1}^{M}\cos\left((\boldsymbol{\omega}_c)_m\left(\overset{\#}{t}_{0,p}\left(\overset{\#}{\mathbf{v}}_l + \hat{\mathbf{i}}\epsilon\right) - \overset{\#}{t}_{0,p}\left(\overset{\#}{\mathbf{v}}_l + \hat{\mathbf{j}}\epsilon\right)\right)\right)\end{aligned} \tag{5.80}$$

Let us consider each of these four second derivative terms individually. The first term involves differentiating a constant, and so reduces to zero. The second term is identical to that which we

differentiated twice previously, starting with Equation 5.65. Therefore we know that,

$$\lim_{\epsilon\to 0} -\frac{d^2}{d\epsilon^2}\frac{\sigma^2}{4}\sum_{p=1}^{P}\sum_{m=1}^{M}\cos\left((\boldsymbol{\omega}_c)_m\left(\overset{\#}{t}_{0,p}\left(\overset{\#}{\mathbf{v}}_l\right)-\overset{\#}{t}_{0,p}\left(\overset{\#}{\mathbf{v}}_l+\hat{\mathbf{i}}\epsilon\right)\right)\right)=\sum_{p=1}^{P}\left(\frac{\sigma\|\boldsymbol{\omega}_c\|}{\sqrt{4}c}\frac{\left(\overset{\#}{\mathbf{v}}_l\right)_1-\left(\mathbf{v}_p\right)_1}{\left\|\overset{\#}{\mathbf{v}}_l-\mathbf{v}_p\right\|}\right)^2 \tag{5.81}$$

Similarly we know that,

$$\lim_{\epsilon\to 0} -\frac{d^2}{d\epsilon^2}\frac{\sigma^2}{4}\sum_{p=1}^{P}\sum_{m=1}^{M}\cos\left((\boldsymbol{\omega}_c)_m\left(\overset{\#}{t}_{0,p}\left(\overset{\#}{\mathbf{v}}_l\right)-\overset{\#}{t}_{0,p}\left(\overset{\#}{\mathbf{v}}_l+\hat{\mathbf{j}}\epsilon\right)\right)\right)=\sum_{p=1}^{P}\left(\frac{\sigma\|\boldsymbol{\omega}_c\|}{\sqrt{4}c}\frac{\left(\overset{\#}{\mathbf{v}}_l\right)_2-\left(\mathbf{v}_p\right)_2}{\left\|\overset{\#}{\mathbf{v}}_l-\mathbf{v}_p\right\|}\right)^2 \tag{5.82}$$

The final second derivative term must be examined more closely; via a similar procedure to the derivation of the distribution of $\frac{d}{dx}\tilde{w}^{r,m,s}\left(\overset{\#}{\mathbf{v}}_l\right)$ we can obtain,

$$\begin{aligned}\lim_{\epsilon\to 0}\frac{d^2}{d\epsilon^2}\frac{\sigma^2}{4}\sum_{p=1}^{P}\sum_{m=1}^{M}\cos\left((\boldsymbol{\omega}_c)_m\left(\overset{\#}{t}_{0,p}\left(\overset{\#}{\mathbf{v}}_l+\hat{\mathbf{i}}\epsilon\right)-\overset{\#}{t}_{0,p}\left(\overset{\#}{\mathbf{v}}_l+\hat{\mathbf{j}}\epsilon\right)\right)\right)=\ldots\\ -\sum_{p=1}^{P}\left(\frac{\sigma\|\boldsymbol{\omega}_c\|}{\sqrt{4}c}\frac{\left(\overset{\#}{\mathbf{v}}_l\right)_1-\left(\mathbf{v}_p\right)_1-\left(\overset{\#}{\mathbf{v}}_l\right)_2+\left(\mathbf{v}_p\right)_2}{\left\|\overset{\#}{\mathbf{v}}_l-\mathbf{v}_p\right\|}\right)^2\end{aligned} \tag{5.83}$$

Combining these terms we obtain,

$$\begin{aligned}\operatorname{cov}\left(\frac{d}{dx}\tilde{w}^{r,m,s}\left(\overset{\#}{\mathbf{v}}_l\right),\frac{d}{dy}\tilde{w}^{r,m,s}\left(\overset{\#}{\mathbf{v}}_l\right)\right)&=\left(\frac{\sigma\|\boldsymbol{\omega}_c\|}{\sqrt{4}c}\right)^2\sum_{p=1}^{P}\left(\frac{\left(\overset{\#}{\mathbf{v}}_l\right)_1-\left(\mathbf{v}_p\right)_1}{\left\|\overset{\#}{\mathbf{v}}_l-\mathbf{v}_p\right\|}\right)^2+\ldots\\ &\left(\frac{\left(\overset{\#}{\mathbf{v}}_l\right)_2-\left(\mathbf{v}_p\right)_2}{\left\|\overset{\#}{\mathbf{v}}_l-\mathbf{v}_p\right\|}\right)^2-\left(\frac{\left(\overset{\#}{\mathbf{v}}_l\right)_1-\left(\mathbf{v}_p\right)_1-\left(\overset{\#}{\mathbf{v}}_l\right)_2+\left(\mathbf{v}_p\right)_2}{\left\|\overset{\#}{\mathbf{v}}_l-\mathbf{v}_p\right\|}\right)^2\\ &=\left(\frac{\sigma\|\boldsymbol{\omega}_c\|}{\sqrt{2}c}\right)^2\sum_{p=1}^{P}\frac{\left(\left(\overset{\#}{\mathbf{v}}_l\right)_1-\left(\mathbf{v}_p\right)_1\right)\left(\left(\overset{\#}{\mathbf{v}}_l\right)_2-\left(\mathbf{v}_p\right)_2\right)}{\left\|\overset{\#}{\mathbf{v}}_l-\mathbf{v}_p\right\|^2}\end{aligned} \tag{5.84}$$

The other covariance terms can be found in the same manner. The distribution of the gradient of the noise term can now be fully represented as,

$$\nabla\tilde{w}^{r,m,s}\sim N\left(\mathbf{0},\left(\frac{\sigma\|\boldsymbol{\omega}_c\|}{\sqrt{2}c}\right)^2\sum_{p=1}^{P}\frac{\left[\overset{\#}{\mathbf{v}}_l-\mathbf{v}_p\right]\left[\overset{\#}{\mathbf{v}}_l-\mathbf{v}_p\right]^T}{\left\|\overset{\#}{\mathbf{v}}_l-\mathbf{v}_p\right\|^2}\right). \tag{5.85}$$

5.7 Position Estimate Error

Recall Equation 5.47 which described the probability distribution of the TART position estimate error. Now that we have computed the Hessian of the ideal TART metric and the gradient of the noise term, we can use them to evaluate this equation. First however, we must note the similarity between our expression for the Hessian matrix of the ideal TART metric at the true location and the covariance of the gradient of the noise term. Indeed the relation is as simple as

$$\operatorname{cov}\left(\nabla\tilde{w}^{r,m,s}\left(\mathbf{v}_l\right)\right) = \frac{-\sigma^2}{2}\nabla\nabla^T f\left(\mathbf{v}_l\right). \tag{5.86}$$

We can use this relation to simplify Equation 5.47,

$$\begin{aligned}\left[\overset{\star}{\mathbf{v}}_l - \mathbf{v}_l\right] &\sim N\left(\mathbf{0}, \left(\nabla\nabla^T f\left(\mathbf{v}_l\right)\right)^{-1} \frac{-\sigma^2}{2}\nabla\nabla^T f\left(\mathbf{v}_l\right)\left(\left(\nabla\nabla^T f\left(\mathbf{v}_l\right)\right)^{-1}\right)^T\right) \\ &\sim N\left(\mathbf{0}, \frac{-\sigma^2}{2}\left(\left(\nabla\nabla^T f\left(\mathbf{v}_l\right)\right)^T\right)^{-1}\right) \\ &\sim N\left(\mathbf{0}, \frac{\sigma^2 c^2}{2\|\boldsymbol{\omega}_c\|^2}\left(\sum_{p=1}^{P}\frac{[\mathbf{v}_l - \mathbf{v}_p][\mathbf{v}_l - \mathbf{v}_p]^T}{\left\|\mathbf{v}_l - \mathbf{v}_p\right\|^2}\right)^{-1}\right)\end{aligned} \tag{5.87}$$

We now have an expression for the distribution of position estimate errors. We see that it is unbiased (has zero mean). The covariance matrix is a function of several parameters. The variance of the errors is linearly proportional to σ^2, the variance of the original noise added to the received signal. We also see the variance of the errors is inversely proportional to $\|\boldsymbol{\omega}_c\|^2$, which implies that having more bandwidth will reduce the size of the errors. We also see that the covariance matrix is affected by the geometry of the system, as the matrix inverse term depends on the mobile transceiver location $\mathbf{v}_l$ and reference transceiver locations, $\mathbf{v}_p$.

As with any expression containing the inverse of a matrix, we must concern ourselves with the conditions under which the matrix is singular and can not be inverted. For example, if $P = 1$ the matrix to be inverted is simply the outer product of a vector with itself, which has rank 1 and can not be inverted. This makes sense because with a single reference unit one can not perform three-dimensional location as the problem is underdetermined. This is reflected by the singularity of the matrix to be inverted. Only by summing the outer product terms from several reference antennas with diverse geometry do we obtain a valid expression for the three-dimensional error covariance.

Suppose we construct a matrix $\mathbf{V}$ where each column is the unit vector in the direction from a

reference antenna to the mobile antenna,

$$\mathbf{V} = \begin{bmatrix} \frac{\mathbf{v}_l - \mathbf{v}_1}{\|\mathbf{v}_l - \mathbf{v}_1\|^2} & \cdots & \frac{\mathbf{v}_l - \mathbf{v}_p}{\|\mathbf{v}_l - \mathbf{v}_p\|^2} & \cdots & \frac{\mathbf{v}_l - \mathbf{v}_P}{\|\mathbf{v}_l - \mathbf{v}_P\|^2} \end{bmatrix}. \tag{5.88}$$

Equation 5.87 can be rewritten as,

$$\left[\overset{\star}{\mathbf{v}}_l - \mathbf{v}_l\right] \sim N\left(\mathbf{0}, \frac{\sigma^2 c^2}{2\|\boldsymbol{\omega}_c\|^2} \left(\mathbf{V}\mathbf{V}^T\right)^{-1}\right) \tag{5.89}$$

It is known that rank($\mathbf{V}$) = rank($\mathbf{V}\mathbf{V}^T$) [31], therefore in order for the inverse in this expression to exist the rank of $\mathbf{V}$ must be three (in the three-dimensional case). This implies for example our perturbation approximation is invalid for certain degenerate geometry cases, as for the example the case of all antennas being coplanar. For reasonably chosen geometries of interest, it is expected that this will not be the case.

Let us also note that while this derivation has been carried out for the three-dimensional case, we can easily reduce it to analyze two-dimensional cases, even for geometries that would be considered degenerate in the three-dimensional case.

We also are interested the root mean square (RMS) error of the distance between the true position and the estimate,

$$\left\|\overset{\star}{\mathbf{v}}_l - \mathbf{v}_l\right\| = \sqrt{\left(\overset{\star}{\mathbf{v}}_l - \mathbf{v}_l\right)_1^2 + \left(\overset{\star}{\mathbf{v}}_l - \mathbf{v}_l\right)_2^2 + \left(\overset{\star}{\mathbf{v}}_l - \mathbf{v}_l\right)_3^2}. \tag{5.90}$$

The RMS error is defined as,

$$\mathrm{rms}\left(\left\|\overset{\star}{\mathbf{v}}_l - \mathbf{v}_l\right\|\right) = \sqrt{E\left\{\left\|\overset{\star}{\mathbf{v}}_l - \mathbf{v}_l\right\|^2\right\}}. \tag{5.91}$$

This can be rewritten as,

$$\mathrm{rms}\left(\left\|\overset{\star}{\mathbf{v}}_l - \mathbf{v}_l\right\|\right) = \sqrt{E\left\{\left(\overset{\star}{\mathbf{v}}_l - \mathbf{v}_l\right)_1^2 + \left(\overset{\star}{\mathbf{v}}_l - \mathbf{v}_l\right)_2^2 + \left(\overset{\star}{\mathbf{v}}_l - \mathbf{v}_l\right)_3^2\right\}}. \tag{5.92}$$

By the linearity of the expectation operator we have,

$$\mathrm{rms}\left(\left\|\overset{\star}{\mathbf{v}}_l - \mathbf{v}_l\right\|\right) = \sqrt{E\left\{\left(\overset{\star}{\mathbf{v}}_l - \mathbf{v}_l\right)_1\right\}^2 + E\left\{\left(\overset{\star}{\mathbf{v}}_l - \mathbf{v}_l\right)_2\right\}^2 + E\left\{\left(\overset{\star}{\mathbf{v}}_l - \mathbf{v}_l\right)_3\right\}^2}. \tag{5.93}$$

The three expectation terms above are simply the x, y, z position error variances, which are the diagonal elements of our covariance matrix. Therefore we have,

$$\mathrm{rms}\left(\left\|\overset{\star}{\mathbf{v}}_l - \mathbf{v}_l\right\|\right) = \sqrt{\mathrm{trace}\left(\frac{\sigma^2 c^2}{2\|\boldsymbol{\omega}_c\|^2} \left(\mathbf{V}\mathbf{V}^T\right)^{-1}\right)}. \tag{5.94}$$

5.8 Test Cases

Next we will observe the perturbation of TART position estimates in various test cases, comparing our analytical approximation to results from repeated trials of a numerical simulation. For comparison we will also observe the perturbation of σART position estimates using simulated results.

First however, let us define signal to noise ratio (SNR) in our context. Since the magnitude of the ideal component for each carrier has been set equal to 1, we have

$$\text{SNR} = -20 \log_{10} \sigma, \tag{5.95}$$

which is the signal to noise ratio expressed in decibels (dB). This value represents the ratio of signal power to noise power for each received signal carrier on each reference antenna.

5.8.1 1D Perturbation Simulation

The first test case we will examine is the one-dimensional case very similar to the one described in Section 5.1 and depicted in Figure 5.1, where we let the solution space be along the x axis and in which we had a single reference antenna at $\mathbf{v}_1 = [10\ 0\ 0]^T$. The only difference is that for this case we will add a second reference antenna at $\mathbf{v}_2 = [10\ 0\ 0]^T$, so that both TART (which needs only one reference antenna in the one-dimensional case) and σART (which requires 2 reference antennas in the one-dimensional case) can be performed with this example. In this example we are only interested in errors in the x-direction.

Figure 5.4 shows both the TART and σART metrics for several trials of the perturbation simulations for this one-dimensional case. Each sub-plot contains curves which represent metric values for 10 different trials at a particular value of SNR. These curves have been normalized to have the same scale. Each curve has an "X" associated with it that indicates the location of the maximum value of the metric. The top left sub-plot shows the TART metric in the infinite SNR case, that is the ideal TART metric for this geometry, which resembles Figure 5.1. Similarly the top right sub-plot shows the ideal σART metric. We can see how as the SNR is reduced, both TART and σART degrade. For relatively high SNR the metrics maintain a single central peak and the distribution of peaks appears to be Gaussian where the variance gradually increases as the SNR decreases. After a certain point

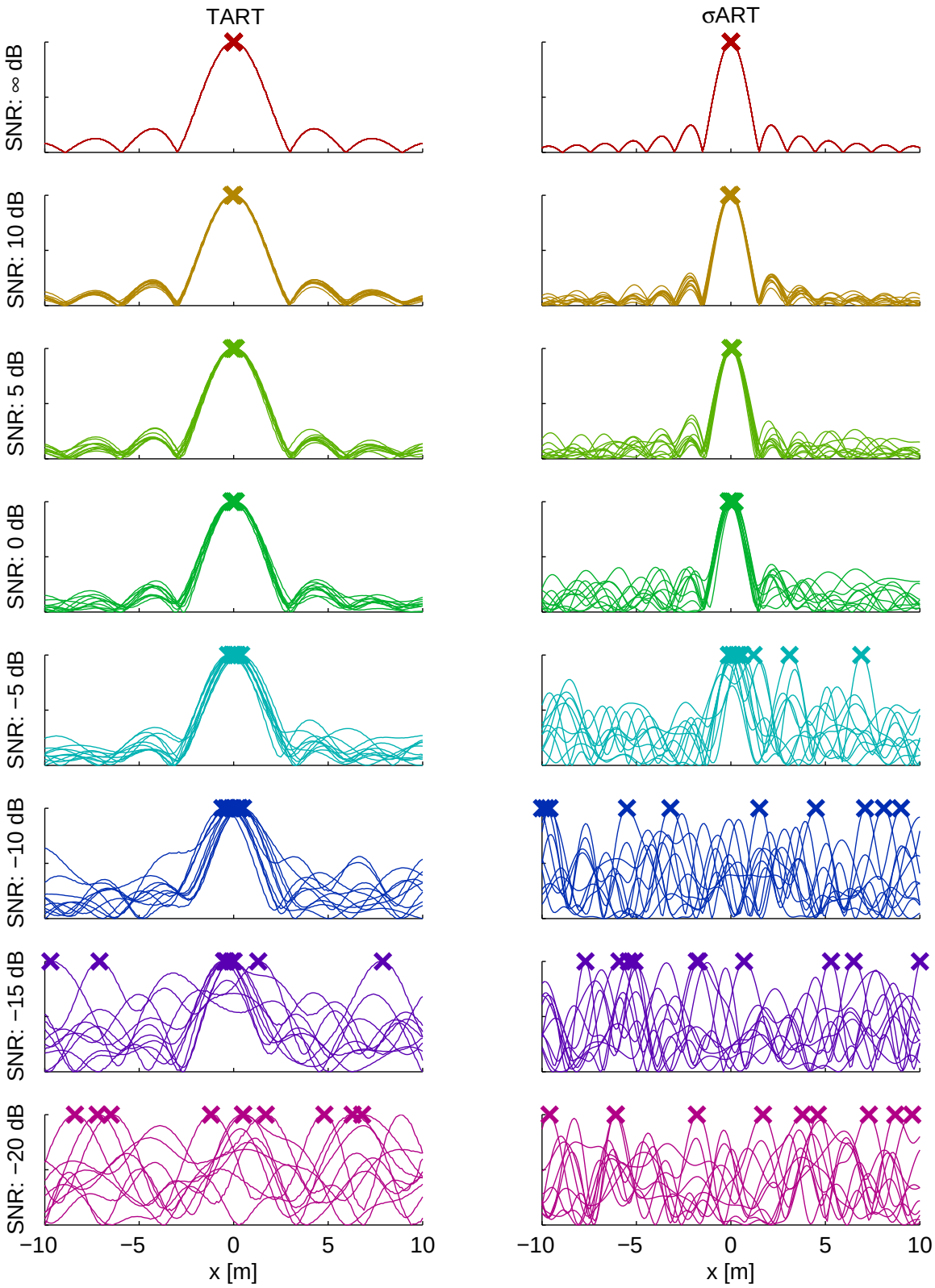

Figure 5.4: 1D Perturbation Simulation Trials

however we have a "breakdown" effect, where secondary peaks begin to become comparable in size to the central peak causing large position errors. We see that TART has significant breakdown at -15 dB SNR, whereas σART breaks down at the much higher -5 dB SNR.

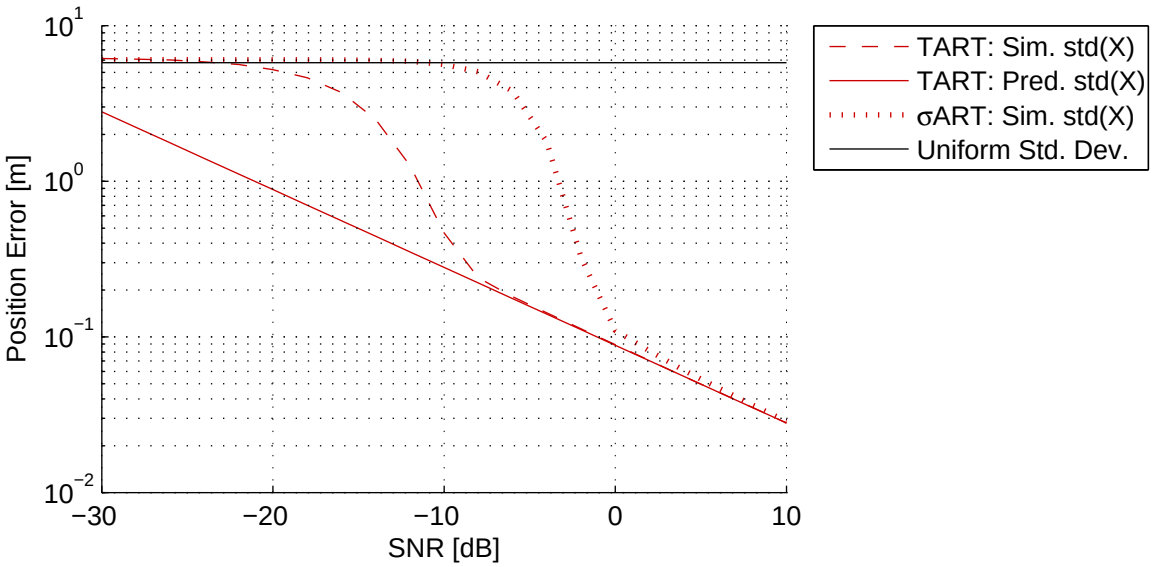

Figure 5.5: 1D Perturbation Simulation

Figure 5.5 shows the position estimate error standard deviation as a function of SNR as predicted by our analytic approximation for TART and as estimated from 100,000 simulation trials for both TART and σART. As expected for high SNR, the predicted and simulated errors become smaller. We also see that for higher SNR the predicted curve matches the simulated curve for TART. This is expected because the approximations made were accurate for high SNR. We see that σART has larger errors than TART for all values of SNR. When the signal to noise ratio becomes lower than approximately -8 dB we see that the simulated standard deviation for TART begins to deviate significantly from the predicted value. This is the breakdown effect which was illustrated in Figure 5.4.

We see in Figure 5.4 that for very low SNR, the distribution of maxima locations appears to be uniform over the search space. Thus in heavy noise the resulting estimates convey no information. Since the truth location is at the origin in this case, the positions of the maxima are the errors. Thus distribution of position errors is approximately uniform over [-10, 10], which is known to have a standard deviation of $\sqrt{\frac{(10-(-10))^2}{12}} \approx 5.7735$.[5] This value is plotted on Figure 5.5 as a horizontal black line. We see that the simulated error standard deviations for both TART and σART take on

approximately this value for very low SNR as expected.

5.8.2 2D Perturbation Simulation

Next we will consider the two-dimensional case depicted in Figure 3.5, with 16 reference antennas on two sides of the scan region. Figure 5.6 shows the perturbation results for both TART and σART in this configuration. The simulated results in this figure were obtained from 10,000 repeated simulations. This plot shows the error standard deviations in the x and y direction, as well as the square root of the x, y covariance. As this is a logarithmic plot we must show the absolute value of the covariance.

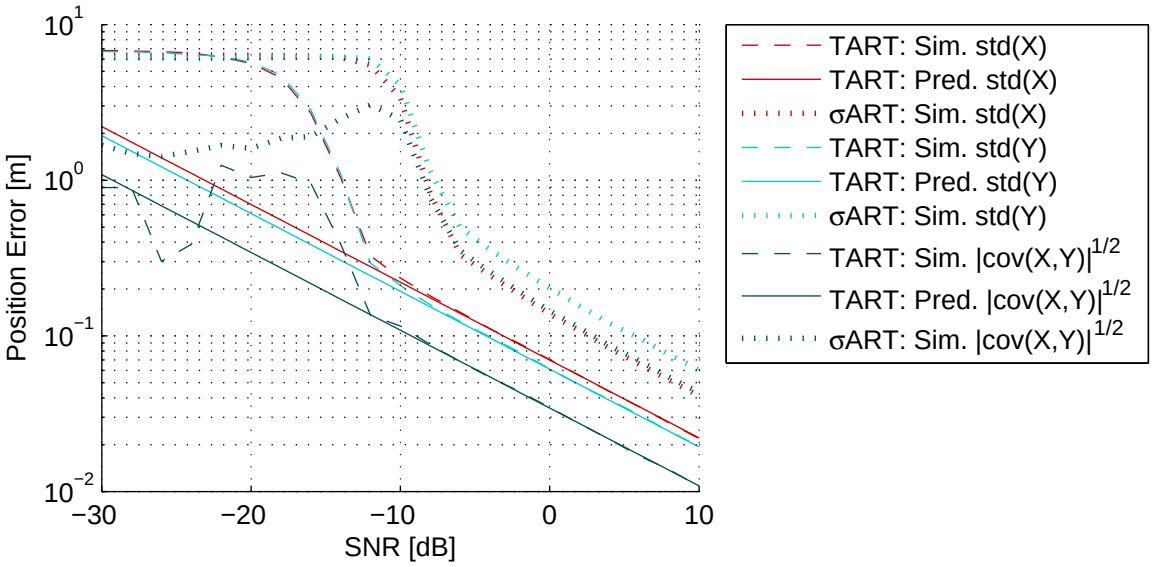

Figure 5.6: 2D Perturbation Simulation

Again we see that the simulated result matches our approximation closely for high SNR. In comparison to the one-dimensional case in Figure 5.5, we see that the position errors are smaller for a given SNR. This is due to the presence of several reference antennas with independent noise, which has an averaging effect on the position estimate. We also see that σART performs significantly worse than TART (by approximately a factor of two), even at high SNR. Both methods approach some constant value as the distribution of maxima becomes uniform at very low SNR. In this case we observe that σART breaks down at an SNR approximately 6 dB higher than TART.

While the plot does not display it, the σART x, y covariance is negative in this example, whereas

the TART x, y covariance is positive. This makes intuitive sense looking at Figure 3.5, which shows that the σART metric is elongated in the $y = -x$ direction, and the TART metric is slightly elongated in the $y = x$ direction. We see that that once TART and σART reach complete breakdown the x and y errors become less correlated.

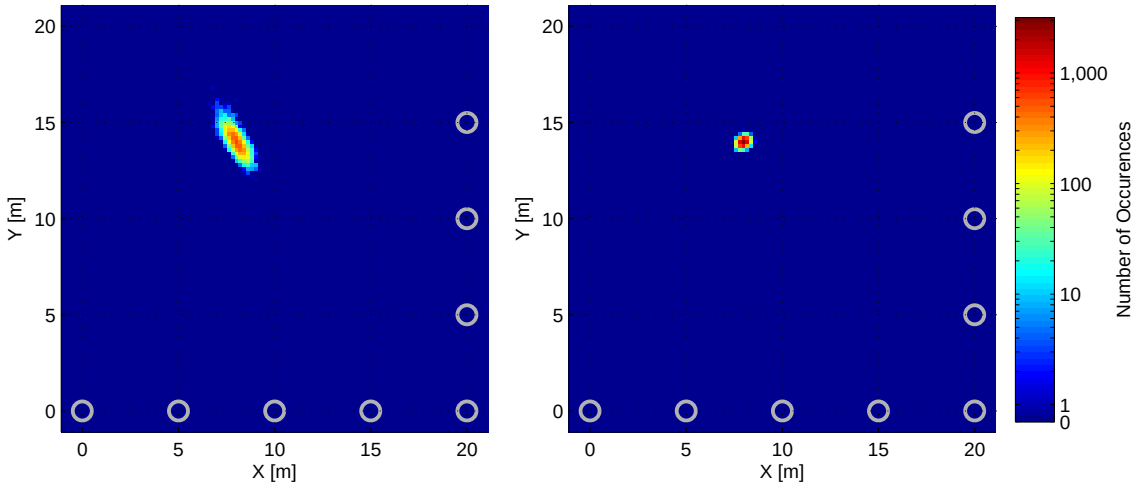

(a) σART (b) TART

Figure 5.7: Histogram of Simulated Position Estimates at -6 dB SNR

Figure 5.7 shows a two-dimensional histogram of the σART and TART position errors for this case at -6 dB SNR. This plot was created by discretizing the solution space with a rectangular grid with 0.2 meter spacing. For each square area in the grid, the number of position estimates within that area was computed and the corresponding pixel of the histogram was colored accordingly. The color bar on the right shows the logarithmic mapping between color and number of occurrences. We see that these histograms look very similar to the metric images in Figure 3.5. We see that there is a direct correspondence between the shape of the σART and TART metrics and the distribution of position estimates, which validates our intuition that metric ambiguity in a certain direction can cause increased position error in that direction.

The probability density function of a multivariate normal random vector $\mathbf{x} \sim N(\mu, \mathbf{\Sigma})$ with m elements is known to be

$$p(\mathbf{x}) = \frac{1}{(2\pi)^m \det(\mathbf{\Gamma})^{1/2}} e^{-\frac{1}{2}(\mathbf{x}-\boldsymbol{\mu})^T \mathbf{\Sigma}^{-1}(\mathbf{x}-\boldsymbol{\mu})}.[5] \tag{5.96}$$

Taking the natural logarithm of this function we have,

$$\ln p(\mathbf{x}) = \ln \frac{1}{(2\pi)^m \det(\mathbf{\Gamma})^{1/2}} - \frac{1}{2} (\mathbf{x} - \boldsymbol{\mu})^T \boldsymbol{\Sigma}^{-1} (\mathbf{x} - \boldsymbol{\mu}) . \tag{5.97}$$

This can be rewritten as

$$\ln p(\mathbf{x}) + k = -\frac{1}{2} (\mathbf{x} - \boldsymbol{\mu})^T \boldsymbol{\Sigma}^{-1} (\mathbf{x} - \boldsymbol{\mu}) , \tag{5.98}$$

where k is an arbitrary constant. If we substitute the parameters for the TART position estimate distribution, which is the TART error distribution from Equation 5.89 shifted to be centered about the true position, we obtain,

$$\begin{aligned} \ln p\left(\overset{\star}{\mathbf{v}}_{\mathbf{l}}\right) + k &= -\frac{1}{2} \left(\overset{\star}{\mathbf{v}}_l - \mathbf{v}_l\right)^T \left(\frac{\sigma^2 c^2}{2\|\boldsymbol{\omega}_c\|^2} \left(\mathbf{V}\mathbf{V}^T\right)^{-1}\right)^{-1} \left(\overset{\star}{\mathbf{v}}_l - \mathbf{v}_l\right) \\ &= -\frac{2\|\boldsymbol{\omega}_c\|^2}{\sigma^2 c^2} \left(\overset{\star}{\mathbf{v}}_l - \mathbf{v}_l\right)^T \mathbf{V}\mathbf{V}^T \left(\overset{\star}{\mathbf{v}}_l - \mathbf{v}_l\right) \end{aligned} \tag{5.99}$$

Recall our Taylor series approximation of the ideal TART peak,

$$f\left(\overset{\#}{\mathbf{v}}_l\right) \approx f(\mathbf{v}_l) + \frac{1}{2} \left(\overset{\#}{\mathbf{v}}_l - \mathbf{v}_l\right)^T \nabla\nabla^T f(\mathbf{v}_l) \left(\overset{\#}{\mathbf{v}}_l - \mathbf{v}_l\right). \tag{5.100}$$

From Section 5.6.1 we know that,

$$\nabla\nabla^T f(\mathbf{v}_l) = \frac{\|\boldsymbol{\omega}_c\|^2}{c^2} \mathbf{V}\mathbf{V}^T. \tag{5.101}$$

Therefore we have,

$$f\left(\overset{\#}{\mathbf{v}}_l\right) \approx f(\mathbf{v}_l) + \frac{\|\boldsymbol{\omega}_c\|^2}{2c^2} \left(\overset{\#}{\mathbf{v}}_l - \mathbf{v}_l\right)^T \mathbf{V}\mathbf{V}^T \left(\overset{\#}{\mathbf{v}}_l - \mathbf{v}_l\right), \tag{5.102}$$

which has a very similar form to Equation 5.99. We can say that

$$\ln p\left(\overset{\star}{\mathbf{v}}_{\mathbf{l}}\right) + k \propto f\left(\overset{\#}{\mathbf{v}}_l\right), \tag{5.103}$$

where $\propto$ represents proportionality. We see that the shape of the ideal TART metric peak is proportional to the logarithm (ignoring the constant offset k) of the probability distribution of position estimates when noise is introduced. This explains why our histogram of TART position estimates looks similar to the original TART image, and while not shown explicitly, the same behavior appears to be true for σART.

5.8.3 3D Perturbation Simulation

Finally we will examine an example in the full three-dimensional case. This case is identical to that depicted in Figure 3.9, with eight reference antennas on two sides of the scan region having staggered heights and the mobile unit is positioned at $\mathbf{v}_l = [8\ 14\ 3]^T$. The scan limits in the vertical dimension were from 0 to 6 meters.

The results for this case are shown in Figure 5.8. The simulated results for this case were the result of 10,000 repeated trials. Again we see that TART outperforms σART significantly (by a

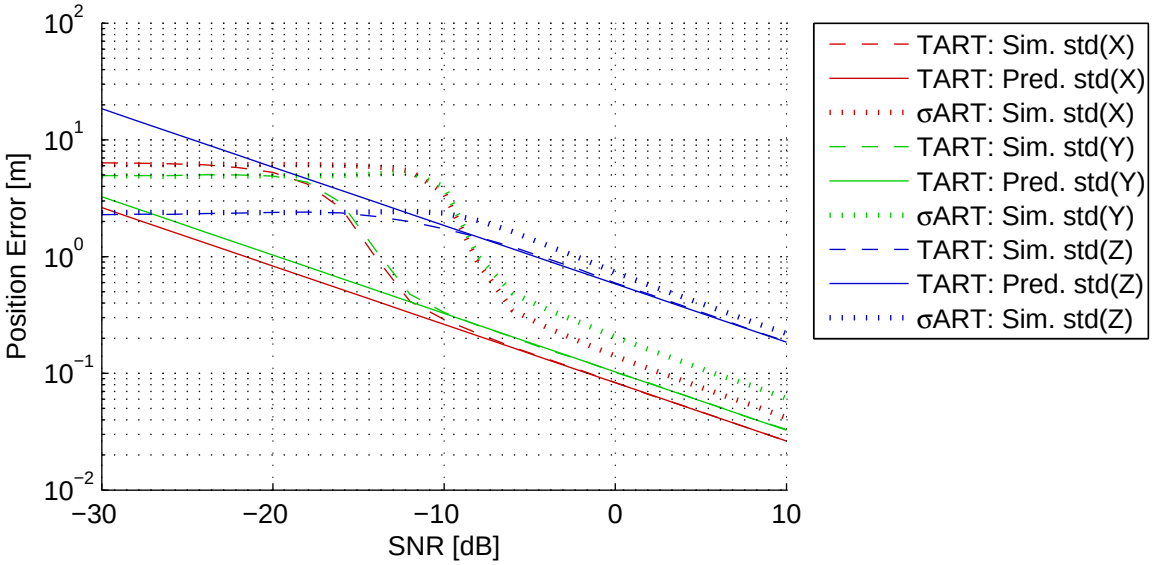

Figure 5.8: 3D Perturbation Simulation: Error vs. SNR

factor of approximately two), and our approximation for TART error closely matches the simulated results for high SNR. We observe that σART breaks down at an SNR approximately 6 dB higher than TART in this case. We also see that for both σART and TART the vertical error is significantly larger (by a factor of approximately six) than the horizontal error. This corresponds to the shape of the metric peaks observed in Figure 3.9, and is expected since the reference antennas have much more diversity in the horizontal dimensions.

With the ability to determine error variances for various system geometries and any level of SNR with repeated simulation trials begs the question: what is the value of having an error variance approximation for high SNR only? First we must note that the derivation of the error variance approximation itself was a useful path that provided significant insight to the TART process and how

it behaves. Second, our approximation can be evaluated much more quickly than a numerical simulation with thousands of repeated trials, while still revealing the error sensitivities for a particular geometry. For example, for a particular reference antenna geometry, our high SNR approximation can quickly provide the error statistics for an entire span of mobile antenna locations, i.e. all locations in the scan region.

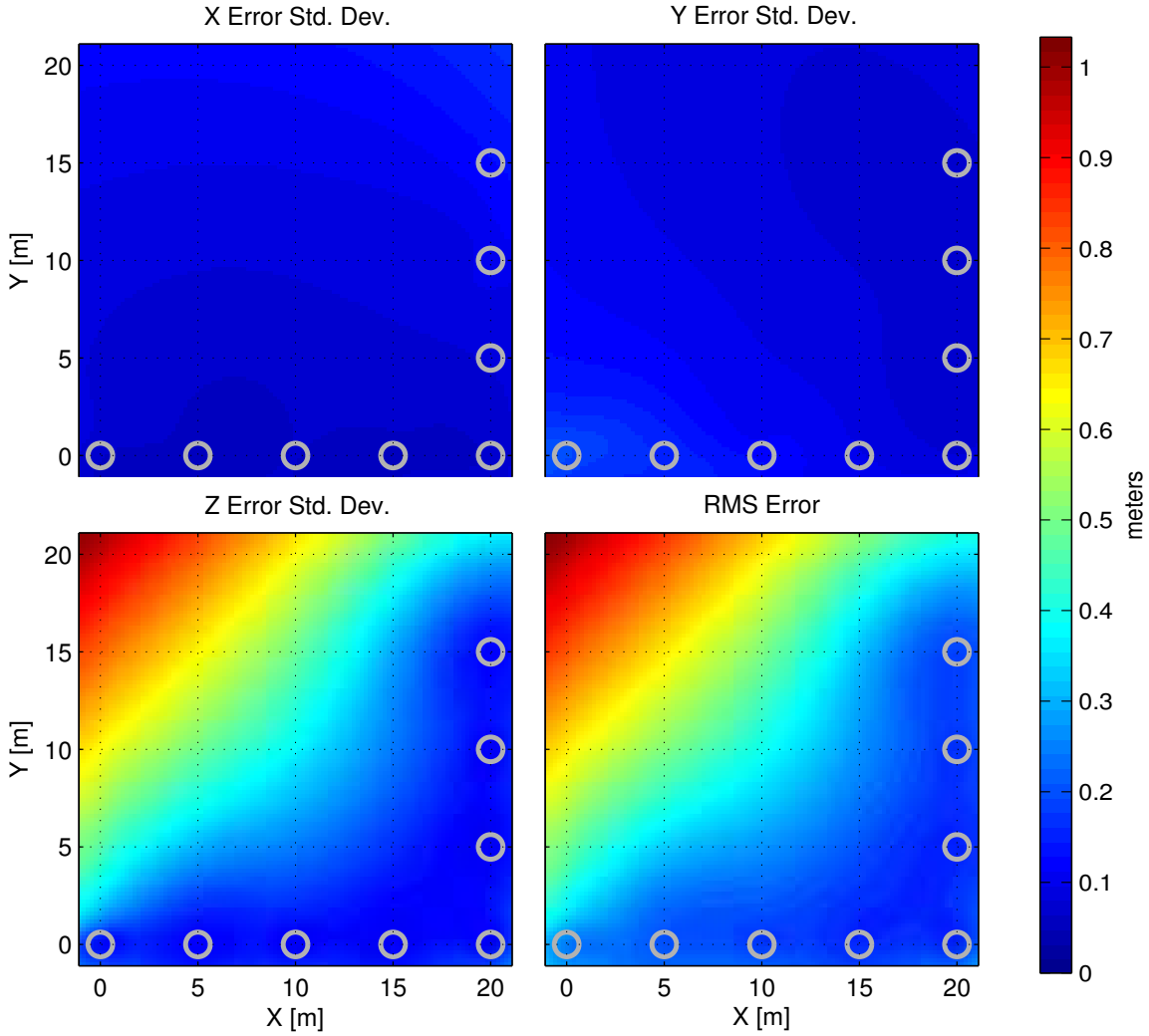

Figure 5.9: Predicted TART Error vs. Mobile Location at 0 dB SNR, $z = 3$

An example of this is shown in Figure 5.9. This again represents the "practical" reference antenna geometry from Figure 3.9, but in this case we show the corresponding error statistics for the mobile antenna being located at different positions in space for 0 dB SNR. In this figure we see

various error statistics for $(\mathbf{v}_l)_1 \in [-1, 21]$, $(\mathbf{v}_l)_2 \in [-1, 21]$, $(\mathbf{v}_l)_3 = 3$, all possible locations in the horizontal dimensions when the height is fixed at 3 meters.

We see that for this geometry the error is predominantly in the vertical dimension, and that the smallest errors occur when the mobile antenna is close to the reference antennas. As the mobile antenna gets farther from the reference antennas the vertical error grows considerably.

Chapter 6

Experimental Results

The measures described in Chapter 4 have been implemented to create a system capable of performing TART with real data. This chapter describes a series of tests that were performed to observe the location estimation performance of TART in real situations. The tests described in this chapter all used a multicarrier signal with 100 MHz of bandwidth and 156 carriers. Additionally a bandwidth extrapolation technique was used to synthetically increase the bandwidth to 133 MHz. This technique fits a autoregressive model to the received frequency data from which additional frequency samples are extrapolated.[25] This technique has been used for years by the PPL system for σART processing and has showed improved results consistently.

All tests described in this chapter use the original transactional synchronization scheme, as opposed to the alternative scheme proposed in Section 3.3.5. This was simpler to implement for these proof-of-concept tests. Testing of the alternative scheme was conducted in the laboratory which showed that both techniques produce nearly identical estimates for the random time offset, implying that they would have the same level of performance for indoor location testing.

6.1 Laboratory Proof of Concept

The first test of TART was performed inside of our laboratory. For this test two of our transceiver units were used. One of the transceivers acted as the stationary reference unit with four antennas connected to it, whereas the other transceiver acted as the mobile unit to be located, with a single antenna connected to it. One significant unrealistic attribute of this test was that both transceivers

were driven by a common oscillator. This allowed the time varying time-offset $\tilde{\tau}(t)$, discussed in Section 4.4, to be assumed to be constant. In a final system this would not be the case, but it was an accepted assumption for this initial proof of concept test. Still in the proof of concept stage, the firmware for the transceivers was not optimized for efficient transactional data captures, so capturing the data from the set of transactions at a given mobile antenna location took as much as 30 seconds to complete. Thus real-time positioning was not possible, but the data was analyzed in post processing. Since the random time-offset was fixed, the time between transactions was not critical.

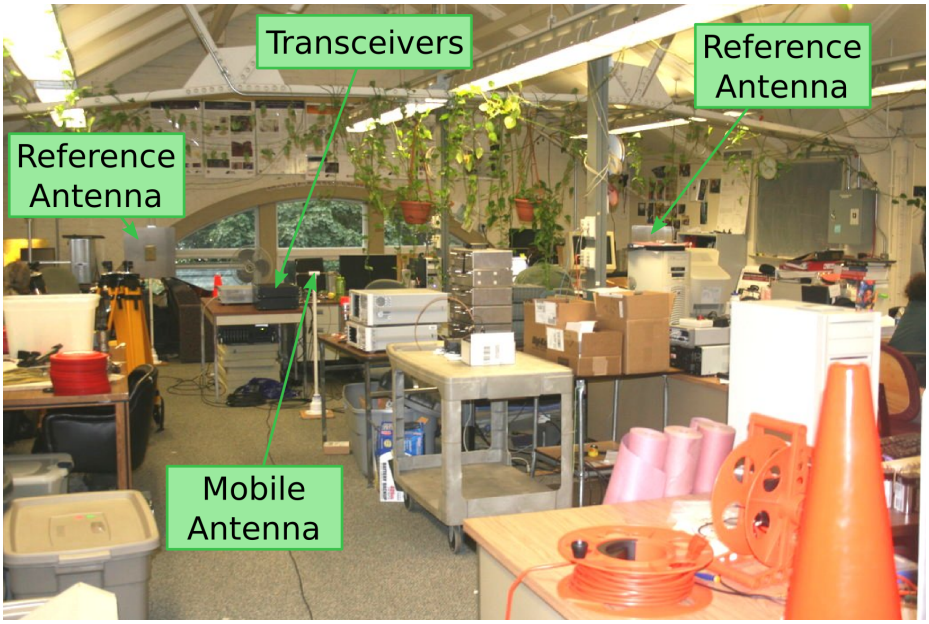

Figure 6.1: Laboratory Test Setup

Figure 6.1 shows the interior of the laboratory used for this test. Two of the four reference antennas are visible, as well as the mobile antenna at one of its locations. In some cases the mobile antenna has direct line of sight to the reference antennas, but in other cases it was obscured by the various objects in the room. There were also many metal objects and structural beams creating a moderate multipath environment. The transceiver units themselves were co-located and connected with cables to the antennas, as shown in Figure 6.2.

The mobile antenna was placed at 18 surveyed locations throughout the lab, at a constant height that matched the reference antennas. At each location, the necessary transactional signals were recorded in order to perform TART. This data was then analyzed with both σART and TART. The

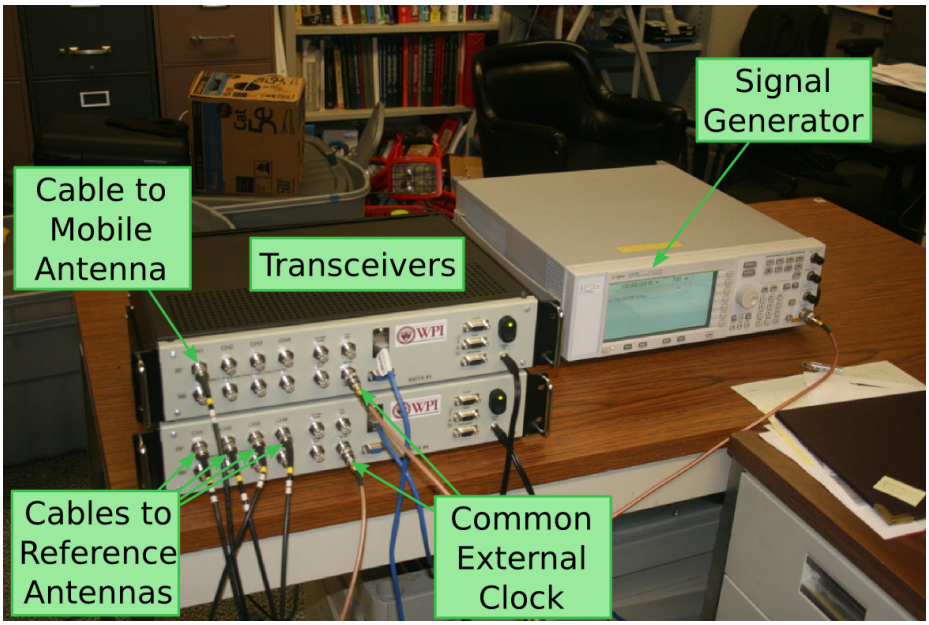

Figure 6.2: Laboratory Test - Transceivers

σART algorithm ignores the additional timing information obtained by the transactional synchronization procedure and behaves as it would in the traditional TDOA system. The data was first analyzed using a two-dimensional scan.

Figure 6.3 shows the result of from the first location for both σART and TART. We see that in this case both algorithms result in an approximately the same error of about 0.2 meters. Careful examination of the TART metric shows arcs centered at the reference antennas that pass through the location of the mobile antenna, as observed in Figure 3.6.

Figure 6.4 summarizes the performance at all 18 mobile antenna locations. The plot on the left illustrates the errors with a vector pointing from each truth location to the estimated location for both σART and TART. We see that at most locations the errors for both σART and TART are relatively small. The table provides error statistics, showing that TART had smaller RMS, median and maximum errors than σART. There was one particular location in which σART had a large 2.11 meter error. The metric images for this case are shown in Figure 6.5. We see that the σART image had multiple peaks; one close to the true location, and one 2.11 meters away that was chosen as the largest peak. This suggests that the σART has incorrectly chosen a peak corresponding to a reflector, as observed in simulation in Figure 3.2.

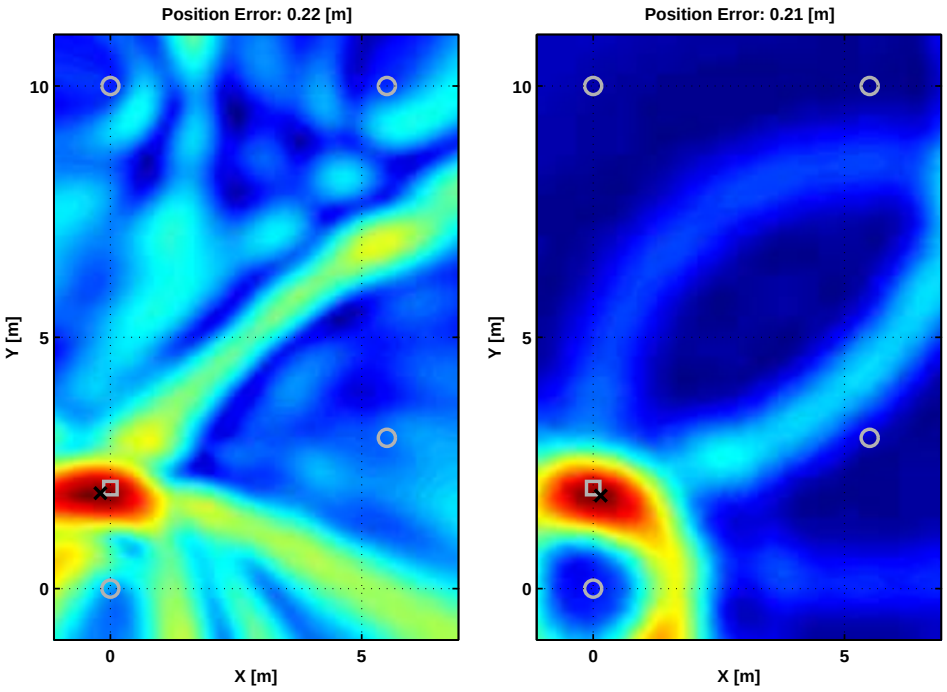

(a) σART (b) TART

Figure 6.3: σART vs. TART - Laboratory Test: 2D, 4 Reference Antennas, Location 1

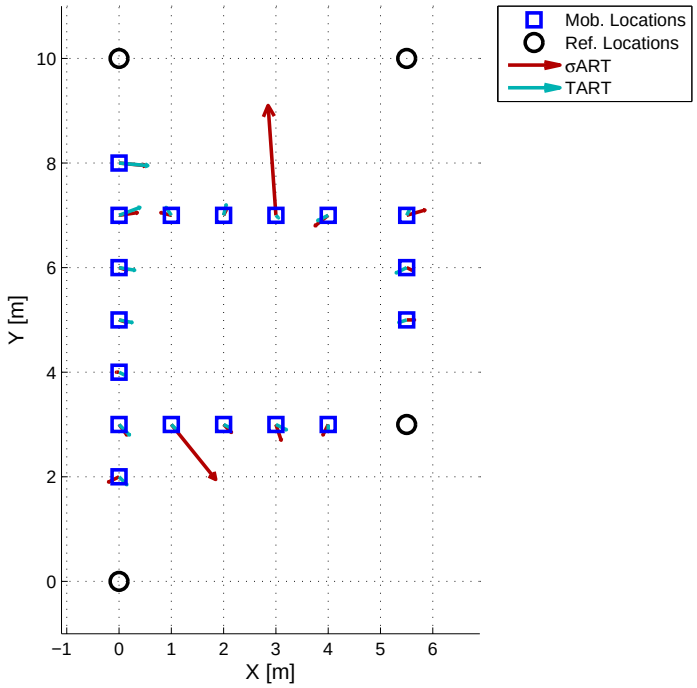

Error [m]	σART	TART
RMS	0.64	0.25
Med.	0.22	0.21
Max.	2.11	0.55

Figure 6.4: Error Summary - Laboratory Test: 2D, 4 Reference Antennas

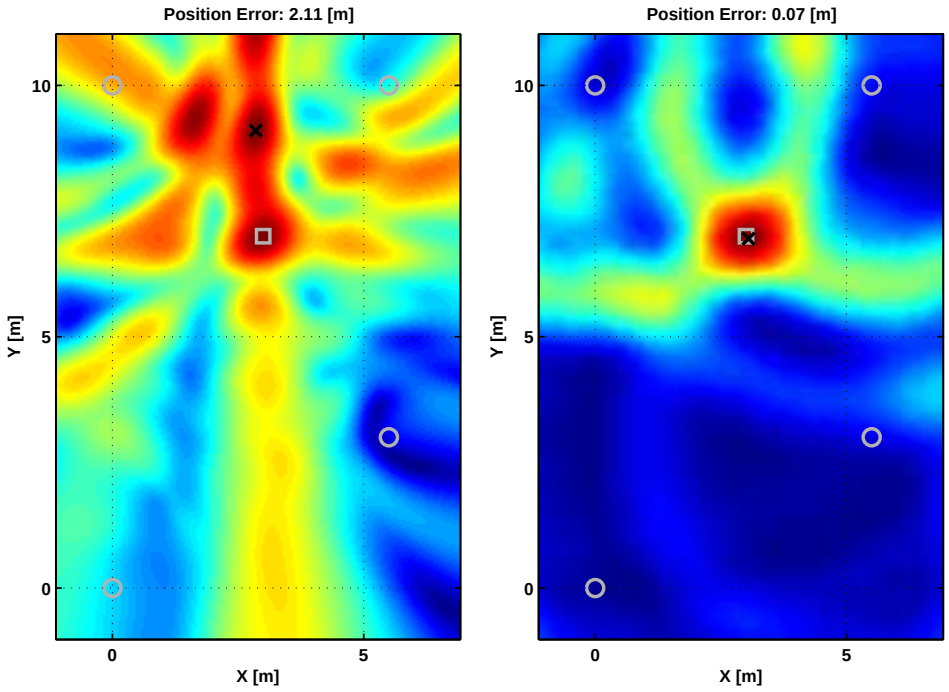

(a) σART (b) TART

Figure 6.5: σART vs. TART - Laboratory Test: 2D, 4 Reference Antennas, Location 16

The data from this test was then analyzed with the data from one of the reference antennas discarded. This simulates the effect of only having three reference antennas in a reduced geometry situation. The results from this analysis are summarized in Figure 6.6. We see that the σART performance degrades dramatically, having three large outliers and many other points with increased error. In contrast, TART has only slight degradation. This agrees with the simulations that suggest TART has superior performance in reduced geometry situations.

The data was then analyzed using a full three-dimensional scan. Figure 6.7 shows the result at Transmitter Location 2. We see that the σART metric volume has significant ambiguity in the vertical direction, as predicted by the simulations. The TART metric is much more localized vertically. At Location 3, shown in Figure 6.8 we see that σART has a gross error due to this vertical ambiguity, whereas TART performs well. These two locations show the general trend that the height errors from σART are sometimes small and sometimes very large, while TART has consistently small height errors.

Figure 6.9 summarizes the three-dimensional scan results for all of the mobile antenna locations.

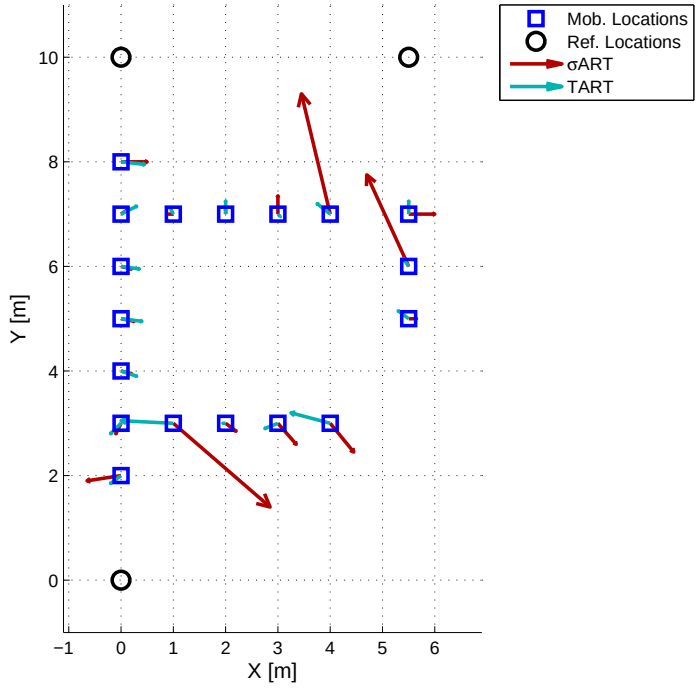

Error [m]	σART	TART
RMS	0.99	0.40
Med.	0.30	0.28
Max.	2.45	1.00

Figure 6.6: Error Summary - Laboratory Test: 2D, 3 Reference Antennas

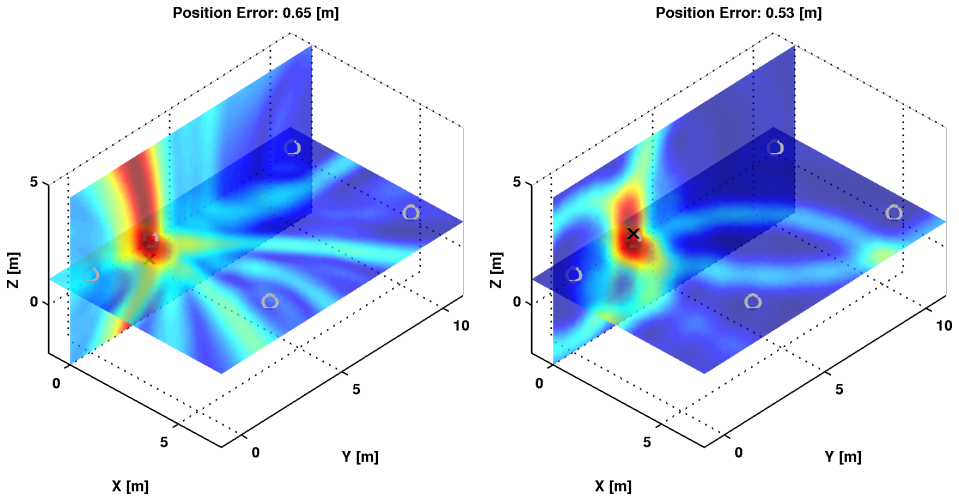

(a) σART (b) TART

Figure 6.7: σART vs. TART - Laboratory Test: 3D, 4 Reference Antennas, Location 2

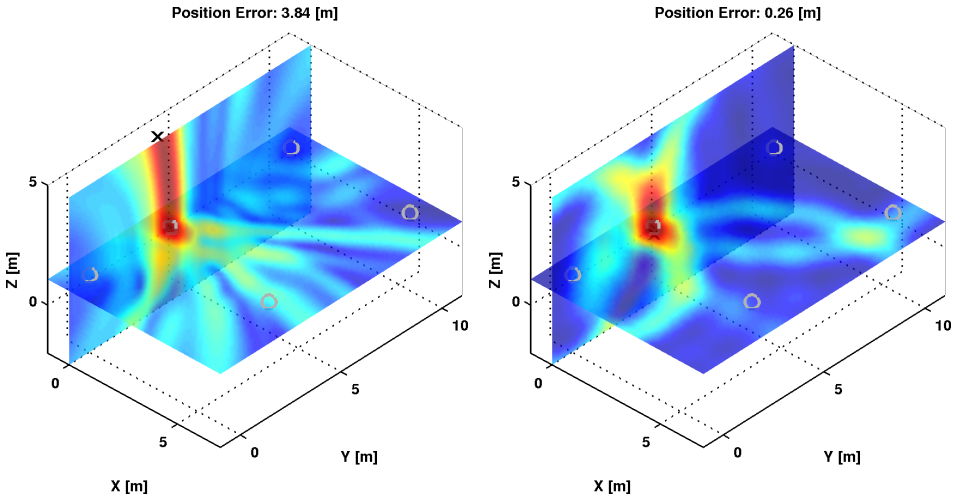

(a) σART (b) TART

Figure 6.8: σART vs. TART - Laboratory Test: 3D, 4 Reference Antennas, Location 3

The error vector plot on the left displays the horizontal errors; we can see that even in the horizontal direction σART suffers without knowledge of the correct height to scan. The table displays the overall errors as well as the horizontal and vertical components of the error. We see that σART is outperformed by TART most dramatically in the vertical direction.

This test was a major milestone in the development of TART. It showed that TART, along with transactional synchronization and its many hardware considerations explained in Chapter 4, had been implemented properly. It also confirmed the performance benefits suggested by the simulations to be true for real data as well.

6.2 Line of Sight Test

After the initial laboratory proof of concept test, a full scale test was performed in a large auditorium in WPI's Alden Hall building. This was an unobstructed line of sight case with minimal multipath, as close to an ideal case as possible to observe baseline performance. Figure 6.10 is a photograph of the test setup in the auditorium. Visible is the mobile antenna that was moved about the testing area, as well as several of the reference antennas, of which there were 12 in total. This test used five transceiver units, four of which acted as reference transceivers with three antennas, and one as the mobile transceiver with one antenna. The mobile antenna was mounted to a longer

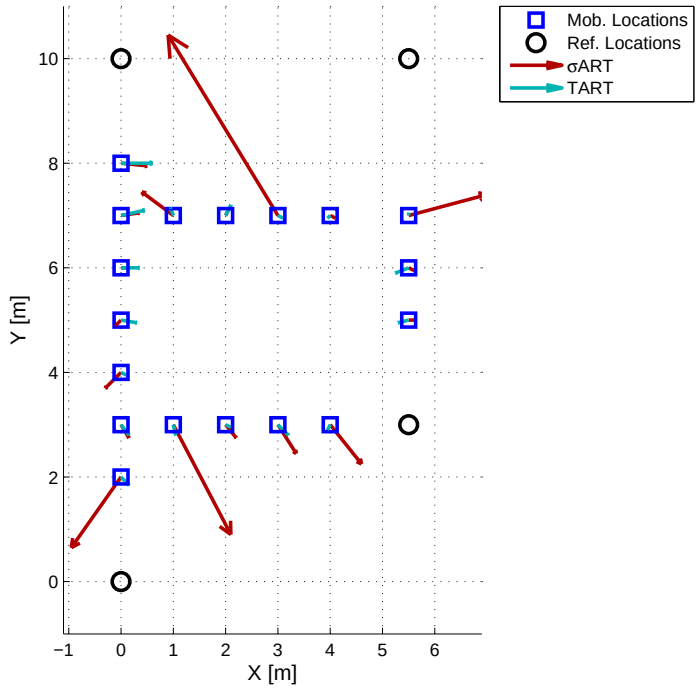

Error [m]	σART	TART
RMS	2.96	0.39
Med.	2.00	0.35
Max.	5.63	0.61
XY RMS	1.29	0.27
XY Med.	0.39	0.21
XY Max.	4.04	0.60
Z RMS	2.67	0.28
Z Med.	1.83	0.23
Z Max.	3.92	0.52

Figure 6.9: Error Summary - Laboratory Test: 3D, 4 Reference Antennas

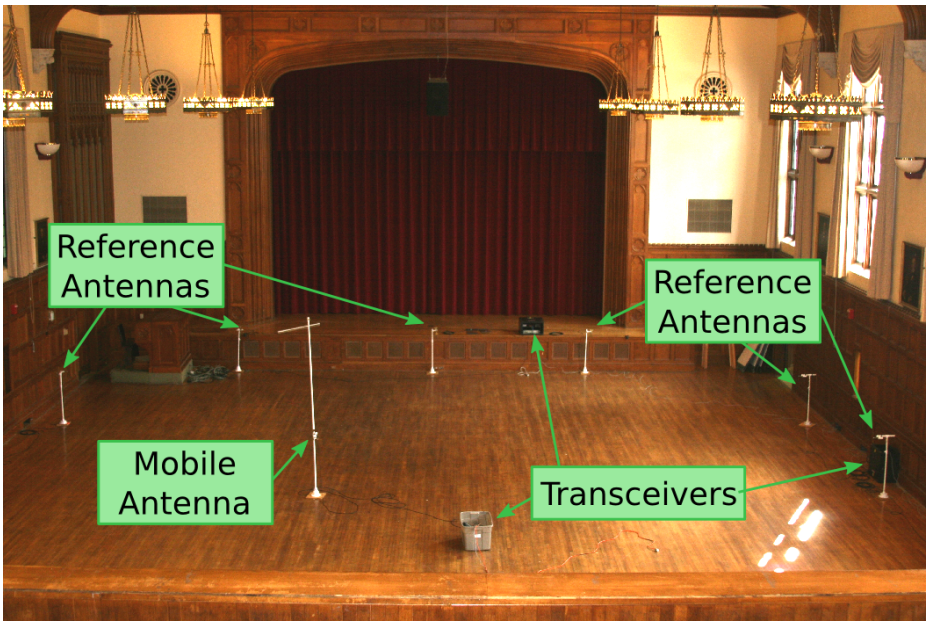

Figure 6.10: Alden Hall Test Setup

pole to allow its height to be varied.

A significant change from the laboratory proof of concept test was that all of the transceivers were driven by independent oscillators, which were Rubidium atomic clocks. The relative drift of these clocks was determined experimentally to be negligible over the approximately 30 second capture times, allowing us to assume $\tilde{\tau}$ to be constant for each location capture.

Two sets of data or "runs" were obtained during this test. The first consisted of the mobile antenna placed at 15 different locations throughout the testing area at the same height as the reference antennas. The second run consisted of the mobile antenna being placed at one of those locations and having its height varied.

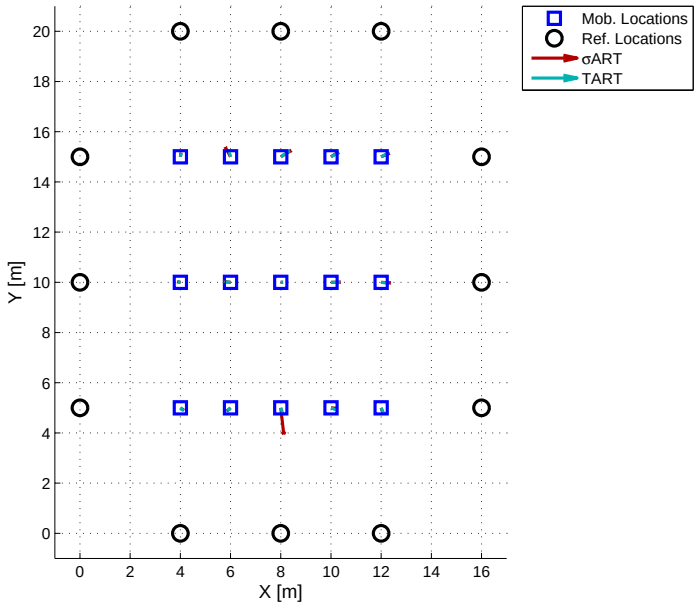

Error [m]	σART	TART
RMS	1.61	0.67
Med.	0.29	0.27
Max.	5.58	1.65
XY RMS	0.40	0.27
XY Med.	0.29	0.26
XY Max.	1.06	0.44
Z RMS	1.56	0.61
Z Med.	0.00	0.00
Z Max.	5.47	1.62

Figure 6.11: Error Summary - Alden Hall Test: 3D, Run 1, 12 Reference Antennas

The data from Run 1 was analyzed with a three-dimensional scan, the results of which are summarized in Figure 6.11. We see once again that TART is more accurate than σART, particularly in regards to the vertical error. There are however, two very striking entries in this error table. Both σART and TART have zero median error in the vertical dimension. This implies that more than half of the mobile antenna locations had no error, which seemingly should not happen. This behavior is an effect of the particular geometry used for this run of the test, in which all reference antennas were placed at the same height, thus being coplanar. This causes both the σART and TART metrics

to be symmetrical about the plane. Since the mobile antenna is also in the same plane, the solution peak is expected to be very close to this plane, and in some cases the symmetry of the σART/TART metric about the plane causes the maximum to be located precisely in the plane. In a more realistic case where the reference antennas have some height diversity this would not be an issue.

Further, if the mobile antenna is raised above the plane then the solution peak moves far enough away so that a maximum does not exist in the plane, as we will see from the second run's data. However, by symmetry a pair of equally size maxima must exist, one above the plane and one below the plane. This ambiguity is avoided by constraining the search space to only include the space above the reference antennas. For this test we assume that the mobile antenna must be within the auditorium and not below the floor. Similarly, in a real situation constraining the search space to only include the building and immediately surrounding area would be advisable.

Figure 6.12 shows the results of analyzing the data from the first run using only six reference antennas, showing a reduced geometry case. We see that σART degrades more that TART does, having significantly larger errors in all categories. TART does have a rather large maximum error of 3.79.

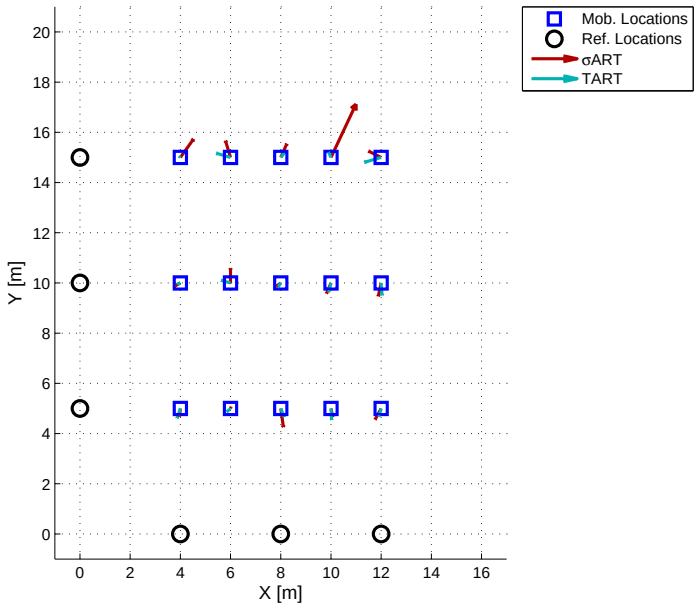

Error [m]	σART	TART
RMS	2.58	1.81
Med.	0.58	1.21
Max.	6.30	3.85
XY RMS	0.79	0.38
XY Med.	0.53	0.36
XY Max.	2.35	0.69
Z RMS	2.46	1.77
Z Med.	0.00	1.16
Z Max.	5.85	3.79

Figure 6.12: Error Summary - Alden Hall Test: 3D, Run 1, 6 Reference Antennas

Run 2 consisted of six data captures with the mobile antenna at a constant horizontal (x,y)

location (6,10) meters, but different heights (1.15, 2.00, 3.00, 4.00, 5.00, and 5.63) meters. The reference antennas were all at a height of 1.15 meters. The results of analyzing this run with all 12 reference antennas are displayed in Figure 6.13. We see again that TART outperforms σART. We

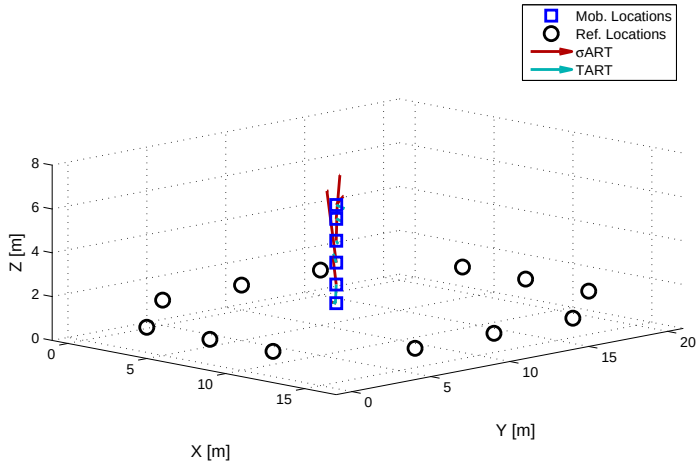

Error [m]	σART	TART
RMS	1.71	0.46
Med.	1.15	0.36
Max.	3.24	0.85
XY RMS	0.35	0.26
XY Med.	0.26	0.26
XY Max.	0.65	0.43
Z RMS	1.68	0.38
Z Med.	1.14	0.12
Z Max.	3.17	0.85

Figure 6.13: Error Summary - Alden Hall Test: 3D, Run 2, 12 Reference Antennas

also see that we no longer have the degenerate geometry issue causing solutions to be in the plane of the reference antennas. The error vector plot illustrates that both methods have relatively accurate horizontal performance, but σART has significantly larger vertical errors.

Finally we show the results of Run 2 with the 6 reference antenna reduced geometry in Figure 6.14. Again we see TART outperforms σART. Both methods seem to have minor degradation

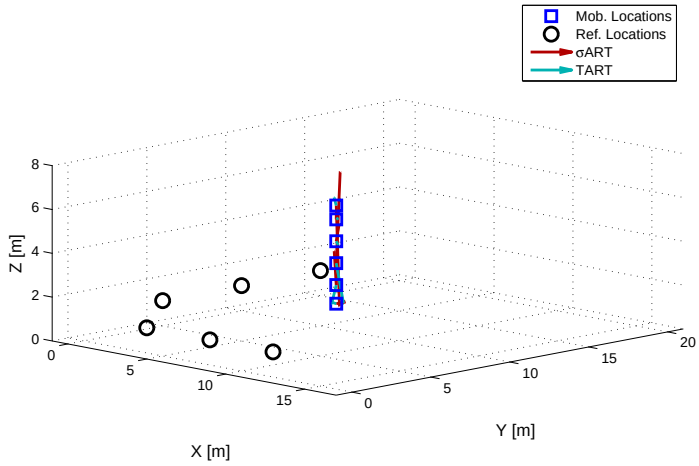

Error [m]	σART	TART
RMS	2.59	0.90
Med.	1.16	0.43
Max.	4.51	1.88
XY RMS	0.46	0.28
XY Med.	0.38	0.27
XY Max.	0.73	0.38
Z RMS	2.55	0.85
Z Med.	1.14	0.28
Z Max.	4.48	1.85

Figure 6.14: Error Summary - Alden Hall Test: 3D, Run 2, 6 Reference Antennas

relative to the full geometry case.

The Alden Hall test proved to be a valuable step in showing the advantages and viability of TART in full scale test, particularly in showing that TART functioned as expected with each transceiver driven by an independent oscillator. This test shows us the level of accuracy that can be expected in an environment with unobstructed direct path signals.

6.3 Building Test

A test was conducted at the WPI Religious Center, a three-story residential structure on campus. This test used 16 reference antennas mounted on 4 ladders that were erected on one side of the building, as depicted in Figure 6.15. With this test we hoped to show that TART would provide accurate location performance in a situation with reference antennas on only one side of a building, unlike various σART tests in recent years which utilized reference antennas fully surrounding the building.

Figure 6.15: Religious Center Test

For this test data was collected with the mobile antenna at 19 different locations: 11 on the first

floor, 5 on the second floor and 3 on the third floor. This data was analyzed with both σART and TART with a three-dimensional scan region. Figure 6.16 displays the horizontal error vectors for the mobile antenna locations on the first floor. We see that the TART has significantly smaller errors than σART. We see that σART has particularly large errors in the x direction. This is expected as we have seen that σART tends to have large errors when the reference antennas are nearly coplanar, in the direction perpendicular to the plane. This behavior can be examined more closely in Figure 6.17, which shows slices of the three-dimensional σART and TART metrics for one of the mobile antenna locations on the first floor. We see that the σART metric is elongated in the x direction.

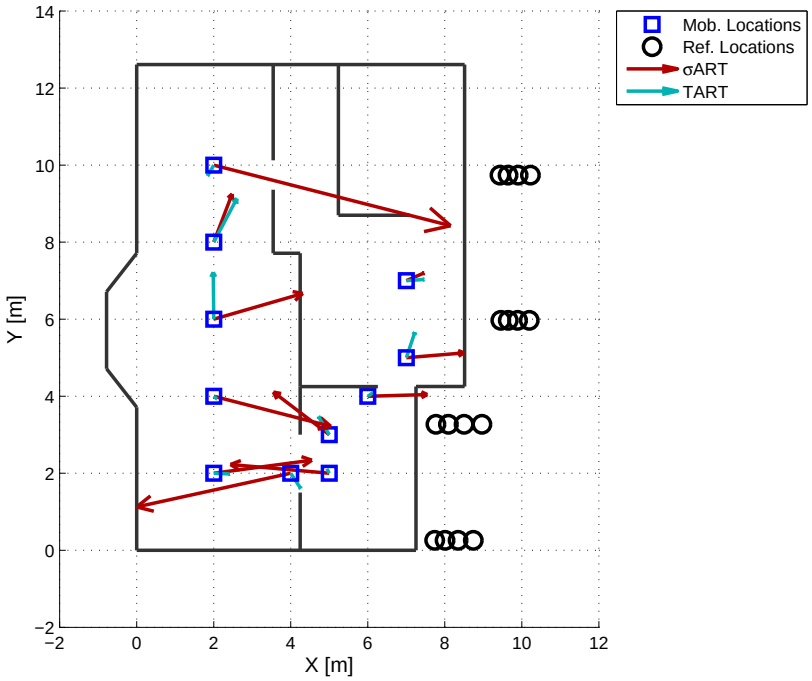

Figure 6.16: Residential Building Test: 3D, First Floor Error Plot

Figure 6.18 and Figure 6.19 display the horizontal error vectors for the mobile antenna locations on the second and third floors respectively. Again we see that TART generally outperforms σART. Table 6.3 summarizes the errors for the points from all three floors. We see that TART outperforms σART throughout, with an overall median error of 0.75 meters compared to 2.36 meters for σART. We see that the σART error in the vertical dimension is actually comparable to σART in this test, but this was achieved by sacrificing σART accuracy in the x direction.

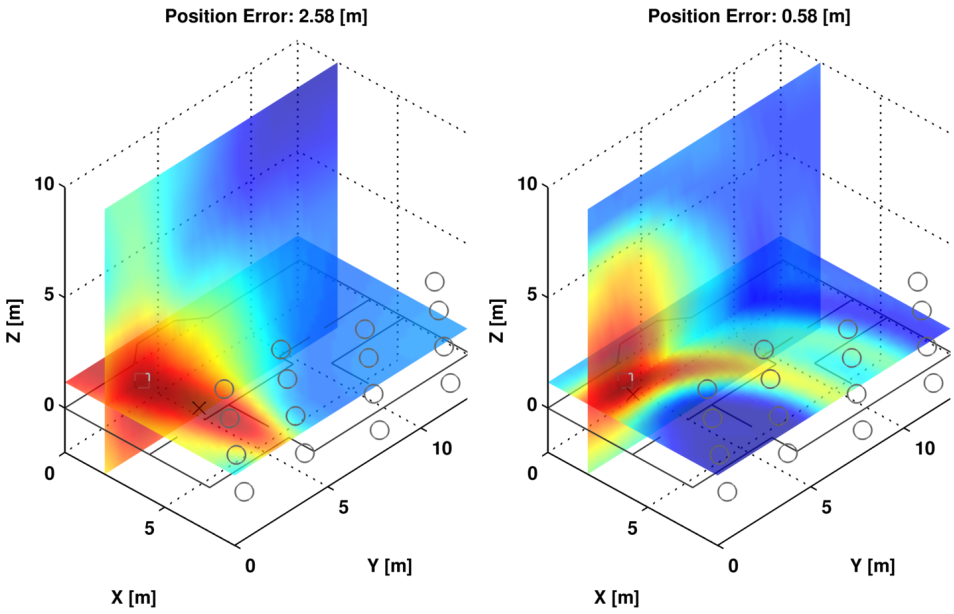

(a) σART (b) TART

Figure 6.17: σART vs. TART - Residential Building Test: 3D, Location 1

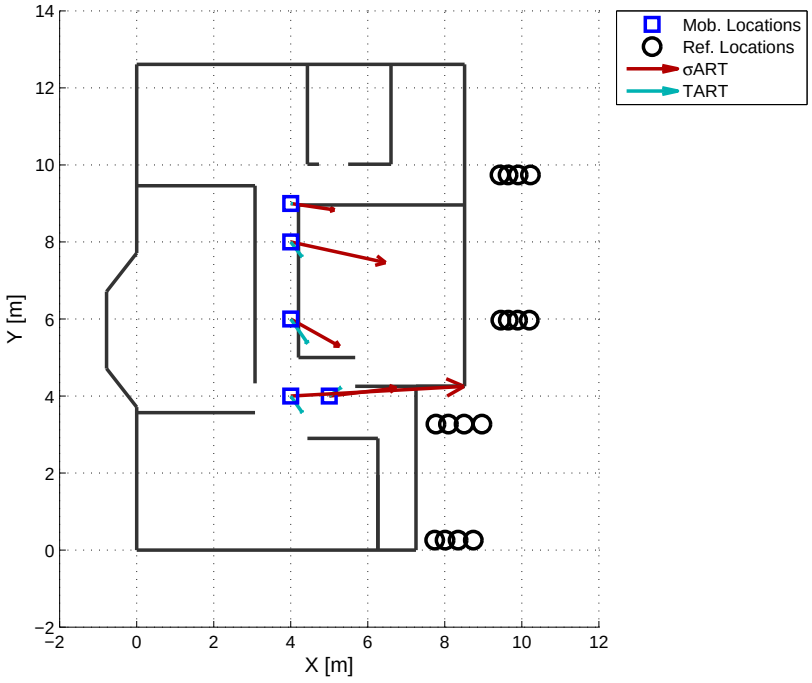

Figure 6.18: Residential Building Test: 3D, Second Floor Error Plot

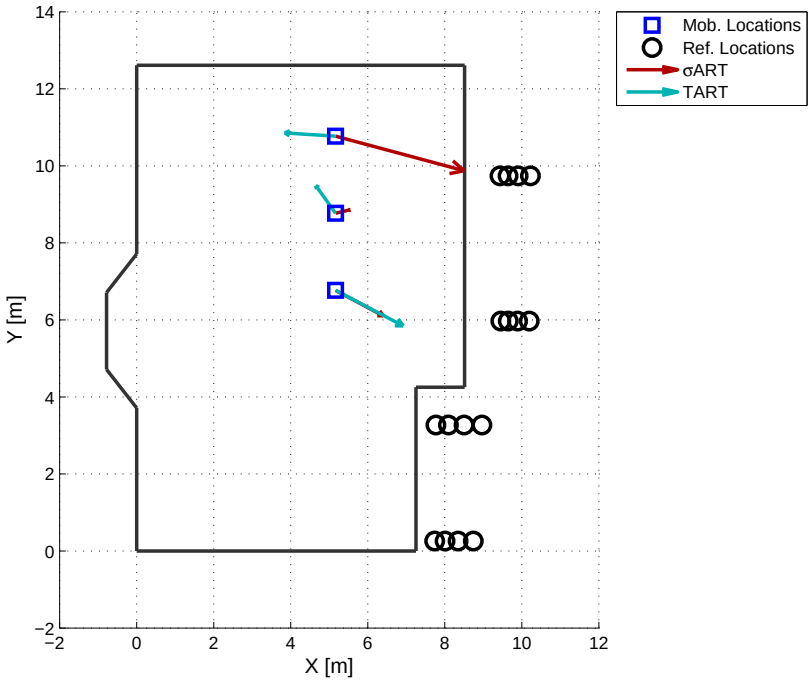

Figure 6.19: Residential Building Test: 3D, Third Floor Error Plot

Error [m]	σART	TART
RMS	2.95	1.26
Med.	2.36	0.75
Max.	6.52	3.04
XY RMS	2.75	0.81
XY Med.	1.83	0.49
XY Max.	6.35	1.99
Z RMS	1.07	0.97
Z Med.	0.33	0.45
Z Max.	3.01	2.91

Table 6.1: Error Summary - Residential Building Test

Chapter 7

Conclusion

This dissertation proposes a novel approach to precision indoor location, as an extension of our existing prototype system. The current system is unique in that it uses a multicarrier signal and multi-signal fusion algorithm to directly estimate the location of a radio transmitter without first estimating the range of the mobile transmitter to each reference station. By introducing a new hardware system architecture which utilizes bidirectional ranging signals it has been shown that additional timing information can be extracted to obtain TOA-like synchronization, which provides various advantages. This new approach has been named Transactional Array Reconciliation Tomography (TART), which consists of an extension of the multi-signal fusion algorithm for synchronized data, as well as the necessary synchronization scheme.

After describing the problem of precision personnel location and why we have chosen a radio based approach, this dissertation described the multicarrier signal structure, which samples the radio channel response to that received signals contain position information. These received signals are challenged by two notable non-ideal synchronization effects: a random frequency-independent phase offset due to unsynchronized mixers and a random time-offset due to having an unsynchronized DAC and ADC. These non-ideal synchronization effects have a substantial impact on the design of algorithms for processing received signals. It was described how the σART algorithm deals with these effects while estimating position from several received signals.

The TART algorithm however was designed with the assumption that there was no random time-offset, only the frequency independent phase offset. Simulated results showed that the information

obtained by removing the random time-offset offered substantial advantages in some cases. These advantages include rejection of reflective objects as position estimate solutions, improved performance with limited reference unit geometries and significant computation reduction. Efforts were then made to show that obtaining this determining this random time-offset was possible using a signal transaction, if the mobile unit to be tracked as well as the reference units outside the building become transceivers that exchange signals with one another. The use of an alternative transactional synchronization scheme was described in Section 3.3.5 which does not require received signal data be sent over a digital data link to the base station to be processed. As a theoretical framework and the practical testing, necessary to prove that this concept was valid, were implemented, various additional complications arose which needed to be overcome. These included the intra-unit synchronization of the transmit and receive circuitry on the transceivers, frequency response calibration of various hardware elements and verification that the stability of reference oscillators would suit the needs of TART.

An approximation of TART error statistics for received signals corrupted by noise was derived via a perturbation analysis and verified with simulated results. This gave insight into the behavior of the TART algorithm and how it was affected by noise for different system geometries. These results were compared to simulated results for σART which showed that the error variance for TART was significantly smaller than σART, the equivalent of that obtained by an approximately 8 dB SNR improvement.

The TART approach was verified using a series of experiments in which the position of a mobile antenna was located in various indoor environments. TART performed as predicted showing that the various synchronization and calibration procedures had been implemented correctly. We observed that TART exhibited the analytically predicted advantages over the current σART approach repeatedly throughout these tests.

There are disadvantages to using TART compared to the current σART approach. TART requires additional hardware complexity; transceivers required on both mobile and reference units instead of dedicated transmitters and receivers. Also our treatment of TART requires twice the number of carriers to acheive a particular range of signal aliasing. While doubling of carriers approach is a valid and straightforward way to solve the time-offset ambiguity problem described in Section 3.3.2, it may not be the most efficient solution. Essentially the additional carriers only provide one bit of

additional information; it may be possible to relax this requirement to use fewer additional carriers while still resolving the time-offset ambiguity.

The experiments conducted used the existing PPL transceiver hardware which was not originally intended for TART, and was not suitable to perform "streaming" data captures, meaning repeated data captures at a rate suitable to track a moving transmitter. For this reason the results presented were from static captures where the mobile antenna was placed at different locations. Past experience using σART has shown that it is possible to estimate the position of a mobile antenna with increased accuracy when it is moving by applying motion constraints in the estimation process. This is most commonly implemented using the Kalman filter, a recursive tracking filter.[20] An example of this is shown in Figure 7.1, which shows a result from a mobile antenna on a cart being moved about the first floor of the WPI Religious Center. We can see that the raw σART position estimates are filtered to produce a result that is more than twice as accurate overall. More information on this topic can be found in reference [4].

Once hardware is in place to perform streaming TART captures it would be desirable to apply Kalman filter techniques to the raw TART position estimates to further improve accuracy. The Kalman filter uses an estimate of measurement variances in order to optimize its state estimates. Providing knowledge of the covariance of the position errors in the x, y and z directions would provide additional information to the Kalman filter that has not been used previously; our TART perturbation error expression could provide an approximation of this for a particular system geometry. The Kalman filter assumes normally distributed error variances. TART errors may not fit this distribution, as there are occasionally large errors due to bad multipath conditions. Occasional large errors, or "outliers," can often be rejected with simple additional logic, as long as most of the errors are small and approximately normally distributed the Kalman filter with outlier rejection logic can perform well. This technique was used on the filtered σART data in Figure 7.1.

The PPL team is currently developing a small mobile transceiver unit to support a full real time TART prototype system. This unit is to have a single transmitter and receiver circuit and connect to a single ranging antenna. One design challenge is choosing a high speed data radio module in order to send received signals to the base station to be processed. Additionally these mobile transceivers need to be "coarsely" synchronized with the reference transceiver units. This coarse synchronization must be accurate on the order of microseconds, and is required in order to coordinate the timing of

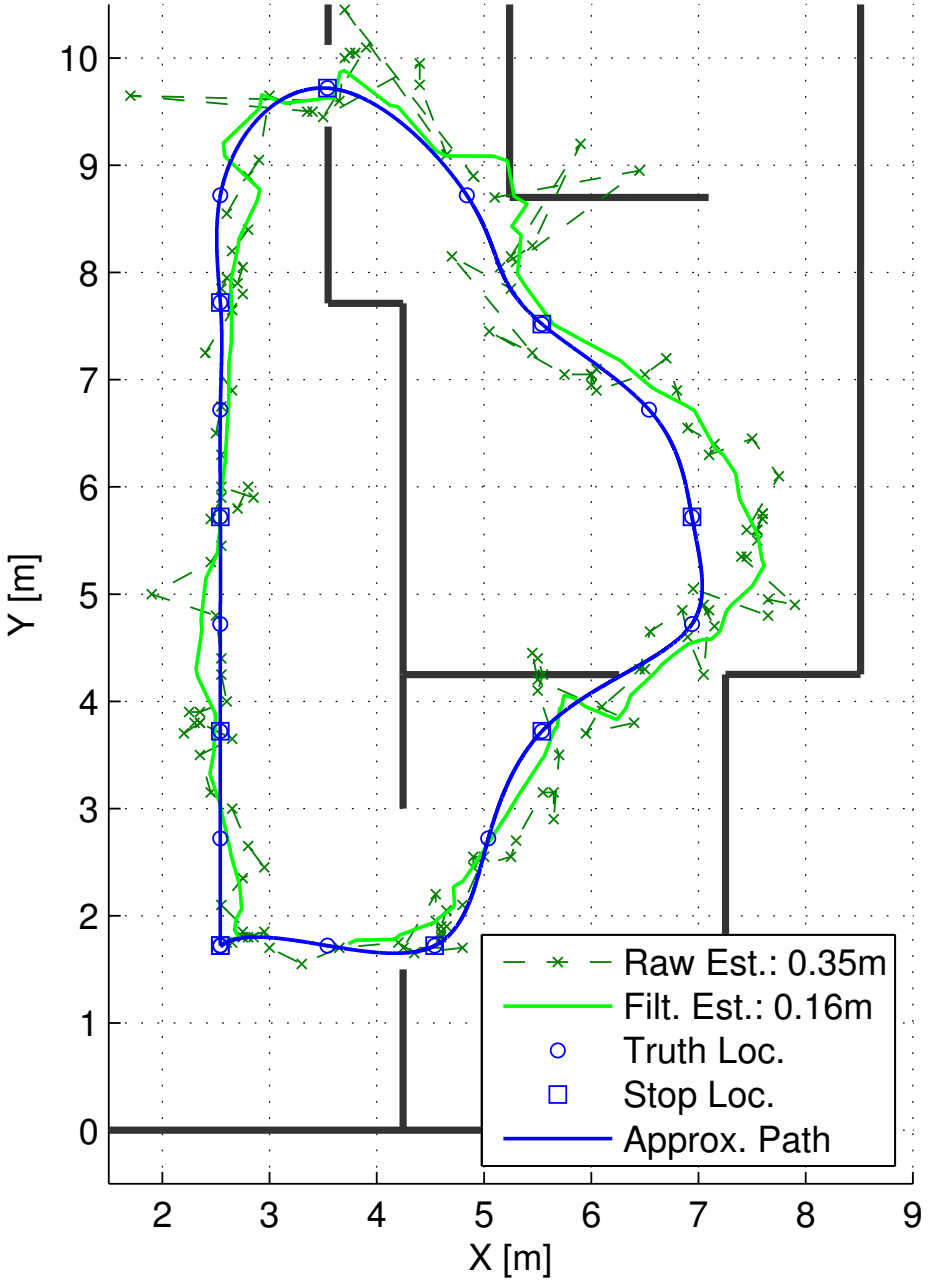

Figure 7.1: Tracking with Kalman Filter

the transactions; as the units take turns transmitting and receiving. The coarse synchronization is to be achieved by the detection of a pulsed signal, as described in [3]. This procedure must be repeated periodically to maintain coarse synchronization. This new mobile unit is being designed to be driven by an inexpensive crystal oscillator, requiring the use of the clock prediction scheme described in Section 4.4. The design of this mobile transmitter is to be documented in an upcoming thesis by another member of the PPL team.[10]

Although we have been allocated 150 MHZ of bandwidth by the FCC, the existing PPL transceiver unit has a design flaw which causes us to restrict our bandwidth to 100 MHz to keep out of band emissions to an acceptable level. This problem has been rectified in the new mobile transceiver unit design, so that the full 150 MHZ can be used. This is expected to increase position accuracy significantly, as discussed in Section 3.2.2.

TART is dependent on preexisting knowledge of the locations of the reference antennas. Automatically determining these locations, which is a very challenging problem in itself, is known as Geometric Autoconfiguration (GAC), and is topic of another dissertation developed by a member of the PPL team.[33] This work uses a rephasing algorithm similar to TART to solve for the reference antenna locations. Not surprisingly, this problem is substantially aided by using synchronized TOA-like signal data. The transactional synchronization techniques developed in this dissertation are directly applicable make a significant contribution to this problem as well.

An additional challenge to using TART to track emergency responders is the use of antennas mounted on personnel. These antennas must be designed to have a small form factor and be close to the human body, which can have an significant effect on the frequency response of the antenna as a function of angle. This could result in weak received signals due to amplitude nulls in the antenna pattern, or even unexpected signal delays due to the phase response of the antenna. This is a challenge that needs to be addressed in the future for TART to be viable. A suggested approach would be to simulate the antenna responses as a function of angle with antenna modeling software and attempt to remove the effects with calibration. The positions and orientations of all of the antennas would need to be known so that the relative angles could be determined. The position and orientation of the reference antennas would presumably be known from the GAC process. The orientation of the mobile antennas could be obtained by an inertial navigation supplementation.[4] The position of the mobile unit is tested at each TART scan location; at each location the corresponding

hypothetical antenna response could be used to calibrate the signal data. At the correct location the correct antenna response would allow the metric to be maximized.

TART is a proposed extension to the PPL system that has great promise to improve position estimate accuracy, particularly in situations with limited reference antenna geometry that is expected to occur in practice. But is it good enough? Can it provide the performance required by emergency responders to be accurate and trustworthy enough in emergency situations and be a source of information upon which life and death decisions could be made? In certain environments, such as wooden residential structures like the WPI Religious center, this could very well be the case. In more challenging settings, such as larger metal and concrete structures, TART may fail to provide the necessary level of accuracy. TART is designed upon the assumption that at least some of the reference antennas receive a direct path signal in order for them to produce a maximum at the correct location. The deeper the mobile transmitter is located in a large building the less likely it is that there will be a direct path signal to any of the reference antennas. It is possible that all of the channel responses measured will contain only reflected signals.

It is possible that TART could be extended to make use of channel response measurements between mobile transceivers, in addition to the channel responses between mobile transceivers and reference transceivers. These indoor-to-indoor channel response measurements may be of higher quality than indoor-to-outdoor measurements if the mobile units are near one another with less intervening material. Such an approach could potentially obtain higher position estimate accuracy by simultaneously estimating the positions of multiple locators with this additional information. This approach would be challenged by the fact that a joint estimation of the location of multiple locators has a much higher dimensional solution space, and also the fact that additional received signal data would need to be sent to the base station.

The TART algorithm is designed to ignore reflected signals and use direct path signals to produce position estimates. Reflected signals do convey information about the location of the mobile unit, albeit much less directly than direct path signals. A direct path signal with a delay t_0 seconds implies that the mobile unit is ct_0 meters away from the reference antenna. A reflected signal with a delay t_0 seconds implies that the mobile unit must be less than ct_0 meters away from the reference antenna, since reflected signals must travel a longer distance than direct path signals. Thus reflected signals can bound the region in which the mobile unit may be located. In more challenging radio

environments, TART may need to be adapted to use such an approach. This will not however provide as accurate a position estimate as is produced with direct path signals. In such situations it is unlikely that TART will be accurate enough to stand alone to produce accurate position estimates. TART would need to be supplemented with information from additional sources such as inertial and barometric pressure sensors, as is commonly used in other navigation applications.

In conclusion, the future of TART, and more largely the Precision Personnel Location system, appears to have both promise and challenge. The new TART approach may not be the final stride in the development of a precision indoor location system for emergency responders, but it is certainly a large step toward that end.

Bibliography

[1] Allan, D. W., Ashby, N., and Hodge, C. C. The Science of Timekeeping: Application note 1289. Tech. rep., Hewlett Packard, 1997.

[2] Amendolare, V. Synchronization in an Indoor Precision Location System. Master's thesis, Worcester Polytechnic Institute, 2007.

[3] Amendolare, V., Cyganski, D., and Duckworth, R. J. WPI Precision Personnel Location System: Synchronization of Wireless Transceiver Units. In *JSDE/ION Joint Navigation Conference* (2009).

[4] Amendolare, V., Cyganski, D., Duckworth, R. J., Makarov, S., Coyne, J., Daempfling, H., and Woodacre, B. WPI Precision Personnel Locator System: Inertial Navigation Supplementation. In *IEEE/ION Position Location and Navigation Symposium (PLANS) Conference* (May 2008).

[5] Athanasios Papoulis, S. U. P. *Probability, Random Variables, and Stochastic Processes*. McGraw Hill, 2002.

[6] Balanis, C. A. *Antenna Theory: Analysis and Design*. John Wiley and Sons, 2005.

[7] Bard, J., Ham, F., and Jones, W. An Algebraic Solution to the Time Difference Of Arrival Equations. *IEEE Transactions on Signal Processing 47*, 2 (Feb. 1999), 1018–1022.

[8] Boyd, S. Multitone Signals with Low Crest Factor. *IEEE Transactions on Circuits and Systems CAS-33*, 10 (Oct. 1986), 313–319.

[9] Breen, D. E. Characterization of Multi-carrier Locator Performance. Master's thesis, Worcester Polytechnic Institute, 2004.

[10] Campbell, M. C. Design of a Mobile Transceiver for Precision Indoor Location. Master's thesis, Worcester Polytechnic Institute, 2010.

[11] Canty, E. J. Six firefighters missing in blaze at vacant building. *Worcester Telegram and Gazette* (Dec. 1999).

[12] Coyne, J., Cyganski, D., and Duckworth, J. FPGA-Based Co-processor for Singular Value Array Reconciliation Tomography. In *16th Annual IEEE Symposium on Field-Programmable Custom Computing Machines* (2008).

[13] Dardari, D., Conti, A., Ferner, U., Giorgetti, A., and Win, M. Z. Ranging With Ultrawide Bandwidth Signals in Multipath Environments. In *Proceedings of the IEEE* (February 2009), vol. 97, pp. 404–426.

[14] David Cyganski, John Orr, W. R. M. A multi-carrier technique for precision geolocation for indoor/multipath environments. Tech. rep., Worcester Polytechnic Institute, Sept. 2003.

[15] Dharmawansa, K., Rajatheva, R., and Ahmed, K. On the Bivariate and Trivariate Rician Distributions. In *Vehicular Technology Conference* (2006).

[16] FOX Electronics. Oscillator part numbering system, 2003.

[17] Golub, G. H., and Van Loan, C. F. *Matrix Computations*. The Johns Hopkins University Press, 1996.

[18] Goodman, N. Statistical analysis based on a certain multivariate complex Gaussian distribution (an introduction). *The Annals of Mathematical Statistics 34*, 1 (1963), 152177.

[19] Hedley, M. System and Algorithms for Accurate Indoor Tracking using Low-Cost Hardware. In *IEEE/ION Position Location and Navigation System Conference* (May 2008).

[20] Kalman, R. E. A new approach to linear filtering and prediction problems. *Transaction of the ASME-Journal of Basic Engineering 82(Series D)* (1960).

[21] Kennedy, T. J. Workshop on precision personnel location and tracking August 7-8, 2006. Tech. rep., Worcester Polytechnic Institute, Aug. 2006.

[22] Lachapelle, G., Kuusniemi, H., Dao, D. T. H., MacGougan, G., and Cannon, M. E. HSGPS signal analysis and performance under various indoor conditions. Tech. rep., University of Calgary, Sept. 2003.

[23] Lathi, B. P. *Signal Processing and Linear Systems*. Berkeley-Cambridge Press, 1998.

[24] Lax, P. D. *Linear Algebra*. John Wiley and Sons Inc., 1997.

[25] Marple, S. L. *Digital Spectral Analysis*. Prentice-Hall, 1987.

[26] McCullough, J. R., Irwin, B. J., and Bowles, R. M. LORAN-C Latitude-Longitude Conversion at Sea: Programming Considerations. In *The Wild Goose Association: Proceedings of the Eleventh Annual Technical Symposium* (Oct. 1982).

[27] Nangle, R. Worst building fire disaster in 21 years. *Worcester Telegram and Gazette* (Dec. 1999).

[28] Opshaug, G. R., and Enge, P. GPS and UWB for indoor navigation. Tech. rep., Stanford University, Sept. 2001.

[29] Orr, J., and Cyganski, D. Firefighter and other emergency personnel tracking and location technology for incident response. Tech. rep., Worcester Polytechnic Institute, July 2001.

[30] Ravindran, S. Fire Escape. *Popular Science* (Mar. 2010).

[31] Trefethen, L. N., and III, D. B. *Numerical Linear Algebra*. Society for Industrial and Applied Mathematics, 1997.

[32] Woodacre, B., Cyganski, D., Duckworth, J., Makarov, S., Michalson, W., Orr, J., Amendolare, V., Coyne, J., and Daempfling, H. WPI precision personnel locator system: Automatic antenna geometry estimation. In *Proceedings of the Institute of Navigation National Technical Meeting* (San Diego, California, January 2008).

[33] Woodacre, B. W. *Geometric Autoconfiguration for Precision Personnel Location*. PhD thesis, Worcester Polytechnic Institute, 2010.

[34] WRIGHT, C. R. *Multidimensional Direction of Arrival Performance Bounds and Optimization for Non-Stationary Noise*. PhD thesis, Worcester Polytechnic Institute, 1994.